
Investigating Gamma-Ray Burst Progenitors & Central Engines

Nicola Lyons

Supervisors:

Paul O'Brien

Nial Tanvir

Thesis to be submitted for the degree of

Doctor of Philosophy

at the University of Leicester.

X-Ray & Observational Astronomy Group

Department of Physics and Astronomy

University of Leicester

May 7, 2013

Publication List

Lyons N. *et al.* 2010, MNRAS, 402, 705

Rowlinson A. *et al.* 2010, MNRAS, 409, 531

Troja E. *et al.* 2008, MNRAS, 385, 10

Thesis Abstract

The aim of this thesis is to study Gamma-Ray Burst (GRB) progenitors and central engines, I begin by examining unexpected plateaus in GRB light curves and place constraints on the central engine, that are consistent with a proto-magnetar. Next I compare these to the normal plateaus seen in the light curve and expand my investigation to include flares. Finally I investigate whether some giant flares could actually be a GRB if the GRB in those light curves could be a progenitor.

Acknowledgements

I would like to thank everyone who helped me get this far, especially my family and friends, without your support and encouragement this thesis would not have become a reality. Thank you to my supervisor Professor Paul O'Brien and everyone I worked with in the *Swift* team.

Contents

1	Introduction	22
1.1	Introduction	22
1.1.1	Vela Satellites	22
1.1.2	Compton Gamma-Ray Observatory	25
1.1.3	The BeppoSax Satellite	29
1.1.4	<i>Swift</i>	31
1.2	The Prompt Phase	37
1.2.1	Energetics	37
1.2.2	Beaming	38
1.2.3	Spectrum	39
1.2.4	Temporal Properties	40
1.3	The Afterglow	43
1.3.1	The Canonical light curve	43
1.4	The Fireball Model	46
1.5	Fireball Model Additions	49
1.5.1	Jets	49
1.5.2	A non-uniform external medium	50

1.5.3	Microphysics	50
1.5.4	Pair formation, neutrons and other effects	51
1.6	The collapsar model	51
1.7	The binary merger model	52
1.8	Long or Short GRBs	53
2	Magnetars & GRBs	56
2.1	Abstract	56
2.2	Introduction	57
2.3	Swift light curves	61
2.4	Internal Plateau Sample	63
2.5	The magnetar model	74
2.6	Discussion	83
3	GRBs at known distances	86
3.1	Introduction	86
3.1.1	Light Curve Shape	91
3.1.2	Prompt Pulses	95
3.2	Method	97
3.2.1	K-corrections	97
3.2.2	Interpolating the data	101
3.2.3	Pulse fitting flares	104
3.2.4	Analysis	106
3.2.5	GRBs with plateaus	125
3.2.6	Light curves of GRBs with flares	129
3.2.7	Flares	133

3.3	Conclusions	141
4	Giant flares	143
4.1	Introduction	143
4.1.1	Models for large flares	144
4.1.2	Precursors	148
4.2	Method	156
4.2.1	Spectral Energy Distributions	156
4.2.2	Obtaining Lorentz factors	157
4.3	Data Analysis	158
4.4	Conclusions	175
5	Conclusions	178
5.1	Thesis Overview	178
5.2	Thesis Summary	180
5.3	What is the central engine?	180
5.4	Central Engine Activity	183
5.5	Probing high redshifts	185
5.6	Conclusions	186
6	References	187

List of Tables

2.1	The observed properties for each of the internal plateaus of GRBs in my sample and also the Steep Decay once the plateau has ended.	71
2.2	The different beamed energies found for the plateau for different opening angles compared to the energy of the actual GRB and the energy available in the rotational energy reservoir. All energies in Table 2 are in ergs, the opening angles used to find the beamed energy respectively are 4 and 18 degrees. The GRB E_{iso} values were taken from <i>Swift</i> GCN Notices referenced above and in Chapter 6.	82
4.1	The observed and rest frame properties of the GRBs and giant flares in my sample. Where E_{iso} is the isotropic energy released in either the GRB or the flare, denoted by the subscript	161
4.2	The time cuts used for the model fitting of each giant flare and the results for the best fitting models to the giant flare spectra.	163
4.3	The parameters found for each giant flare using Formula 4.1, the results for the giant flare for GRB 050502B is found in Jin, Fan & Wei (2010), the centre time of each flare is also included for comparison with results found in Jin, Fan & Wei (2010).	173

List of Figures

- 1.1 The gamma-ray burst on 2nd August 1970 recorded by three of the Vela satellites. The arrows show peaks observed by each of the satellites establishing that they are a genuine phenomenon and not a source of noise aboard one of the satellites (Klebesadel, Strong & Olson 1973) 24
- 1.2 The sky distribution of 2,704 GRBs observed by BATSE colour coded by fluence, statistical tests confirm the GRBs are isotropically distributioned on the sky; no significant quadrapole or dipole moment is found (<http://www.nasaimages.org/luna/servlet/view/all>). 27

- 1.3 The durations of the GRBs recorded with BATSE (Kouveliotou *et al.* 1993). The duration parameter used is T_{90} , which is the time over which a burst emits from 5% to 95% of its total measured counts. The solid line shows the distribution of the uncorrected values for T_{90} . To correct for the time errors δT_{90} in each time bin, Kouveliotou *et al.* (1993) assumes that each T_{90} is represented by a Gaussian distribution. Next each error convolved bin is found by adding all the overlapping Gaussians. The convolved distributions are shown by the dotted line. 28
- 1.4 An image of the afterglow of GRB 970228 in the 2-10 keV range. The left panel shows a previously unknown X-ray source visible 8 hours after the GRB. The right panel shows the X-ray source three days later when it had faded by a factor ~ 20 29
- 1.5 A picture of the *Swift* satellite labelled with the BAT, XRT and UVOT. <http://www.swift.psu.edu> 35
- 1.6 A schematic view of the early GRB light curve. After the prompt emission the decay tends to follow one of two paths: A steep decay during which the flux can fall by 3 or more orders of magnitude, followed by a plateau starting between $10^3 - 10^4$ seconds, is known as the canonical GRB light curve. Alternatively it can follow a gradual decay. Either decay path may have flares occurring or can end with a break $> 10^4$ seconds to a steeper decay (O'Brien *et al.* 2006). 36

- 1.7 The evolution of the X-ray spectral index β_{XRT} with time since the BAT trigger for GRB 070616. GRB070616 had unusually prolonged prompt emission with a T_{90} (15 - 350 keV) = 402 ± 10 seconds. The spectral evolution from the prompt to the afterglow emission is modelled with the curvature model plus an underlying afterglow component (Starling *et al.* 2007). 41
- 1.8 The *Swift* distribution of GRB durations, the top panel shows the GRB T_{90} duration; the lack of short GRBs detected is clearly visible compared to Figure 1.3 (Sakamoto *et al.* 2008). The lower panel shows the distribution of the T_{50} duration i.e. the time over which a burst emits from 25% to 75% of its total measured counts. 42
- 1.9 The BAT light curve and hardness ratio of GRB 060614. The BAT light curve (15 - 150 keV) at 1 second time resolution is shown in the upper panel, where the solid-dotted line marks the T_{100} interval and dotted vertical lines mark the beginning and end of the satellite slew time. The lower panel shows the hardness ratio of the count rate in the 25 - 150 keV and in the 15 - 25 keV band (Manganol *et al.* 2007). 54

2.1 The top panel shows the light curve in the BAT and XRT for GRB 060510B and the bottom panel displays a more typical burst; GRB 060427. The green line represents emission from the burst (prompt) and the blue line emission from the afterglow, as given by the Willingale et al. (2007) model. The portions in red in the left panel are the data (flares and internal plateaus) which the model does not fit. 59

2.2 The GRB light curves displaying internal plateau behaviour. The green line represents emission from the burst (prompt) and the blue line emission from the afterglow, as given by the Willingale et al. (2007) model. The portions in red are the data (flares and internal plateaus) which the model does not fit. 66

2.3 The GRB light curves displaying internal plateau behaviour. The green line represents emission from the burst (prompt) and the blue line emission from the afterglow, as given by the Willingale et al. (2007) model. The portions in red are the data (flares and internal plateaus) which the model does not fit. 67

2.4 The GRB light curves displaying internal plateau behaviour. The green line represents emission from the burst (prompt) and the blue line emission from the afterglow, as given by the Willingale et al. (2007) model. The portions in red are the data (flares and internal plateaus) which the model does not fit. 68

2.5 The GRB light curves displaying internal plateau behaviour. The green line represents emission from the burst (prompt) and the blue line emission from the afterglow, as given by the Willingale et al. (2007) model. The portions in red are the data (flares and internal plateaus) which the model does not fit. 69

2.6 The GRB light curves displaying internal plateau behaviour. The green line represents emission from the burst (prompt) and the blue line emission from the afterglow, as given by the Willingale et al. (2007) model. The portions in red are the data (flares and internal plateaus) which the model does not fit. 70

2.7 Combined BAT, XRT, and UVOT light curves for the 4 GRBs with multi-wavelength data during the internal plateau. The vertical dashed lines indicate the time interval over which the internal plateau dominates the emission. The optical data have been scaled down by a factor of ten in panels a and c. 72

- 2.8 The initial period and magnetic field for each of the GRBs examined. In the left-hand panel it was assumed that energy was released isotropically, whereas in the middle and right-hand panels it is beamed with an opening angle of 4 and 18 degrees respectively. GRBs with red filled circles have known redshifts and their internal plateaus occur during the prompt emission; GRBs shown by blue filled squares have known redshifts and their internal plateaus occur after the prompt emission; GRBs shown by green filled triangles have internal plateaus that occur during the prompt emission at unknown redshifts, and for which the redshift has been assumed to be equal to the median redshift of the *Swift* sample, meaning their parameters are more uncertain. The light grey shaded regions show limits based on the magnetic field and period limits discussed in the literature. See text for details. The darker grey shaded region shows where a progenitor would be violating the breakup spin-period of a neutron star. 78

2.9	The relationship between the length of the internal plateau emission and its luminosity in the observers frame, where it was assumed that energy was released isotropically in the left panel and beamed with an opening angle of 4 degrees in the right panel. GRBs with red filled circles have known redshifts and their internal plateaus occur during the prompt emission, GRBs shown by blue filled squares have known redshifts and their internal plateaus occur after the prompt emission. The GRBs shown by green filled triangles have internal plateaus that occur during the prompt emission at unknown redshifts.	79
3.1	The cumulative distributions of the maximum redshifts at which 15 GRBs redshifts and published peak photon number fluxes would be detectable by BATSE, HETE-II and <i>Swift</i> (Lamb 2007).	88
3.2	A diagram to place the maximum expected redshift of GRBs and Quasars in a cosmological context. The epochs of first light and re-ionization are shown on a scale of redshift and the age of the Universe (Lamb 2007).	89
3.3	A schematic diagram of the different GRB morphologies (Evans <i>et al.</i> 2009). Panel a shows canonical light curves (also shown in Chapter 1 Section 1.1.4 Figure 1.6 Steep decay path), panels b and c show light curves with one break either flattening b or steepening c, panel d shows light curves with no breaks. Evans <i>et al.</i> (2009) also defines any light curves that do not fall into one of these morphologies as oddball light curves.	93

- 3.4 The energy release over 20-20,000 keV of 17 cosmological GRBs. The k-corrected energies and their estimated errors are indicated by dark squares and the uncorrected energy by a cross (Bloom *et al.* 2001) 98
- 3.5 A schematic diagram of a GRB's flux and energy, which has been annotated with some of the parameters used to find each k-correction. Figure 3.5 also shows the measured energy range detected using *Swift* compared to the k-corrected energy range. 100
- 3.6 The light curve of GRB 060218 and the linear interpolation between each datapoint. The original data points in red and in green the linear interpolation and the error on each interpolated point. . . 103
- 3.7 A schematic diagram showing important parameters for the pulse fitting model, where the pulse rises over time T_{rise} until it reaches a peak T_{pk} . The characteristic times of the pulse T_f and $T_0 = T_f - T_{rise}$ are the arrival times of the last photon and the first photon emitted from the shell, along the line of sight measured with respect to the ejection time T_{ej} 105
- 3.8 A simplified diagram of how the program uses a series of trapeziums to estimate the area under the light curve of each GRB. Since the step size of the interpolation program is very small this was taken to be the width of the trapezium. 107
- 3.9 The relationship between the luminosity of a GRB (ergs s^{-1}) and its isotropic energy (ergs) in the rest frame 10 seconds after the initial burst, for which the scatter in luminosity is 0.12 dex. . . . 109

-
- 3.10 The relationship between the luminosity of a GRB (ergs s^{-1}) and its isotropic energy (ergs) in the rest frame 100 seconds after the initial burst, for which the scatter in luminosity is 1.94 dex. 110
- 3.11 The relationship between the luminosity of a GRB (ergs s^{-1}) and its isotropic energy (ergs) in the rest frame 10^3 seconds after the initial burst, for which the scatter in luminosity is 5.06 dex. 111
- 3.12 The relationship between the luminosity of a GRB (ergs s^{-1}) and its isotropic energy (ergs) in the rest frame 10^4 seconds after the initial burst, for which the scatter in luminosity is 5.16 dex. 112
- 3.13 The relationship between the luminosity of a GRB (ergs s^{-1}) and its isotropic energy (ergs) in the rest frame 10^5 seconds after the initial burst, for which the scatter in luminosity is 2.54 dex. 113
- 3.14 The relationship between the luminosity of a GRB (ergs s^{-1}) and its isotropic energy (ergs) in the rest frame 10^6 seconds after the initial burst, for which the scatter in luminosity is 0.32 dex. 114
- 3.15 The luminosity of each GRB at 100 and 1,000 seconds, when there should be a larger separation in luminosity due to spectral shape O'Brien *et al.* (2006). The GRBs are displayed colour-coded by their light curve shape. 116
- 3.16 The complete lightcurve of a GRB chosen from each light curve morphology with redshift closest to $z = 1$. Each GRB light curve is then colour-coded by shape 119
- 3.17 The complete lightcurve of a GRB chosen from each light curve morphology with redshift closest to $z = 2$. Each GRB light curve is then colour-coded by shape 120

-
- 3.18 The complete lightcurve of a GRB chosen from each light curve morphology with redshift closest to $z = 3$. Each GRB light curve is then colour-coded by shape 121
- 3.19 The complete lightcurve of a GRB chosen from each light curve morphology with redshift closest to $z = 4$. Each GRB light curve is then colour-coded by shape 122
- 3.20 The light curves of two GRBs plotted in the rest frame at each redshift step. 124
- 3.21 The variation in luminosity and end time of the plateau for GRBs with traditional plateaus and GRBs with internal plateaus. Early internal plateaus are shown in red, blue shows late internal plateaus and traditional plateaus are green. 126
- 3.22 The relationship between period and magnetic field found for GRBs with an internal plateau compared to those with a traditional plateau. Early internal plateaus are shown in blue, orange shows late internal plateaus, traditional plateaus are green and red shows traditional plateaus which also have an internal plateau in their light curve 128
- 3.23 The population of each light curve shape for all GRBs with redshift and no flares (blue), for all GRBs with redshift and normal flares (red) and GRBs with giant flares (beige) and measured redshift. 130

3.24	The luminosity of afterglows with flares (red), giant flares (green) or without flares (blue). The letters represent different light curve morphologies where A, B, C, and E are canonical, one break flattening, one break steepening and oddball light curves respectively	132
3.25	The correlation between the flare peak luminosity and T_f found in Willingale <i>et al.</i> (2010), plotted with GRBs from this chapter.	135
3.26	The relation between the time the pulse peaks and the time between pulse ejection and the time the flare peaks; the equivalent width of flares.	137
3.27	The relation between flare energy and the magnetic field strength of the central object. The magnetic field strength was found using the end time of traditional and internal plateaus which are indicated separately.	139
3.28	Flare energy plotted against the initial rotation of the central object. The central object's initial rotation was found using the end time of traditional and internal plateaus which are indicated separately.	140
4.1	A schematic diagram of the luminosity of a GRB and giant flare as time passes. Panel a shows the usual definition of GRB and flare, for this chapter I investigate the scenario in panel a compared to precursors and the giant flares to examine if the scenario in panel b could be correct for some GRBs	144

- 4.2 The propagation of the jet through the stellar mantle, initially the jet is unable to move the envelope material to a speed comparable to its own and is thus abruptly decelerated. As the jet propagates a bow shock propagates ahead (a), a strong thermal precursor is produced as the shock breaks the stellar surface and exposes the hot shocked material (b). The fireball escapes the stellar envelope and interacts with very dense photon emission (c) (Ramirez-Ruiz, MacFadyen & Lazzati 2002). 151
- 4.3 A schematic diagram of the curvature emission component that is used for the method used to find giant flare Lorentz factors. Where R is the ratio between the peak flux of the X-ray flare $F_{x,p}$ and the flux when a cutoff emerges $F_{x,c}$. T_{tail} is the time the curvature emission component ends (Jin, Fan & Wei 2010). 159
- 4.4 The lightcurves,hardness ratios and photon indices of GRB 050502B and GRB 060124. The photon indices were supplied by the UK Swift Science Data Centre at the University of Leicester (Evans *et al.* 2007) 165
- 4.5 The lightcurves,hardness ratios and photon indices of GRB 060526 and GRB 061121. The photon indices were supplied by the UK Swift Science Data Centre at the University of Leicester (Evans *et al.* 2007) 166
- 4.6 The lightcurves,hardness ratios and photon indices of GRB 070704 and GRB 100619A. The photon indices (and hardness ratio for GRB 100619A) were supplied by the UK Swift Science Data Centre at the University of Leicester (Evans *et al.* 2007) 167

- 4.7 The isotropic energy of the giant flare/precursor plotted against the isotropic energy of the GRB. GRBs with giant flares (red spots) are then compared to GRBs with precursors from B08; where blue stars denote GRBs that are also in my giant flare sample and green crosses all other GRB in B08 170
- 4.8 The relationship between the burst T_{90} and the quiescent period between GRB and flare or precursor. The GRBs with giant flares are shown by red spots, whereas the blue stars are GRB with precursors that are in B08 and also in my giant flares sample, all other GRBs with precursors in B08 are represented by green crosses. . . 172
- 4.9 The upper limits of the bulk Lorentz factor of the outflow powering GRB flares and the centre time of the flares. The hollowed and filled triangles are where the spectrum is assumed to be modelled by a single power law and the band function respectively. In black are normal flares and the red stars are two giant flares (Jin, Fan & Wei 2010). 174
- 5.1 The curved red line indicates the new forbidden zone (also shaded in dark grey), the black lines show theoretical limits in Lyons *et al.* 2010. The dotted lines indicate the merger model for short GRB 090515 and the solid blue line the collapsar model for GRB 090515. Green data points represent the long GRB sample with internal plateaus. 182

Chapter 1

Introduction

1.1 Introduction

1.1.1 Vela Satellites

In this chapter I summarise the discovery and observation of Gamma-Ray Bursts (GRBs), the most powerful objects in the Universe. The US ‘Vela’ satellites were sent into space to monitor the Nuclear Test Ban Treaty signed in 1963, which forbade nuclear explosions in the atmosphere, underwater or in space. However their lasting legacy was the discovery of bright gamma-ray flashes, now known as Gamma-Ray Bursts.

To detect a nuclear explosion in space the Vela satellites were going to monitor X-rays and gamma-rays. On the 2nd July 1967 the Vela satellites detected an unexpected burst of gamma-rays shown in Figure 1.1. This was not confused with gamma-rays produced by a nuclear explosion because instead of having a sharp peak followed by a slow levelling and finally a slow fading due to the decay

of unstable elements. The observed signal had two distinct peaks rather than a gradual fading and it also lacked the intense flash.

The Vela satellites could accurately locate nuclear explosions out to several times the distance of the Moon, further out it was only possible to set a lower bound on distance. Using the Vela satellites' data for the distance and direction it was possible to rule out GRBs as events within the Solar System.

Originally it was thought that GRBs were events in our galaxy because of the huge amounts of energy involved. For example if GRB 080319B, which had isotropic energy of $E_{\text{iso}} \approx 7 \times 10^{52}$ ergs and a distance of 6116.9 Mpc (Racusin *et al.* 2008); occurred within the Milky Way its isotropic energy (found assuming a distance of 25,000 parsecs) would be $\approx 6 \times 10^{45}$ ergs. With these lower energies the leading model was that GRBs could be caused by violent disturbances in the magnetospheres of neutron stars within our galaxy (Rees, Mészáros & Begelman 1994). If GRBs were of galactic origin then the distribution of GRB positions would have a concentration near the galactic centre, also other galaxies would show up as hot spots.

For long GRBs, the isotropic energy is found to be from 10^{51} to 10^{54} erg (for the energy range 1 keV - 10 MeV). Energies around 10^{54} ergs are hard to produce using the favoured model (the Sun's rest mass energy is 1.8×10^{54} ergs). For the efficiency of a GRB to be $\sim 20\%$ (Bloom, Frail & Kulkarni 2003), this would imply a maximum expected energy for a GRB to be roughly an order of magnitude below the higher energies observed for a GRB (few $\times 10^{54}$ erg). This also does not take into account any mass that would be tied up in the compact object remaining after the GRB or in the expected accretion disk.

Supernovae have a typical isotropic energy of 10^{51} ergs (Chevalier 2005).

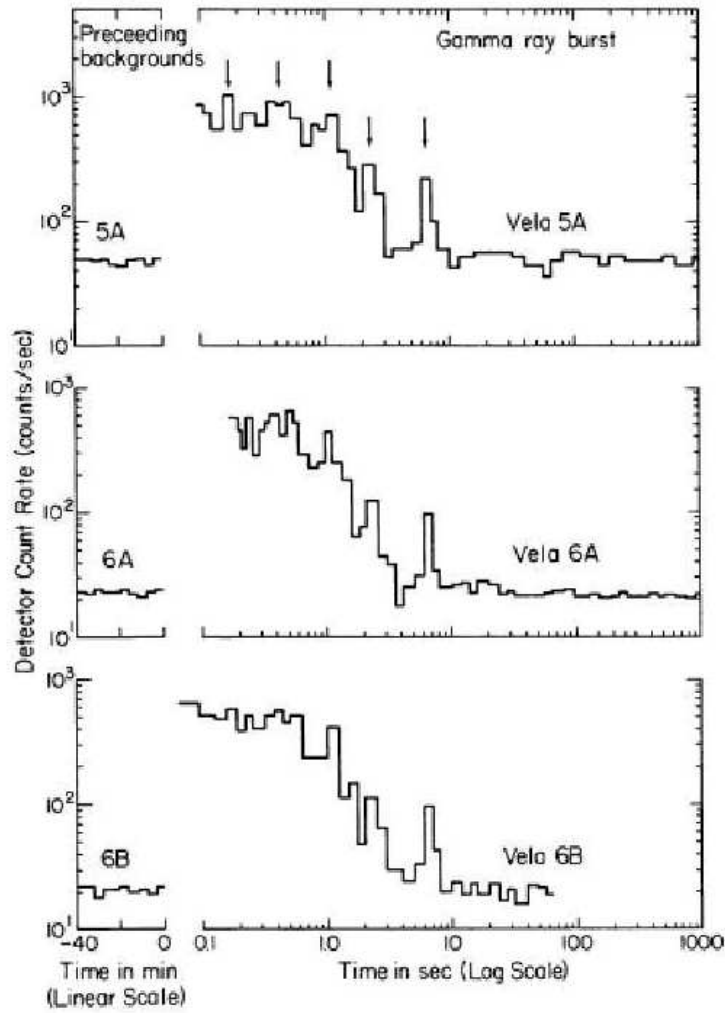


Figure 1.1: The gamma-ray burst on 2nd August 1970 recorded by three of the Vela satellites. The arrows show peaks observed by each of the satellites establishing that they are a genuine phenomenon and not a source of noise aboard one of the satellites (Klebesadel, Strong & Olson 1973)

However the electromagnetic energy output of a GRB during tens of seconds appears to be of the order of a percent or less of the total energy output, but even this photon output (in gamma-rays) is comparable to the total kinetic energy output leading to optical photons by a supernova over weeks (Mészáros 2006).

The main issue with GRBs occurring at cosmological distances are that the observed gamma-ray fluences imply a total energy of the order of a solar rest mass $\sim 2 \times 10^{54}$ ergs (Mészáros 2006), if the radiation is emitted isotropically. Woosely 1993 states that the progenitor star should collapse to a black hole with mass (M) \sim few solar masses (M_{\odot}) with an accretion disk of $0.5 M_{\odot}$ which grows at a few tenths $M_{\odot} \text{ s}^{-1}$, this would require that the disk mass was converted into gamma-rays at $\sim 92.6\%$ efficiency. For long GRBs the efficiency is thought to be 20% (Kobayashi *et al.* 1997, Bloom, Frail & Kulkarni 2003).

1.1.2 Compton Gamma-Ray Observatory

However it was not until 1991 that our understanding of GRBs significantly improved, with the launch of NASA's Compton Gamma-Ray Observatory (CGRO) that included the Burst And Transient Source Experiment (BATSE). BATSE used eight sodium iodide scintillators facing outward from each corner of the satellite, these are sensitive to gamma-ray energies over the band 20-100 keV.

The scintillators produce a flash of visible light when struck by gamma-rays. Flashes were recorded by light sensitive-detectors whose signal output is digitized and analyzed to determine the arrival time and energy of the gamma-ray which caused the flash. The relative gamma-ray fluxes are recorded by different detectors could also provide positions on the sky.

Unfortunately, the BATSE uncertainty of ~ 4 arc minutes (Fishman 1998) meant counterpart features were not discovered in other parts of the electro-magnetic spectrum. In spite of this BATSE detected 2704 bursts over its 9 year lifetime. The analysis of these led to the following major discoveries:

1. The distribution of GRBs on the sky is isotropic as shown in Figure 1.2, this strongly indicating either GRBs occurred in the galactic halo (Podsiadlowski *et al.* 1995) or at extra galactic distances, this result provided evidence of cosmological origin (Briggs *et al.* 1996).
2. The duration of GRBs have a bimodal distribution divided at ~ 2 seconds as shown in Figure 1.3. It was also found that GRBs with durations < 2 seconds release more of their energy in very energetic gamma-rays relative to longer bursts which have soft spectra (Kouveliotou *et al.* 1993).

The distinction between the two main populations was relatively clear; they were classified into two types short and long i.e. those shorter than 2 seconds and those longer than 2 seconds (Kouveliotou *et al.* 1993). This also provided the first evidence for two different progenitors for GRBs, long GRBs were thought to be produced when a rapidly rotating massive star collapsed to form a black hole, whereas for short bursts the merger of two neutron stars or a neutron star and a black hole.

An easy test for if GRBs were from very distant galaxies would be to search for lines in the spectrum which should indicate that GRBs have large redshifts; however no lines were observed in the spectra from any GRB. This was consistent with the theory that the radiation is emitted by synchrotron radiation¹.

¹Synchrotron radiation is where a charged particle moves very close to the speed of light in a

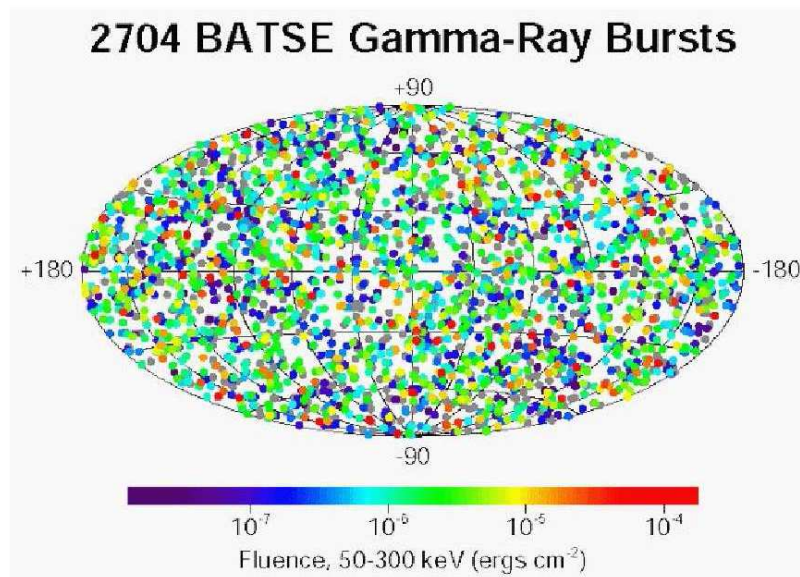


Figure 1.2: The sky distribution of 2,704 GRBs observed by BATSE colour coded by fluence, statistical tests confirm the GRBs are isotropically distributed on the sky; no significant quadrupole or dipole moment is found (<http://www.nasaimages.org/luna/servlet/view/all>).

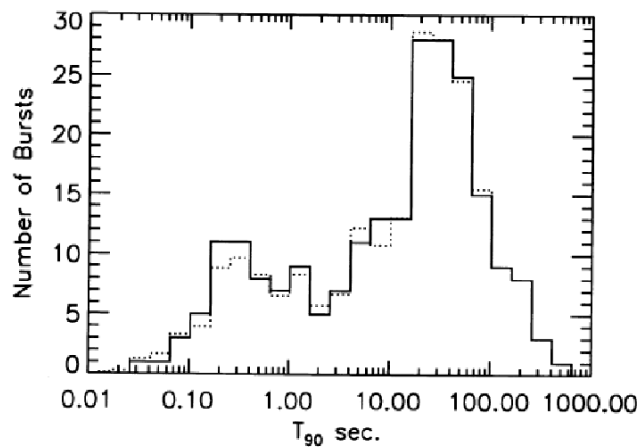


Figure 1.3: The durations of the GRBs recorded with BATSE (Kouveliotou *et al.* 1993). The duration parameter used is T_{90} , which is the time over which a burst emits from 5% to 95% of its total measured counts. The solid line shows the distribution of the uncorrected values for T_{90} . To correct for the time errors δT_{90} in each time bin, Kouveliotou *et al.* (1993) assumes that each T_{90} is represented by a Gaussian distribution. Next each error convolved bin is found by adding all the overlapping Gaussians. The convolved distributions are shown by the dotted line.

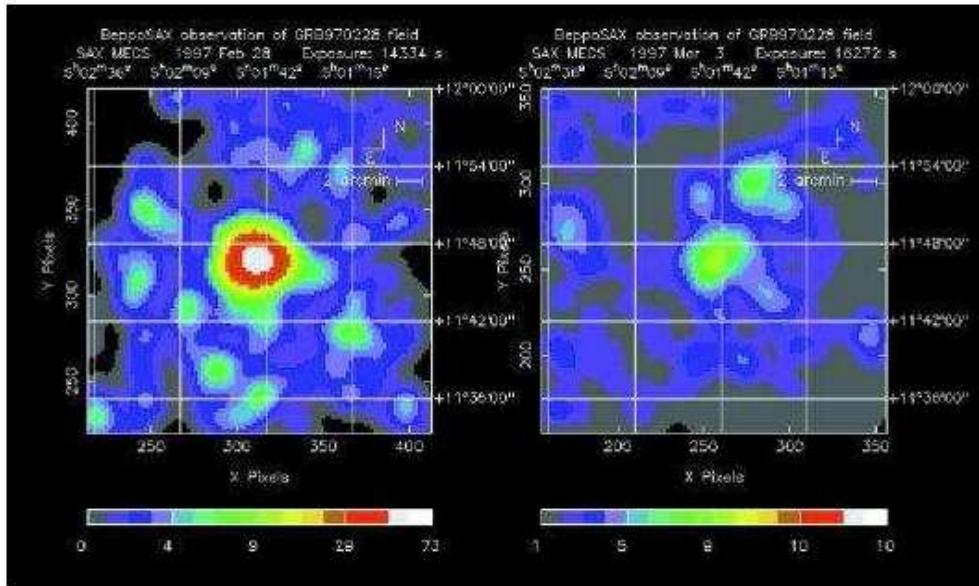


Figure 1.4: An image of the afterglow of GRB 970228 in the 2-10 keV range. The left panel shows a previously unknown X-ray source visible 8 hours after the GRB. The right panel shows the X-ray source three days later when it had faded by a factor ~ 20 .

1.1.3 The BeppoSax Satellite

The BeppoSax satellite discovered the first GRB afterglow on the 28th February 1997, which is shown in Figure 1.4. The key innovation for BeppoSax was a second instrument focused by quickly slewing the satellite to try to rapidly find the X-ray flare from the GRB and to provide a much more accurate location with an uncertainty of a few minutes of an arc (Mangano, Holland & Malesani 2007).

Despite providing the first afterglow localization no redshift measurement could be determined. Thus once the burst had faded and a ‘fuzzy’ nature of the medium around the burst it was impossible to tell if this was a local nebula or a distant host galaxy. The first redshift measurement was given by the Mg_{II} doublet spiral path in a magnetic field and thereby radiates energy in the form of electromagnetic waves.

line ratios ($z \geq 0.835$) and an absence of the Lyman- α absorption features ($2.3 \geq z$) in the spectra of an optical counterpart to GRB 970508 (Metzger *et al.* 1997). Metzger *et al.* (1997) could not rule out the possibility that the optical emission is due to a chance coincidence of a BL Lac Object within the GRB error circle (with a probability $\sim 2 \times 10^{-4}$), however the chance of finding a chance BL Lac Object that also displays the same temporal variability as the GRB is very small. Assuming the minimum distance and cosmology of $H_0 = 70 \text{ km s}^{-1} \text{ Mpc}^{-1}$ and $\Omega_0 = 0.2$, the luminosity distance is at least 48 Gpc.

BeppoSax continued capturing bursts including GRB 980425. Optical observations failed to find an afterglow, but instead observed a supernove Type Ic², the probability of a chance alignment was $< 1 \times 10^{-5}$. However, it was not until GRB 030329, that the relation between GRBs and supernovae was confirmed, agreeing with the favoured progenitor model. Here a supernovae spectrum was superimposed upon the afterglow and the timing of the supernova suggests it exploded within a few days of the burst (Horth *et al.* 2003; Stanek *et al.* 2003).

The X-ray luminosity of GRB 030329 was $\sim 10^{51} \text{ erg s}^{-1}$ (Schmidt 2001) which typical for a cosmological GRB (see Section 1.2.1). However the nearby (40 Mpc) GRB 980425 was ~ 5 orders of magnitude lower (Pian *et al.* 2000), it could be that SNe 1b/c produce 2 classes of GRB or that GRB 980425 is a typical GRB jet viewed off axis (Guetta *et al.* 2004).

If Supernovae 1b/c produce different classes of GRBs, with most long GRBs produced by the scenario discussed in Sections 1.1.2 and 1.6, the origin of the

²Supernovae Type Ic are supernovae containing no hydrogen and no (or very weak) helium lines in their spectra. The progenitors of Types Ic supernovae lose most of their outer hydrogen-rich and helium envelopes due to strong stellar winds or else from interaction with a companion (Pols 1997).

second low-luminosity class is unknown. It could be due to the supernovae shock break out (Colgate 1968, Woosley & Weaver 1986 and Matzner & McKee 1999), the small radius and high density of the progenitor may allow a jet to escape with a mildly relativistic speed, but it may not transfer sufficient energy to account for γ -ray emission (Waxman 2004).

If the GRB jet is viewed from a direction making $\theta_j + \text{few} \times \frac{1}{\Gamma}$ with the jet axis, where Γ is the Lorentz factor, the γ -ray flux may be strongly suppressed (Nakamura 1998, Eichler & Levinson 1999, Woosely *et al.* 1999, Granot *et al.* 2002, Yamazaki *et al.* 2003), radio emission is then expected at ~ 1 year delay (Frail *et al.* 2000 and Livio & Waxman 2000).

1.1.4 *Swift*

On 11th December 2002, a telescope known as RAPTOR responded to a trigger from HETE-II for GRB 021211; it started imaging 64.9 seconds after the GRB was detected. This was one of the fastest response times before *Swift*. If RAPTOR had not started imaging so quickly the afterglow would not have been seen and the GRB would have been classified as a dark gamma-ray burst³. About 50% of the GRBs precisely located by BeppoSax have no optical afterglow, about 60% have no radio detection and about 10% have no X-ray afterglow.

Historically the time delay between the burst and when the small error-box positions are available, and therefore when the follow-up observations can begin are typically in the range of 3-8 hours (Barthelmy *et al.* 2005) and cause difficulty to studying GRB central engines. *Swift* has eliminated such delays by using a sin-

³Dark gamma-ray bursts are GRBs observed without an afterglow, this could be because the afterglow faded too quickly for telescopes to move to the right direction or that some GRBs occur in galaxies that contain a lot of dust blocking the optical light from the afterglow.

gle spacecraft instrument to detect a burst, provide a position within 12 seconds of the initial trigger, within as little as 20-70 seconds (Barthelmy *et al.* 2005). *Swift* incorporates on board autonomy to slew the spacecraft to point the X-ray Telescope and UV-Optical Telescope at the burst position to begin observations without ground-based intervention. This autonomous response allows *Swift* to examine GRBs faster than previous instruments, providing rapid multi-wavelength data of a GRB which is used to study GRBs in this thesis at varying timescales.

The *Swift* satellite hoped to identify the positions of GRBs, so their progenitors can be identified and to study the afterglow i.e. the first 1,000 seconds to provide more detail about the blast wave and its interaction with its surroundings. To accomplish these goals *Swift* carries three instruments to observe GRBs, a wide field Burst Alert Telescope (BAT) which studies the energy range 15 - 350 keV, a narrow field X-Ray Telescope (XRT) observing the spectrum from 0.3 - 10 keV and a UV-Optical Telescope (UVOT). A key feature of *Swift* is also its ability to slew to the direction of a burst within as little as 100 seconds. Figure 1.5 shows the main parts of the *Swift* satellite.

The BAT is a coded-aperture instrument, which images hard X-rays, but does not focus them, it has a high sensitivity $\sim 10^{-8}$ erg cm⁻² s⁻¹ and a large field of view (2 steradians) over which it searches for possible GRB triggers (Barthelmy *et al.* 2005). The BAT algorithm to detect GRB triggers is based on the algorithm developed for the HETE-II, it looks for excesses ranging from 4 to 11 σ above the background noise with a typical value of 8 σ . The onboard software ensures any that trigger is caused by a point source, eliminating potential trigger sources such as flickering in bright galactic sources and magnetospheric particle events. Once a burst is detected, the BAT provide an initial position with an accuracy

of 1-4 arc-min (Barthelmy *et al.* 2005), the sky location and intensity will be immediately sent to the ground and distributed to the community through the Gamma-ray burst Coordinates Network (GCN). Within 100 seconds of the burst this position is narrowed down to a few arc seconds by the XRT which is also then relayed to the GCN.

The XRT on *Swift* is designed to autonomously measure the fluxes, spectra, and light curves of GRBs and afterglows over a wide range covering more than 7 orders of magnitude in flux. To do this the XRT has 3 operational observing modes and automatically changes between them depending on the GRB's flux. The first mode used is Image mode, which is most useful up to $7 \times 10^7 \text{ erg cm}^{-2} \text{ s}^{-1}$ (Burrows *et al.* 2005). The XRT CCD is operated like an optical CCD, collecting the accumulated charge from the target and reading it out without any X-ray event recognition. For a typical GRB, this image is highly piled up and will therefore produce no spectroscopic data but it will produce an accurate position and a good flux estimate (Burrows *et al.* 2005).

The X-ray data discussed in successive chapters was taken in either Windowed Timing (WT) or Photon-counting (PC) mode. WT mode uses a 200 column window covering the central 8 arcminutes of the field of view (FOV). Imaging information is preserved in one dimension, but the columns are clocked continuously to provide rapid timing information in the trailed image along each column, at the expense of positioning information. This mode has good time resolution (2.2 ms) and also bright source spectroscopy through rapid CCD readouts. It is useful for fluxes below $\sim 10^{-7} \text{ ergs cm}^{-2} \text{ s}^{-1}$ (Gehrels *et al.* 2004). PC mode has complete imaging and spectroscopic resolution, but the time resolution is only 2.5 seconds. PC mode uses a 'normal' CCD readout sequence, in which the entire

CCD is read out every 2.5 seconds, and processed on-board by subtracting a bias map and searching for X-ray events in 5×5 pixel neighborhoods (Burrows *et al.* 2005) around each local maximum pixel. It is useful for fluxes from 2×10^{-14} to 2×10^{-11} ergs cm⁻² s⁻¹ (Gehrels *et al.* 2004).

This thesis seeks to discover more properties of the GRB central engines by examining GRB energetics, to find a GRB's energy it is necessary to have a reliable redshift measurement. GRBs can occur out to $z \sim 15-20$ (Lamb & Reichart 2000), at these redshifts the Lyman cut-off will not be detected in the UVOT, however for redshift $1.5 < z < 4.5$ the UVOT can use the Lyman cut-off to determine redshift. For fainter GRBs ($17.0 < m_B < 24.0$) the photometric redshifts can be acquired by comparing the fluxes in the broadband filters (Roming *et al.* 2005). Also varying optical, UV and X-ray lines and edges are expected within an hour following the burst from the illumination of the immediate (100 pc) environment by the initial burst. The rapid response of Swift enables a search for X-ray lines and thus provide another method to determine redshift (Gehrels *et al.* 2004).

By obtaining a large sample of GRBs over a wide range of fluences and redshifts, *Swift* enables this thesis (in Chapter 3) to seek trends between high and low redshift GRBs in the observer and the rest frame using early-time data and high redshift bursts which were not identified prior to the launch of *Swift*. Most of the data used is either light curve morphology or spectra from either prompt emission seen in the BAT or afterglow emission at later times seen in the XRT. The BAT uses a two-dimensional coded mask and a large-area solid state detector array to detect weak bursts and has a large FOV to detect a good fraction of bright bursts. Hence, the only way to formulate an image is to use a coded-aperture. The BAT coded aperture mask consists of $\sim 54,000$ lead tiles in a random pattern, while

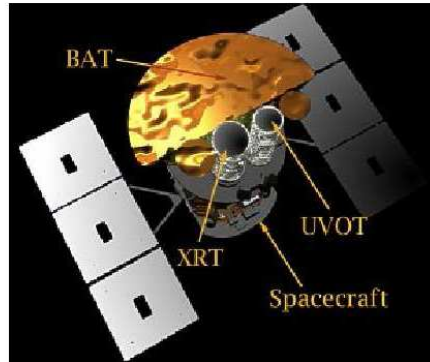


Figure 1.5: A picture of the *Swift* satellite labelled with the BAT, XRT and UVOT. <http://www.swift.psu.edu>

there are 32,768 individual CdZnTe elements in the detector plane. After about 130 seconds, light curve information in 4 energy bandpasses are transmitted. After about 20 minutes the afterglow light curve becomes available with burst event by event data available 3-4 hours after the burst (Barthelmy *et al.* 2005).

An X-ray afterglow is found for 96% of BAT detected GRBs, while the optical/UV afterglow is found for 60% of GRBs (Burrows *et al.* 2008). Prior to the *Swift* mission X-ray and optical afterglows generally began 10^4 seconds after the burst decaying with a temporal index of -1 . When *Swift* started observing its first GRBs, revealing the first 1,000 seconds they found an unexpected steep decline at roughly 100 seconds for example GRB 050125 and GRB 050219A (Goad *et al.* 2006). In fact less than 20% of GRBs follow a gradual decline shown in Figure 1.6 (Evans *et al.* (2010), a canonical light curve⁴ has been observed for many GRBs (Nousek *et al.* 2006, Zhang *et al.* 2006).

A further surprise was that there were far fewer GRB light curves with achromatic jet breaks (Willingale *et al.* 2007, Sato *et al.* 2007), these are caused when

⁴The canonical light curve is the most common light curve shape for GRBs shown by the steep decay in Figure 1.6

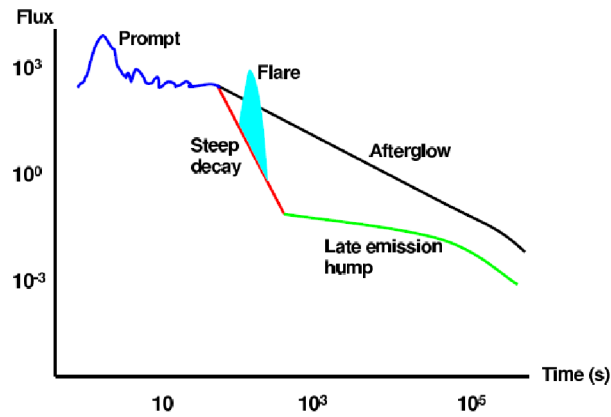


Figure 1.6: A schematic view of the early GRB light curve. After the prompt emission the decay tends to follow one of two paths: A steep decay during which the flux can fall by 3 or more orders of magnitude, followed by a plateau starting between $10^3 - 10^4$ seconds, is known as the canonical GRB light curve. Alternatively it can follow a gradual decay. Either decay path may have flares occurring or can end with a break $> 10^4$ seconds to a steeper decay (O’Brien *et al.* 2006).

the jet stops moving relativistically so that the radiation is no longer beamed, but emitted isotropically so that the flux that can be observed by telescopes decreases. Jet breaks were expected to be seen in most light curves.

Swift also observes flares in $\sim 50\%$ of GRB afterglows (O’Brien *et al.* 2006), including giant flares seen after the T_{90} duration had passed. Such flares are particularly unusual as the fluence of the flare is comparable to that seen during the prompt emission (Burrows *et al.* 2005, Falcone *et al.* 2006).

Swift has localised many short GRBs finding they occur in host galaxies that are either elliptical or irregular galaxies (Prochaska *et al.* 2006). Only a few show evidence for star formation in the host, for example GRB050709 (Fox *et al.* 2005, Prochaska *et al.* 2006), which fits for an old population such as neutron star or black hole mergers.

X-rays from a supernova shock wave were observed during the afterglow of

XRF/GRB 060218/SN2006aj, the rapid slew performed by *Swift* ensured that the supernova was observed at the time of initial core-collapse. Also in addition to the usual non-thermal spectrum a thermal component was also seen and evolved over time (Campana *et al.* 2006).

Other bursts of note include; GRB 090423 one of the furthest objects seen in the Universe at $z \sim 8.2$ (Salvaterra *et al.* 2009, Tanvir *et al.* 2009), GRB 080319 which was bright enough to be seen with the naked eye (Racusin *et al.* 2008), GRB 060614 which cast doubt on the method used to classify long & short GRBs and finally GRB 050509B the first short burst observed with an afterglow.

To date *Swift* has observed over 500 GRBs, the average redshift is a factor of ~ 2 higher than the median redshift for BeppoSax and HETE-II (Berger *et al.* 2005). This is due to the BAT's trigger sensitivity, rapid slewing so that afterglows are observed when they are brighter and also possibly that *Swift* observed different population of GRBs to previous missions (Lee & Dermer 2007).

1.2 The Prompt Phase

1.2.1 Energetics

The prompt emission is radiation that is emitted directly during the burst, this often consists of multiple pulses which can overlap. The energy of a burst is usually given as the isotropic energy found using the fluence of the GRB in gamma-rays, which can be found using Formula 1.1 where e_1 and e_2 are the minimum and maximum energies and $\psi(E)$ is the spectral shape. If two GRBs are at different redshifts the fluence will be measured in two separate rest frame energy ranges,

also two different instruments with different energy ranges will also lead for different values of e_1 and e_2 , this implies that in both of these cases the isotropic energies cannot be directly compared. Thus to compare the intrinsic energies of GRBs in either of these cases a k-correction is applied to give the bolometric energy for all GRBs in the same energy range.

$$S_\psi = \int_{e_2}^{e_1} E\psi(E)dE \quad (1.1)$$

The k-correction is the ratio of the measured GRB fluence between two rest frame energies [$E_1/(1+z)$ and $E_2/(1+z)$] (where z is the redshift) and the fluence measured in the first detector wavelength range (Formula 1.1).

$$k = \frac{\int_{E_2/(1+z)}^{E_1/(1+z)} E\psi(E)dE}{\int_{e_2}^{e_1} E\psi(E)dE} \quad (1.2)$$

Thus for GRBs in the rest frame the isotropic energy can be found using (Bloom *et al.* 2001):

$$E_{\text{iso}} = 4\pi D_1^2 S_\psi \quad (1.3)$$

1.2.2 Beaming

The energy of the first GRB with measured redshift (GB970508) was 7×10^{51} ergs (Metzger *et al.* 1997) which is consistent with the energy observed in a supernova implying a stellar origin for GRBs. However, the very high luminosity leads to a compactness problem caused by the high electron-positron production rate. This can be solved by invoking an extremely high outflow velocity with a Lorentz factor equal to $(1 - (v/c)^2)^{-0.5} \sim 100 - 300$ (Baring 1993, Fenimore, Epstein & Ho

1993).

The approximate opening angle of the jet can be estimated directly by observing jet breaks in the afterglow light curves: a time after which the slow-decaying afterglow abruptly begins to fade quickly as the jet slows down and can no longer beam its radiation as effectively. Jet breaks are discussed in more detail in Section 1.3.1.

The isotropic energy can be corrected for beaming by multiplying it by a factor shown in Formula 1.4.

$$E_{\gamma} = f_b \times E_{\text{iso}} \quad (1.4)$$

where $f_b = (1 - \cos(\theta_j)) \sim 0.5 \times \theta_j^2$ for small θ and θ_j is the opening angle of the jet.

This leads to a narrower range of energies for GRBs i.e. for long bursts the isotropic energy $\sim 10^{51}$ ergs.

1.2.3 Spectrum

The spectrum of prompt emission is non-thermal, for GRBs the spectrum is expected to be produced by synchrotron radiation or inverse Compton radiation⁵. GRB spectra are best fit by a non-thermal synchrotron spectrum with a power law with an exponential cut off at lower energies and a steeper power law at high energies (Band *et al.* 1993).

⁵Inverse Compton radiation is when a photon collides with an electron causing the photon to gain energy.

$$\begin{aligned}\Phi(E) &= \left(\frac{E}{100\text{keV}}\right)^\alpha \exp\left(-\frac{E}{E_0}\right) && \text{for } (\alpha - \beta)E_0 \geq E \\ \Phi(E) &= \left(\frac{(\alpha - \beta)E_0}{100\text{keV}}\right)^{\alpha - \beta} \exp(\beta - \alpha) \left(\frac{E}{100\text{keV}}\right)^\beta && \text{for } (\alpha - \beta)E_0 \leq E\end{aligned}\tag{1.5}$$

This is known as the Band Function (Formula 1.5) where E is the energy in keV, E_0 is the break energy. A is a constant and α is the low energy spectral index and β is the high energy spectral index. GRBs are classified as short, hard or long, soft bursts by their T_{90} parameter and their spectral hardness. Spectral hardness is found using the ratio of the total counts in two energy bands dependent on the instrument used to observe the GRB. During my thesis the hardness ratio for prompt emission detected in the BAT was found using a 25 - 50 keV band and a 50 - 150 keV band, GRB spectra when well resolved shows significant time evolution as demonstrated in Figure 1.7, whereas each pulse evolves from hard to soft (Ryde & Svenson 1999).

1.2.4 Temporal Properties

How the GRB light curve change from pulse to pulse is termed as variability, which typically varies from a few milliseconds to a few seconds. The duration of the prompt emission is measured by T_{90} parameter and for BATSE GRB shows a bimodal distribution as shown in Figure 1.3. In comparison the *Swift* GRB distribution shown in Figure 1.8 does not show evidence of biomodality this is because short GRBs frequently fail to trigger the BAT which requires that the count rate must have increased meanfully above the background level and that

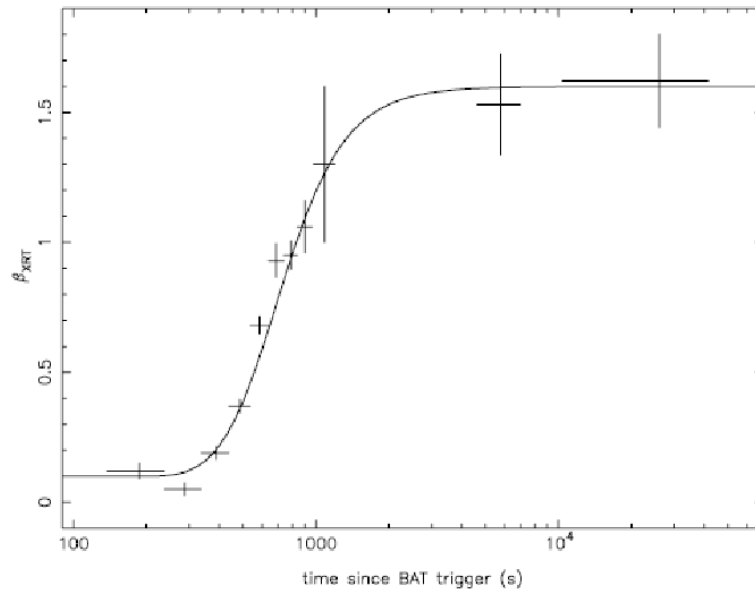


Figure 1.7: The evolution of the X-ray spectral index β_{XRT} with time since the BAT trigger for GRB 070616. GRB070616 had unusually prolonged prompt emission with a T_{90} (15 - 350 keV) = 402 ± 10 seconds. The spectral evolution from the prompt to the afterglow emission is modelled with the curvature model plus an underlying afterglow component (Starling *et al.* 2007).

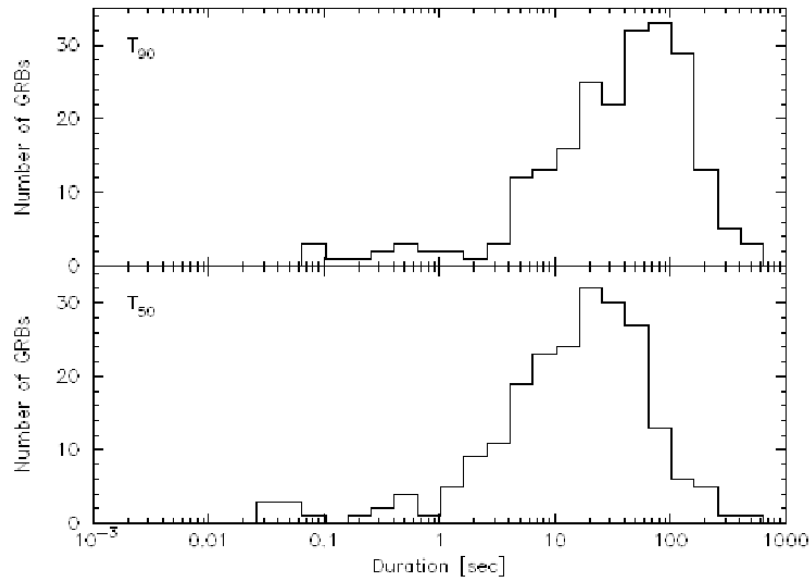


Figure 1.8: The *Swift* distribution of GRB durations, the top panel shows the GRB T_{90} duration; the lack of short GRBs detected is clearly visible compared to Figure 1.3 (Sakamoto *et al.* 2008). The lower panel shows the distribution of the T_{50} duration i.e. the time over which a burst emits from 25% to 75% of its total measured counts.

there must be significant signal in the image. Short GRBs often fail to have enough photons to produce the signal required in the image (Sakamoto *et al.* 2008).

Another reason *Swift* detects less GRBs per year is that BATSE searches for triggers by observing the whole sky that is not concealed by the Earth, whereas *Swift* monitors $\sim \frac{1}{6}$ of the sky. *Swift* sacrifices the all-sky coverage for greater precision; using a high resolution detector it provides positions (to an accuracy of about 3 arcmin) fine enough to aim optical and X-ray telescopes.

1.3 The Afterglow

The prompt emission is followed by the afterglow, which is measured from X-ray to radio wavelengths. The X-ray and optical emission may be seen during or just after the prompt emission and in some cases \sim a month after the GRB. All of the afterglows in this thesis are examined using X-ray afterglows, some optical afterglows are discussed in Chapter 2 Section 2.4. Radio emission is not examined in this Thesis.

Since the launch of *Swift* four main light curve shapes have been seen; canonical, one break, no breaks and oddball light curves. The next section examines the canonical light curve which is the most common afterglow morphology seen in 42% of GRBs (Nousek *et al.* 2006, Zhang *et al.* 2006, Evans *et al.* 2010). GRBs with canonical and other light curves are also discussed in Chapter 3 Section 3.3.

1.3.1 The Canonical light curve

The canonical light curve is shown in Figure 1.6 by the steep decay path, this steep decay has a temporal index between -5 and -3 and is the tail of the prompt emission. Next a shallow decay known as the plateau is seen with a temporal index between -1 and 0 (Liang *et al.* 2007), this is then followed by a normal decay with a temporal index between -1.5 and -1.0 . Finally a steep decay known as the ‘jet break’ (also discussed in Section 1.2.2) with temporal index ~ -2 .

These jet breaks are not always seen in X-ray afterglows (Sato *et al.* 2006), Curran *et al.* (2008) suggests this could be because often at late times the signal to noise ratio is poor or the temporal break in the X-rays is masked by some additional source of X-ray emission (Sato *et al.* 2006). Racusin *et al.* (2009)

finds extra jet breaks assuming the normal decay in the canonical light curve is not necessarily a distinct second section of the light curve and fitting this as a jet break.

The jet break in the afterglow light curve has been argued to be the combination of both the edge of the jet becoming visible and fast lateral spreading. These are both expected to occur at the same time, when the Lorentz factor Γ , of the jet drops below the inverse of the half opening angle θ_o .

When Γ drops below θ_o^{-1} the edge of the jet becomes visible, since relativistic beaming limits the region from which a significant fraction of the emitted radiation reaches the observer to within an angle of $\sim \Gamma^{-1}$ around the line of sight ($\theta \lesssim \Gamma^{-1}$). Once the edge becomes visible then assuming no significant lateral spreading only a small fraction $\Gamma\theta_j^2 < 1$ of the visible region is occupied by the jet and therefore would be 'missing' contributions to the observed flux compared to spherical flow. This would cause a steepening in the light curve called a jet break (Granot 2007).

When Γ drops below θ_o^{-1} the centre of the jet comes into casual contact with its edge, and the jet can in principle start to expand sideways significantly. It has been argued it would then expand sideways rapidly close to the speed of light in its own rest frame. During this lateral expansion the jet opening angle grows as $\theta_j \sim \Gamma^{-1}$, this causes the energy per solid angle to drop with observed time and Γ to decrease faster as a function of the observed time which results in a steepening of the afterglow light curve i.e. a jet break (Granot 2007).

It is important to keep in mind, however, that numerical studies show that the lateral spreading of the jet is very modest as long as it is relativistic (Granot 2007). This implies that jet spreading cannot play an important role in creating a

jet break and the predominant cause of the jet break is the ‘missing contribution’ from the outside of the jet once its edge becomes visible.

The GRB environment also effects the shape of a jet break. Jet structure models in the context of the cocoon in the collapsar model (Ramirez-Ruiz, Celotti & Rees 2002) and in the context of a hydromagnetically driven neutron-rich jet (Vlahakis, Peng & Konigl 2003) have been invoked in order to account for sharp bumps in the afterglow light curves of some GRBs for example GRB 030329 (Berger *et al.* 2003).

Another example is a ‘fan’-shaped jet (Thompson 2005) where a magnetocentrifugally launched wind from the protoneutron star, formed during the supernova explosion in the massive star progenitor, becomes relativistic. The density in its immediate vicinity drops and it is envisioned to form a thin sheath of relativistic outflow.

Swift GRBs are on average at higher redshifts, have smaller opening angles, lower isotropic energies and lower collimated gamma-ray energies compared to GRBs seen before *Swift*. Racusin *et al.* (2009) suggests this could be biasing from detecting jet breaks at late times where a large opening angle and collimation corrected energy output would be required.

In canonical light curves flares are often seen superimposed upon different stages of the decay. Spectral evolution is observed in the first few hundred seconds for light curves that have a steep decay and in which flares tend to be harder than the underlying continuum.

In the collapsar model both rapid rotation and host galaxy metallicity have an effect on the collapse of the progenitor. For a single star scenario achieving both a stellar envelope depleted of hydrogen (which requires a strong wind i.e. high

metallicity) and fast rotating core (low metallicity) seem to contradict each other. It is argued that rapid mixing of hydrogen with helium would cause hydrogen to be converted to helium without ejecting the envelope (Yoon & Langer 2005) and thus without momentum loss (Woosley & Heger 2005).

Without rapid rotation (angular momentum $j = \text{few} \times 10^{16} \text{ cm}^{-2} \text{ s}^{-1}$), the star would collapse a black hole on a hydro-dynamical timescale carrying any internal energy with it. With rapid rotation the mantle has too much energy to fall freely inside the stable orbit. An accretion disk forms with the dissipation of rotational and gravitational energy and will give rise to some sort of mass ejection and electromagnetic display, though a lot of the energy may come out as neutrinos (Svensson *et al.* 2010). Low metallicity keeps the radius of the star smaller and also reduces mass loss, both effects inhibit the loss of the angular momentum of the star.

In the collapsar model the metallicity to a large extent determines the rate of mass loss that is due to the stellar wind in the progenitor star, and thus also the angular momentum loss (Svensson *et al.* 2010). Core-collapse progenitors arising in low metallicity environments support only weak winds and may be able to retain a large fraction of initial rotation.

1.4 The Fireball Model

As discussed in Section 1.1.1 the energy of a GRB is generated by a catastrophic energy release from a stellar object. The progenitors of both long and short GRBs are likely to leave a black hole behind powering flares (although it is possible an unstable magnetar may form temporarily before collapsing to a black hole as

discussed in Chapter 2).

The gravitational energy released by the massive star collapse or merger involves the order of a few solar masses which is converted into free energy on timescales of milliseconds inside a volume of the order of kilometers. The prompt energy is then boosted by continued accretion of gas from the core of the progenitor star or from the debris of the compact merger.

The sudden release of gravitational energy in such a compact volume converts a fraction of that energy to neutrinos and gravitational waves, while a smaller fraction goes into producing a high temperature fireball first theorized by Jeremy Goodman and Bohdan Paczynski. They proposed that an expanding gas (or fireball) of electron and positrons would form along the axis of rotation and that this gas would expand outwards at relativistic speeds.

As it expanded the energy would be transferred from heat to kinetic energy and as the gas cooled the average energy per particle and gamma-ray would decrease. The decrease in the average energy per particle would continue until the gamma-rays would not have enough energy to make new electron-positron pairs to replace the pairs which annihilate. Eventually this would leave only the gamma-rays streaming outwards.

To make the fireball model fit with observational data an amount of protons and electrons was added to the fireball (effectively adding hydrogen the most abundant element in the Universe). After the electron-positrons annihilate, the protons and some electrons survive to form the debris of the fireball. The debris is plasma which has no overall charge as the charge on the electrons cancels out that of the protons.

These left over protons cause the gamma-rays to be trapped in the opaque

(optical depth > 1) cloud of surviving electrons by Compton Scattering. The pressure of the gamma-rays pushes on the electrons causing them to accelerate outward at relativistic speeds.

The protons and electrons that are accelerated by the gamma-rays will travel until they run into the surrounding interstellar medium; it will then start to gather up more matter. When the fireball enters another plasma such as the interstellar medium it creates plasma waves⁶. The interstellar medium is very dilute (with a density $\sim 1 \text{ atom/cm}^{-3}$ (Chaisson & McMillan 1993)); however the fireball quickly gathers enough material to affect its motion.

When the fireball debris and the interstellar medium interact, the forces between the two plasmas are carried by plasma waves and not by the collision of particles. The plasma waves involve large numbers of charged particles moving with each other and colliding together with the particles in the interstellar medium, these collisions create heat.

When the fireball debris and the interstellar medium collide at relativistic speeds, three things occur for a GRB to be created. First the kinetic energy of the protons in the fireball is converted to random motion, then the protons share their energy with the electrons so the electrons are accelerated close to the speed of light also some of the energy also some of the energy is transferred to magnetic fields.

The electrons radiate synchrotron radiation in the form of soft gamma-rays with roughly the energy that is needed to produce a GRB. The emission appears in a continuous spectrum extending over a wide range of wavelengths due to the velocity of the particle.

⁶Plasma waves involve a partial separation of protons from electrons, and large electric fields pulling them back together, there may also be large magnetic fields (Ridpath *et al.* 1997).

1.5 Fireball Model Additions

1.5.1 Jets

The energy needed to produce a typical GRB with the properties observed is between 10^{51} to 10^{52} ergs. To reduce the amount of energy required to produce a GRB that fits observations, it was suggested the radiation is beamed in our direction. This would also imply that there are many more GRBs which are not observed because they are beamed in other directions, a fireball could be produced, but it would be channelled in the direction of the beam.

Two quantities are needed for the theory of the evolution of the jets, the first is the geometric beaming factor which in the simplest jet model is the opening angle of the jet θ_j . The second is the relativistic beaming factor i.e. the emission of a particle that moves with a Lorentz factor Γ being beamed into a cone with opening angle $1/\Gamma$.

Initially the jet is ultra-relativistic ($1/\Gamma < \theta_j$), an observer on the beam only receives information from within the relativistic light cone and has no knowledge about whether the cone outside the emitter is radiating or not. This part of the jet's evolution is equivalent to the isotropic case.

As the jet slows down eventually the relativistic beam becomes wider than the collimation angle $1/\Gamma > \theta_j$. Two effects come into play, firstly the edge effect i.e. the observer starts to feel the deficit of energy per solid angle. Secondly the causally connected region starts to extend the whole jet cone and can keep expanding sideways. The times for the two effects are close to each other or simultaneous depending on the assumption of the unknown expansion speed.

The post jet-break optical light curve should be proportional to $\sim t^{-2}$, much

steeper than the isotropic case $\sim t^{-1}$. A jet break is the natural interpretation for the apparent steepening observed in many GRB optical afterglows. Although behaviour in the asymptotic regime was well-known, the detailed behaviour near the jet break involves complex effects including the jet spreading hydrodynamics.

1.5.2 A non-uniform external medium

The density surround a GRB may not be uniform; an example would be a Wolf-Rayet star producing a stellar wind, where the wind is ejecting material with a constant mass loss rate. Most of the current GRB afterglow data is consistent with a constant density external medium, but a handful of bursts could be well modelled by including stellar wind. An external density jump would be expected where the stellar wind meets the interstellar medium (ISM) outside it, this causes a distinct afterglow signature. The ISM itself may have density fluctuations which would also add impints on the afterglow light curve.

1.5.3 Microphysics

Some bursts such as GRB 010222 have a shallower temporal decaying slope before and after the jet break suggesting $1 < p < 2$ (Cowsik *et al.* 2001). Afterglow model fits assume all the shock parameters p , ϵ_e and ϵ_B do not evolve with time, detailed afterglow fitting seems to be compatible with the idea one or more of these parameters, may evolve with time.

1.5.4 Pair formation, neutrons and other effects

The prompt gamma-rays can form a radiation front which moves ahead of the blast wave, this can interact with the interstellar medium (ISM) so that some of the gamma-rays can scatter back to meet outgoing gamma-rays and generate electron-positron pairs.

The pairs enhance the opacity and can modify the blast wave dynamics considerably. It is likely a number of neutrons are caught in the fireball, if neutrons and protons move at roughly the same speed the neutron shell would lead when the proton shell is decelerated, the trailing proton wave could interact with the neutron tail causing a bump on the light curve.

If GRBs originate in star forming regions the presence of dust grains would cause a new emission component. Some GRBs are associated with a supernova, signalled by a red bump on the optical afterglow light curve. Either the collapse of a giant star or the compact binary merger creates the fireball. The observational evidence for massive stars collapsing to produce a GRB is given in Section 1.1.3. In the next two sections I will go into more detail about the collapsar model and the merger model.

1.6 The collapsar model

There is agreement in the astrophysics community that the long-duration bursts are associated with the deaths of massive stars in a core-collapse supernova event known as a collapsar or hypenova. Collapsars are expected to occur for rapidly rotating helium stars such as Wolf-Rayet stars with masses $< 25 M_{\odot}$ (MacFadyen, Woosley & Heger 2001). Matter from around the core forms an accretion disk.

The infall of the accretion disk material into the black hole is thought to drive a pair of jets along the poles of the rotational axis as the matter density is less in the accretion disk. Matter in the jets are accelerated to relativistic velocities creating a shock wave. When the jet breaks the surface, a shock wave breaks out into the interstellar medium, producing external shocks.

1.7 The binary merger model

This model involves either two neutron stars (NS - NS) or a neutron star and a black hole (NS - BH) merging which results in a short GRB (Paczynski 1986, Eichler *et al.* 1989). The final supernova producing a neutron star is thought to give the system a ‘kick’ which may be large enough to push the binary system outside a small galaxy. Troja *et al.* (2007) found that short GRBs which were followed by a soft episode of emission lie very close to their hosts suggesting that their progenitors were a NS - BH binary, whereas GRBs with no extended external emission have large offsets consistent with a NS - NS merger in a low density environment.

Given the time needed to form a NS - NS or a NS - BH binary, a short GRB is likely to be located in an old stellar population. The binary has to be compact enough that the system will emerge within 13.8 billion years, giving an initial separation between $\sim 10^{10}$ cm and 10^{11} cm. Gravitational radiation will cause the binary system to lose energy and thus spiral inwards increasing the gravitational pull between the compact objects until they collide and merge. The GRB fireball will be produced around the rotational axis by either neutrino emission or magnetohydrodynamical processes (Rosswog *et al.* 2003).

1.8 Long or Short GRBs

Since was launched it has taken observations of a few GRBs that seem to defy the usual classification as either a long or a short burst, these include GRB 050911, GRB 060505 and GRB 060614. Taking GRB 060614 as an example, it was a low redshift burst with T_{90} of 102 seconds, placing it easily past the 2 second criteria for long bursts. A host galaxy was found at $z = 0.125$ with a relatively low star formation rate for long GRBs (Christensen *et al.* 2004, Sollerman *et al.* 2005) and GRB 060614 was a significant distance from this star forming region in a location more commonly associated with short GRBs (Gal-Yam *et al.* 2006).

Other well-observed nearby GRBs had supernovae detected, but this GRB did not, to limits more than a hundred times fainter than previous detections (SN1998bw/GRB 980425 Galama *et al.* 1998, SN2003dh/GRB030329 Stanek *et al.* 2003, SN20031w/GRB031203 Hjorth *et al.* 2003 & SN2006aj/GRB 060218 Campana *et al.* 2006). Finally the BAT spectrum shows a first short-hard spectrum episode of emission lasting 5 seconds followed by an extended softer episode lasting about 100 seconds as shown in Figure 1.9.

GRB 060614 shares some similarities with short bursts, but has important differences such as the bightness of the extended soft episode. If it was due to a collapsar, it is the first indication that a some massive stars fail as supernovae or highly under produce ^{56}Ni . If it was due to a merger, then the bright long lived episode is difficult to explain for a NS - NS merger where little accretionis expected at late times, but it may a NS - BH scenario more easily.

In the next chapter I examine unexpected plateaus in some GRB light curves, I then use the luminosity and duration of these plateaus to place limits on the central

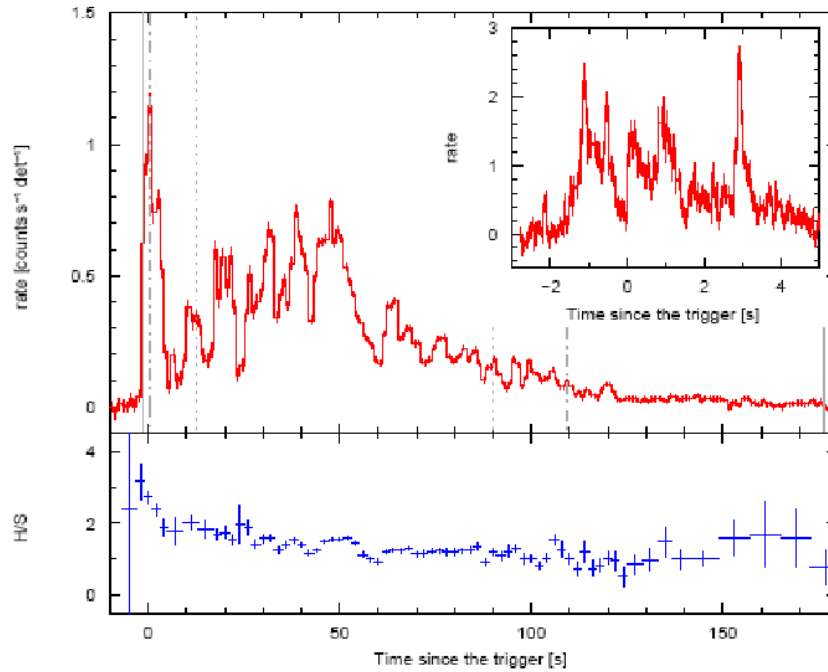


Figure 1.9: The BAT light curve and hardness ratio of GRB 060614. The BAT light curve (15 - 150 keV) at 1 second time resolution is shown in the upper panel, where the solid-dotted line marks the T_{100} interval and dotted vertical lines mark the beginning and end of the satellite slew time. The lower panel shows the hardness ratio of the count rate in the 25 - 150 keV and in the 15 - 25 keV band (Mangano *et al.* 2007).

engine. Chapter 3 investigates GRBs with a redshift detected by *Swift* in the rest frame to search for global trends. In Chapter 4 I examine giant flares and ask if they could actually be the GRB, finally in Chapter 5 I summarise my findings and discuss possible future work.

Chapter 2

Can magnetars power GRBs?

2.1 Abstract

Long duration gamma-ray bursts (GRBs) are thought to be produced by the core-collapse of a rapidly-rotating massive star. This event generates a highly relativistic jet and prompt gamma-ray and X-ray emission arises from internal shocks in the jet or magnetised outflows. If the stellar core does not immediately collapse to a black hole, it may form an unstable, highly magnetised millisecond pulsar, or magnetar. As it spins down, the magnetar would inject energy into the jet causing a distinctive bump in the GRB light curve where the emission becomes fairly constant followed by a steep decay when the magnetar collapses. We assume that the collapse of a massive star to a magnetar can launch the initial jet. By automatically fitting the X-ray lightcurves of all GRBs observed by the *Swift* satellite we identified a subset of bursts which have a feature in their light curves which we call an internal plateau — unusually constant emission followed by a steep decay — which may be powered by a magnetar. We use the duration and luminosity of

this internal plateau to place limits on the magnetar spin period and magnetic field strength and find that they are consistent with the most extreme predicted values for magnetars.

2.2 Introduction

GRBs are thought to be caused by a violent event such as the collapse of a massive star (for long duration bursts) or the coalescence of two compact objects (for short duration bursts). These progenitors result in the immediate formation of a black hole which powers a relativistic jet pointing in the direction of the observer. In the standard fireball model variability in the Lorentz factor of the outflow causes internal shocks which produce the prompt flash of X-ray and gamma-ray emission (Rees & Mészáros 1994; Sari & Piran 1997). When the relativistic outflow sweeps up a sufficient amount of external material, the ejecta is decelerated causing a forward shock which is primarily responsible for the multi-wavelength afterglow emission (Katz 1994; Mészáros & Rees 1997; Sari, Piran & Narayan 1998).

Alternatively there is a model that suggests a black hole may not be formed immediately, but instead that a transitory highly magnetised rapidly rotating pulsar, or magnetar, may form (Usov 1992; Thompson 1994), before the star collapses to a black hole (Rosswog & Ramirez-Ruiz 2003). Proto-magnetars have very high magnetic field strengths of 10^{16} G (Duncan & Thompson 1992; Duncan 1998) which are thought to be a consequence of millisecond rotation at birth in a core-collapse supernova. Values up to $\sim 10^{17}$ G are implied by observations (Stella *et al.* 2005). Such objects are considered a possible central engine for GRBs due to their large rotational energy reservoir, E_{rot} . Also they can be associated with

supernovae, as are long GRBs, and their winds are thought to become relativistic like a GRB jet.

Zhang & Mészáros (2001) investigated the observational signature of a spinning-down magnetar as the GRB central engine. Adopting an approximate magnetic dipole radiation model, they infer that the spindown power of the proto-magnetar could produce a period of prolonged constant luminosity followed by a t^{-2} decay. They considered the modification of the forward shock dynamics by magnetar spindown and predicted a distinct achromatic feature. A similar model was discussed earlier by Dai & Lu (1998) who considered the energy injection to the forward shock by a millisecond pulsar with much a weaker magnetic field. This model is one of the candidates to interpret the majority of the X-ray plateaus observed in many Swift GRB afterglows (Zhang *et al.* 2006; Nousek *et al.* 2006). This model does not invoke the internal dissipation of the magnetar wind. On the other hand, if the magnetar wind indeed dissipates internally before hitting the blastwave, it is possible that it would generate an ‘internal’ X-ray plateau whose X-ray luminosity tracks the spindown luminosity if the energy dissipation and radiation efficiency remain constant. If the magnetar undergoes direct collapse into a black hole before spin down, then the X-ray plateau would be followed by a very steep decay. This is the light-curve feature we investigate and hereafter we call this feature an ‘internal plateau’.

In the *Swift* era the early X-ray light curve, observed within the first few hours of the GRB, has been found to be complex (e.g. Nousek *et al.* 2006; O’Brien *et al.* 2006). The so-called canonical X-ray light curve observed in a significant fraction of GRBs (Evans *et al.* 2009) has a short period of fast decay, often with flares superimposed, which are usually over within the first hour after the burst.

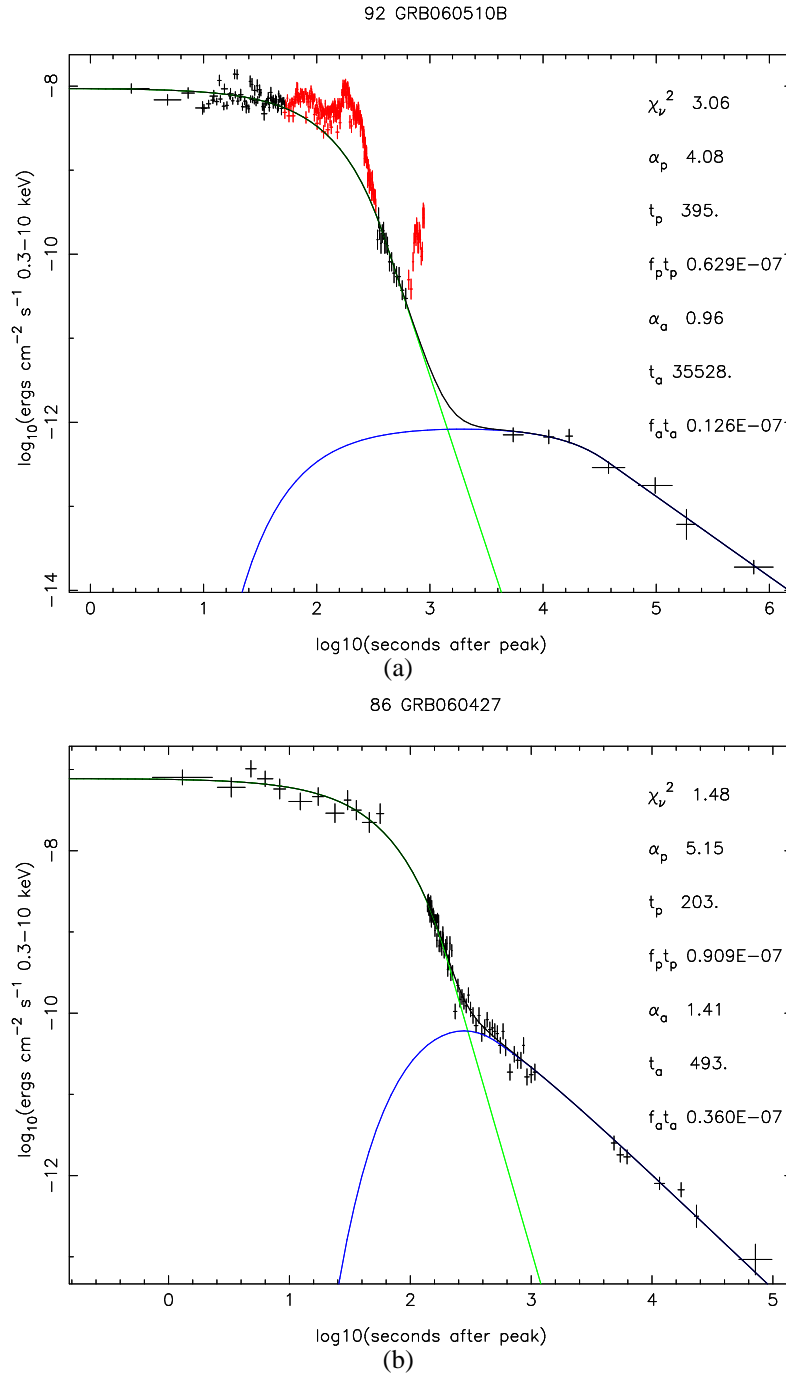


Figure 2.1: The top panel shows the light curve in the BAT and XRT for GRB 060510B and the bottom panel displays a more typical burst; GRB 060427. The green line represents emission from the burst (prompt) and the blue line emission from the afterglow, as given by the Willingale et al. (2007) model. The portions in red in the left panel are the data (flares and internal plateaus) which the model does not fit.

This is followed by a shallower decay period lasting from a few hours up to a day with a temporal decay index $\alpha \sim 0.5$ (where the X-ray flux, $f_\nu \propto \nu^{-\beta} t^\alpha$ and β is the spectral index). After this X-ray plateau there is a smooth transition to a modest power law decay of $\alpha \sim 1 - 1.5$.

Willingale *et al.* (2007) found that the X-ray light curve of most GRBs, including those of the canonical form, can be represented by two components – the prompt and afterglow — plus flares (Section 2). However, we find that in a small minority of bursts a period of relatively constant emission (compared to the general lightcurve) followed by a steep decline can be identified which does not fit this phenomenological model. The observed feature instead resembles the proposed signature of a magnetar spin down. Troja *et al.* (2007) found such a feature dominates the X-ray light curve of GRB 070110 from $\approx 1,000 - 20,000$ seconds in and proposed it was due to a spinning down millisecond pulsar. Starling *et al.* (2008) found a similar, earlier feature in GRB 070616 ending at about 600 seconds. Liang *et al.* (2007) systematically analyzed a sample of X-ray plateaus and identified several more plateaus that are followed by decays with slopes steeper than $\alpha = -3$. It is the combination of a plateau followed by a steep decay which distinguishes these from the canonical behaviour. We regard these objects as candidate internal plateaus.

We have conducted a systematic investigation of the GRB X-ray light curves observed by *Swift* up to the end of 2008. Using an automated fitting procedure in this Chapter we identify 10 bursts which may have an emission component powered by magnetar spin-down dominating the light curve for some period of time in the form of an internal plateau. Assuming this internal plateau is caused by the spinning down of a magnetar we use its properties to constrain the magnetic field

and initial spin period of the magnetar. The criteria for selecting those GRBs with internal plateaus is discussed in Section 2.2. Section 2.3 compares the properties of the internal plateaus with the magnetar model and we discuss the implications in Section 2.4.

2.3 Swift light curves

Over 90% of GRB X-ray light curves are well described by a two component model with a prompt and an afterglow component as described in Willingale *et al.* (2007). These components are described by an exponential that relaxes into a power law; this function can be expressed for the prompt component as shown in Equation 2.1. Large flares were masked out of the fitting procedure. Although apparently bright, such flares account for only about 10% of the total fluence in most cases. The prompt and afterglow emission rises with the time constant t_p and t_a respectively. Later the emission transitions from an exponential to a power law at point (T_p, F_p) , where the subscript p refers to the prompt component of the emission (Willingale *et al.* 2007) or subscript a refers to the afterglow component of the emission. The exponential and power law decay are both controlled by the index α_p or α_a .

$$f_p(t) = F_p \exp\left(\alpha_p - \frac{t\alpha_p}{T_p}\right) \exp\left(\frac{-t}{t_p}\right), \quad t < T_p \quad (2.1)$$

$$f_p(t) = F_p \left(\frac{t}{T_p}\right)^{-\alpha_p} \exp\left(\frac{-t}{t_p}\right), \quad t \geq T_p$$

For this investigation we are interested in those GRBs whose early X-ray emission could not be adequately fitted by the Willingale model. Thus we fitted all the

Swift GRBs with the model and then examined all cases where the model fails.

The X-ray light curves were derived from the BAT and XRT data using the methods described in O'Brien *et al.* (2006) and Willingale *et al.* (2007). BAT & XRT light curves were derived for each GRB using the NASA's HEASARC software. The BAT data were extracted over the 15-150 keV band and the BAT spectra were produced using the task `batbinevt`. An estimate of the fractional systematic error in each BAT spectral channel from the BAT calibration database (CALDB) was added to the spectra using the `batphasyserr` command. The corresponding response matrices were generated by the command `batdrngen`. XRT data were extracted over the 0.3-10 keV band. The light curves were corrected for Point Spread Function (PSF) losses and exposure variations. The XRT spectra were extracted using the `xselect` software and the spectra was grouped to have at least 20 counts per channel. The relevant ancillary response files were generated using the task `xrtmkarf`. data from the Ultraviolet and Optical Telescope (UVOT) was extracted using the task `uvotevtlc`. The V, B, U and white magnitudes were corrected for Galactic extinction along the line of sight and then converted to monochromatic fluxes at the central wavelength of each filter. The effective mid-wavelength was taken to be 4450Å for the White filter.

In Fig. 2.1 we show an example of a GRB that the Willingale model fits well (GRB 060427) and one which it does not (GRB 060510B) and instead demonstrates an internal plateau where the flux remains constant with small fluctuations for about 360 seconds. It has been suggested that instead of a plateau there is a group of flares very close together, however maintaining a high level of flux for hundreds of seconds with the peak of each flare having almost identical flux seems unlikely. Some of the GRBs for which the model fails were those where

a pre-cursor triggered the *Swift* BAT instrument or where very large flares were not fitted. We examined all of the fitted light curves to remove such cases. To be included in the internal plateau sample a GRB must have

1. A lightcurve that could not be adequately fitted by the Willingale model.
2. A significant period of time during which the X-ray flux is relatively constant, i.e. at least a third of a decade long.
3. A convincing steep decline following the internal plateau which falls by a factor of ten where $\alpha \geq 4$, so that the emission is likely caused by central engine activity and is not the canonical X-ray plateau.

This gives 10 GRBs with light curve internal plateau features that resemble the spin-down magnetar model discussed in Zhang & Mészáros (2001).

2.4 Internal Plateau Sample

The 10 GRBs which form our internal plateau sample and values of interest such as the redshift and plateau luminosity are listed in Table 1. For the GRBs with an observed redshift in Table 1, the mean redshift is 3.96, significantly higher than the *Swift* mean redshift of 2.22 for all GRBs with measured redshift. A K-S test with a confidence level of 90% could not prove that the distribution of these redshifts are inconsistent with the *Swift* redshift distribution for all GRBs with measured redshift. The GRBs which display an internal plateau are shown in Figures 2.2 to 2.6 and are discussed briefly below.

GRB 080310 has emission that could be an internal plateau followed by a steep decline, which seems to rise above the underlying emission. Also shortly after the

internal plateau there is a flare which peaks at the same flux as the internal plateau. While in this GRB the proposed internal plateau could be due to a multiple number of flares (Littlejohns *et al.* 2012), we include it in our sample.

GRB 071021 has a possible internal plateau dominating the early X-ray lightcurve. This is the shortest proposed internal plateau in the sample lasting about 105 seconds.

GRB 070721B has a possible internal plateau that dominates early in the lightcurve. Flaring dominates over the internal plateau emission, during the middle of this time interval. This could signify a brief period of accretion onto the proto-magnetar. Ignoring the single flare the emission is similar to that for other internal plateau candidates, so it has been included in the sample.

GRB070616 is intriguing in that the emission rises relatively slowly over 100 seconds to a peak, then persists at a fairly constant level before showing a very rapid decline.

GRB 070129 is similar to GRB 070721B in that it has a possible internal plateau that is interrupted by a flare followed by a steep decline.

GRB 070110 displays a canonical early light curve with an initial steep decline, but then exhibits a period of relatively constant emission. Following this plateau the decay is surprisingly steep ($\alpha \sim 7$) decay (Troja *et al.* 2007). Thus in this case the proto-magnetar survived for much longer than in most of the other GRBs.

GRB 060607A appears to follow the canonical lightcurve with a ‘normal’ X-ray plateau with multiple flares preventing a good fit with the two component model. However at late times the decay following the plateau is too steep for an afterglow and is consistent with $\alpha \sim 4$. This is unlikely to be explained by any-

thing other than central engine activity and thus has been included in the internal plateau sample. As in GRB 070110, the internal plateau seen in GRB 060607A dominates the burst emission unusually late starting at about 900 seconds when (from Table 1) most of the other internal plateaus have ended.

GRB 060510B (also shown in Fig. 2.1) is very similar to GRB 070616. In both cases the proposed internal plateau dominates the emission from the burst very early on.

GRB 060202 displays unusual emission attributed to an internal plateau between 325 and 766 seconds. The fluctuations during this plateau are unusually regular.

GRB 050904 has multiple flares at early and late times, but at about 230 seconds there is a period where the emission appears relatively constant followed by a steep decay, leading it to be included in the sample as a possible internal plateau.

To further investigate the nature of the internal plateau we compared the X-ray data to optical/UV data from the UVOT. The GRBs within the sample with near-simultaneous optical/UV and X-ray light curves are shown in Fig. 2.7. While an early rise in the optical can be seen in some cases, the optical emission does not show the same behaviour as the X-ray. The internal plateau and following steep decay are significantly more prominent in X-rays. For example in GRB 070616, the optical is constant from before the plateau in the X-ray and until after the steep decline.

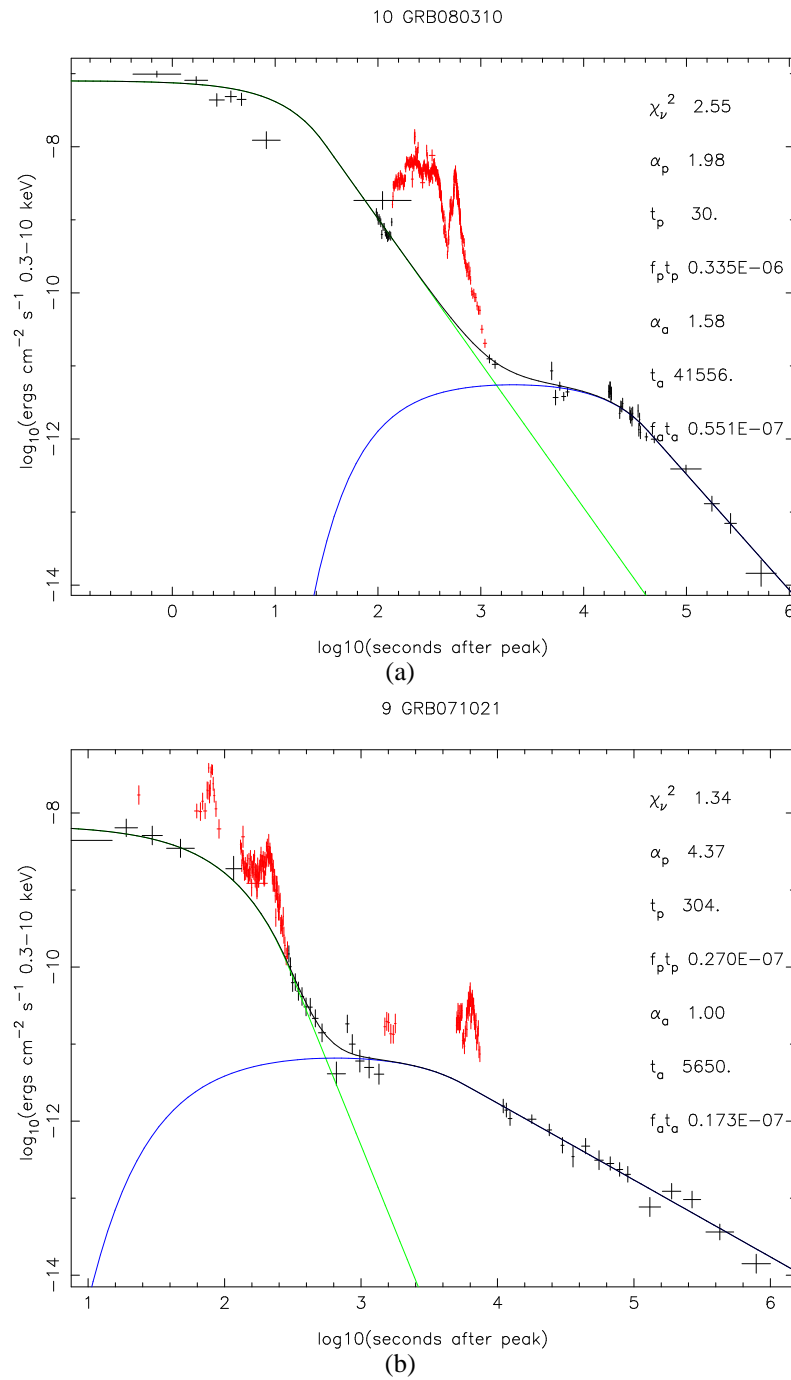


Figure 2.2: The GRB light curves displaying internal plateau behaviour. The green line represents emission from the burst (prompt) and the blue line emission from the afterglow, as given by the Willingale et al. (2007) model. The portions in red are the data (flares and internal plateaus) which the model does not fit.

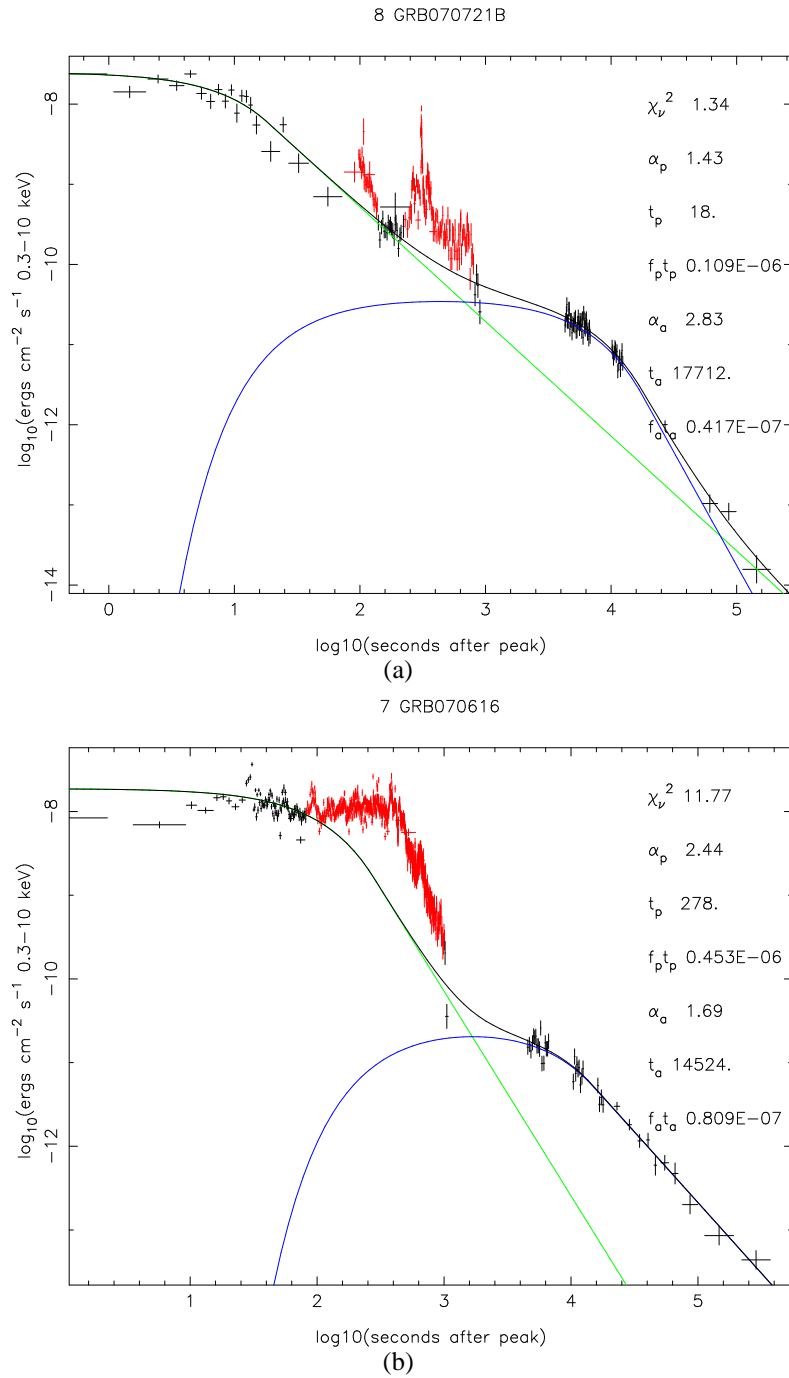


Figure 2.3: The GRB light curves displaying internal plateau behaviour. The green line represents emission from the burst (prompt) and the blue line emission from the afterglow, as given by the Willingale et al. (2007) model. The portions in red are the data (flares and internal plateaus) which the model does not fit.

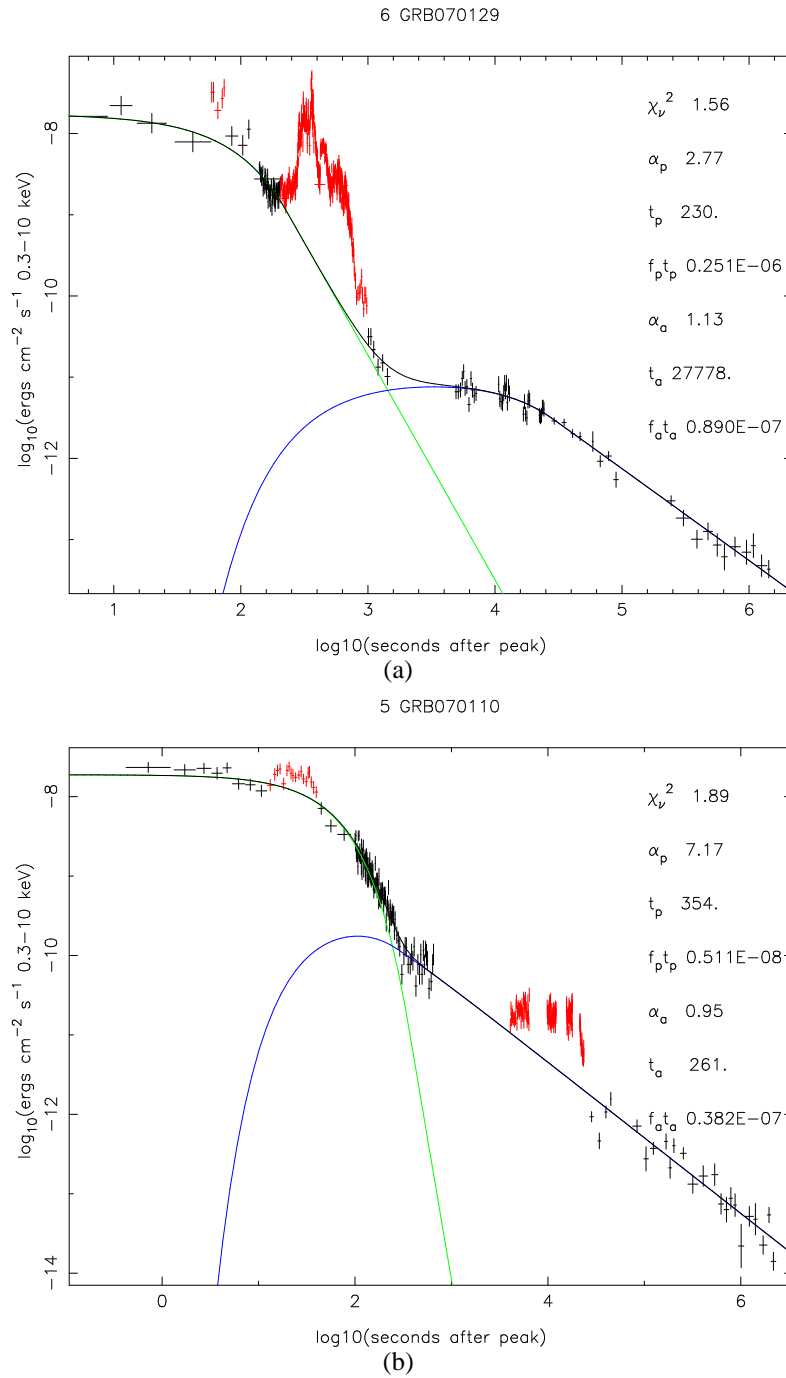


Figure 2.4: The GRB light curves displaying internal plateau behaviour. The green line represents emission from the burst (prompt) and the blue line emission from the afterglow, as given by the Willingale et al. (2007) model. The portions in red are the data (flares and internal plateaus) which the model does not fit.

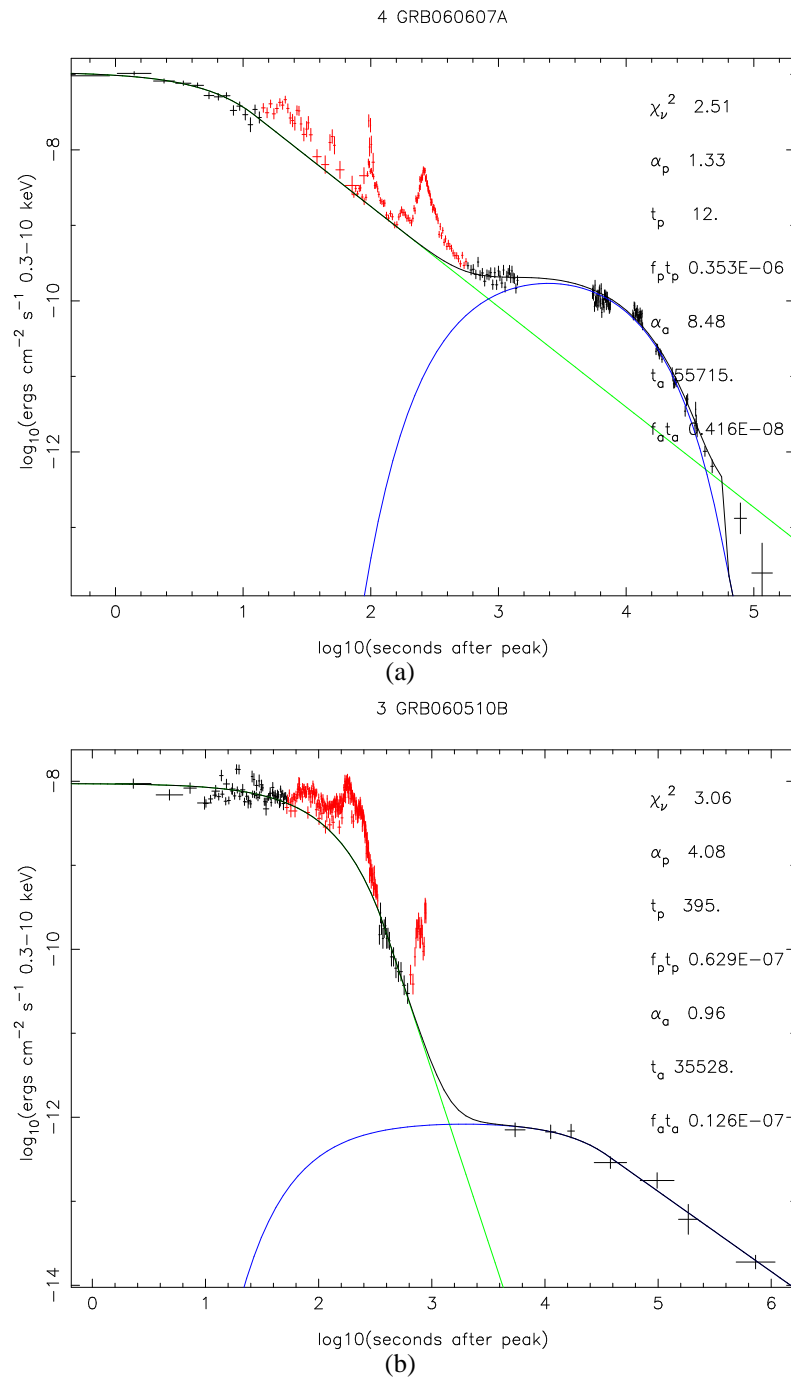


Figure 2.5: The GRB light curves displaying internal plateau behaviour. The green line represents emission from the burst (prompt) and the blue line emission from the afterglow, as given by the Willingale et al. (2007) model. The portions in red are the data (flares and internal plateaus) which the model does not fit.

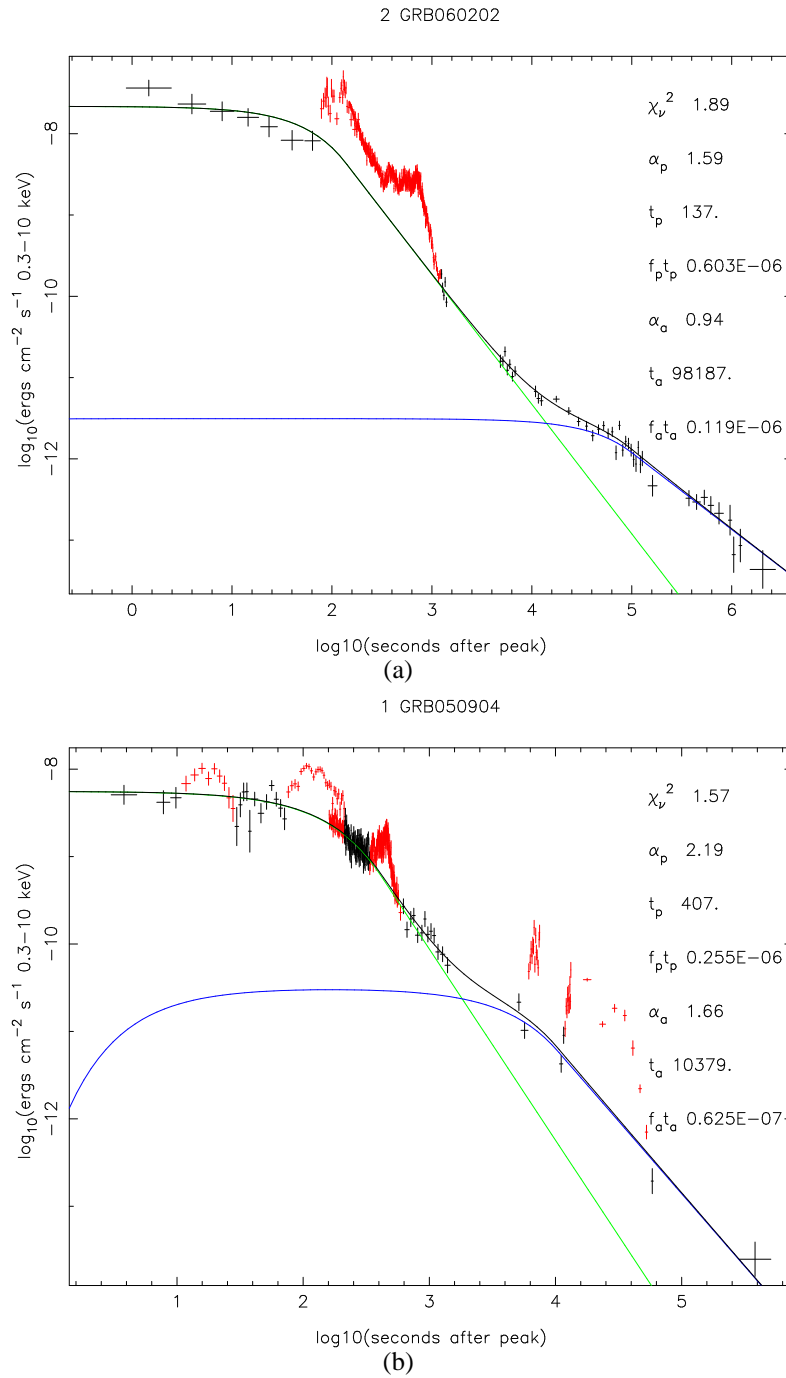


Figure 2.6: The GRB light curves displaying internal plateau behaviour. The green line represents emission from the burst (prompt) and the blue line emission from the afterglow, as given by the Willingale et al. (2007) model. The portions in red are the data (flares and internal plateaus) which the model does not fit.

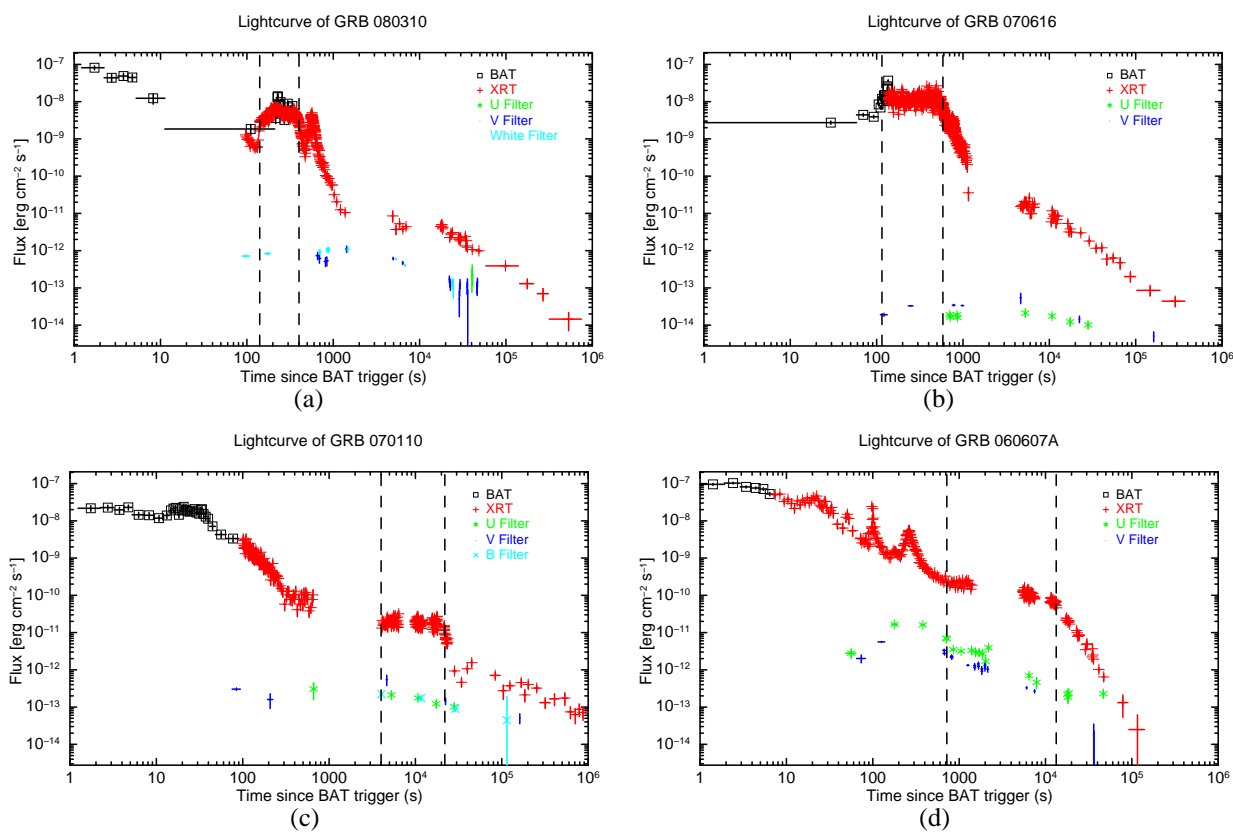
Table 2.1: The observed properties for each of the internal plateaus of GRBs in my sample and also the Steep Decay once the plateau has ended.

GRB	Redshift	Flux ¹ 10 ⁻⁹ erg cm ⁻² s ⁻¹ 0.3-10 keV	Luminosity ¹ erg s ⁻¹	End Time ¹ s	Steep Decay
080310	2.426	5.39	2.6e+50	401.9	11.21 ^{+1.00} _{-0.50}
071021	5.0	2.45	6.6e+50	248.3	9.18 ^{+1.01} _{-0.474}
070721B	3.626	0.24	3.0e+49	802.9	10.31 ^{+1.42} _{-2.696}
070616	2.22*	11.44	4.4e+50	585.6	5.07 ^{+0.13} _{-0.17}
070129	2.22*	2.24	8.6e+49	683.0	7.71 ^{+0.88} _{-0.67}
070110	2.352	0.02	8.8e+47	21887.1	6.98 ^{+0.10} _{-0.34}
060607A	3.082	0.15	1.3e+49	13294.7	3.43 ^{+0.80} _{-0.91}
060510B	4.9	6.58	1.7e+51	362.9	10.43 ^{+0.66} _{-0.58}
060202	2.22*	2.69	1.0e+50	766.0	5.70 ^{+0.17} _{-0.16}
050904	6.29	1.53	7.1e+50	488.8	9.364 ^{+0.91} _{-1.49}

* Where no measurement is available the redshift is assumed to be the mean of *Swift* GRBs taken from the website maintained by P. Jakobsson
<http://raunvis.hi.is/pja/GRBsample.html>

¹ These are parameters related to the plateau, i.e. the end time is the time the plateau ends before the steep decline begins.

Figure 2.7: Combined BAT, XRT, and UVOT light curves for the 4 GRBs with multi-wavelength data during the internal plateau. The vertical dashed lines indicate the time interval over which the internal plateau dominates the emission. The optical data have been scaled down by a factor of ten in panels a and c.



If the plateau seen in each of the X-ray lightcurves is of an external origin, then the X-ray and optical lightcurve should be related to each other in a manner consistent with the external shock model, i.e. the breaks should be achromatic. However, if the X-ray and optical emission components are not related to each other, e.g. a sharp decay in X-ray but no break in optical, this strongly suggests that the X-ray emission is not external or a jet-break but rather is of internal origin.

In Troja *et al.* (2007) for GRB 070110 four spectral energy distributions (SEDs) were examined during the initial decay, the beginning and end of the plateau and during the shallow decay after the steep decline. These SEDs were constructed by extrapolating the X-ray spectrum to the lower energies. During the initial decay the optical data are not consistent with the extrapolation of the X-ray spectrum to low energies. During the internal plateau, the optical and X-ray spectral distributions are also completely inconsistent with one another, implying different origins for the optical and X-ray photons.

For GRB 080310 and GRB 070616 the extrapolation of the X-ray spectrum is also inconsistent with the optical during the internal plateau (Littlejohns *et al.* 2012, Starling *et al.* 2008). Likewise, for GRB 060607A extrapolating the X-ray spectrum to the optical in a similar way to Troja *et al.* (2007) gives a poor fit to the optical (reduced χ^2 of 15.1). From this we conclude that during the internal plateau, the X-ray and optical emission have separate origins for the four GRBs for which we have multi-wavelength data. Henceforth we concentrate on the X-ray behaviour of our sample.

As the time at which the internal plateau ends differs markedly (*cf.* GRB 070110 and GRB 070616) it is possible they have a different origin. Thus we further sub-divide the sample into those GRBs in which the constant emission

phase ends before or after 10,000 seconds. Those which end before 10,000 seconds are denoted as having early internal plateaus whereas those ending after this time have late internal plateaus. In the next section we compare the results for these two groups to determine if their properties are consistent with being caused by the same physical process and whether that process is consistent with being due to a magnetar. Of the 8 GRBs in the early internal plateau group 5 have a redshift measurement as do both GRBs in the late plateau group. For the 3 GRBs with no redshift measurement we adopt a redshift of 2.22, the mean redshift of *Swift* GRBs to determine the luminosity. Our conclusions are not sensitive to this choice.

2.5 The magnetar model

Magnetars are defined as a neutron star where the magnetic field gives the main source of free energy, rather than rotation. The decay of this magnetic field powers electro-magnetic radiation (Duncan & Thompson 1992).

The first recorded observational evidence of this was from a pulse of ‘hard’ gamma-rays detected on 5th March 1979 which were 1,000 times as intense as any previous burst of gamma-rays from beyond the Solar System which is now thought to be from a magnetar (Kouveliotou, Duncan & Thompson 2003). This pulse was followed by fainter ‘soft’ gamma-rays which faded over the next 3 minutes oscillating with a period of 8 seconds. Two objects in theory may be able to produce this energy to power this emission; a black hole or a neutron star, a black hole can be ruled out as it would not be able to produce the 8 second oscillation.

Duncan & Thompson (1992) examined the effect of dynamo action on neutron star magnetic fields and found that if the fluid moving in a newborn neutron star transfers a tenth of its kinetic energy to the magnetic field (the same ratio as is seen in the Sun), then the field would grow to 10^{15} G. The over time magnetic field should slow the magnetars rotation, within 5,000 years a field of 10^{15} G would slow the spin rate to once every 8 seconds (Kouveliotou, Duncan & Thompson 2003), matching the oscillations seen for the March 1979 burst.

The magnetar hypothesis has been accepted as a likely explanation for the observed Soft Gamma Repeaters (SGRs) and Anomalous X-ray Pulsars (AXPs) (Thompson *et al.* 2002, Kaspi 2004, Woods & Thompson 2006), which are distinguished by quiescent, bursting and flaring X-ray emission powered by their magnetic field. In this chapter I am comparing the properties of the GRB central engine for 10 GRBs and comparing them to the limits set for a proto-magnetar, however there is evidence that caution is needed with this approach. McLaughlin, Stairs & Kaspi (2003) report the discovery of a radio pulsar powered by a rotational spin period of 6.7 seconds with a magnetic field of 9.4×10^{13} G, which is in the same range as the anomalous X-ray pulsars which have been identified as being magnetars.

The maximum rotation of a star can be estimated by equating the gravitational attraction at the surface of the star to the centrifugal force tending to throw matter off the star, bearing in mind that matter will be thrown off the star if it rotates too quickly and a stable star would need to rotate below this value. The exact break-up speed depends on the internal conditions of the neutron star, Lattimer & Prakash (2004) estimate this as being > 0.96 milliseconds.

In order to generate the intense magnetic fields required for a proto-magnetar

a massive star's magnetic field must be increased as it collapses through magnetic-flux conservation or efficient dynamo action (Dai & Lu 1998). This can be used to make a prediction for the initial period of the proto-magnetar; every time the star collapses inwards by a factor of two the magnetic fields are increased by a factor of four. To build up sufficient dynamo action on the surface the star needs an initial rotation period of ≤ 10 ms (Usov 1992). The initial rotation period of milliseconds are thought to differentiate between a proto-magnetar and a neutron star. From a theoretical estimate the limits set for the expected strong magnetic field are $B > 10^{15}$ G (Thompson 2007), which is a factor of 10 greater than those found for the unusual radio pulsar discovered by McLaughlin, Stairs & Kaspi (2003).

To place limits on the central object we assume the GRB jet is launched by the collapse of a massive star to a magnetar which survives for a short period of time before it collapses to a black hole (see Thompson 2007 for a review on the magnetar GRB central engine models). A transitory proto-magnetar could cause the flux to remain roughly constant throughout the plateau until the proto-magnetar had spun-down enough for the rotational energy to be insufficient to support the star. It would then collapse to form a black hole ceasing the plateau-like emission and causing the steep decay following the plateau. Flares during the plateau-like emission or the steep decline can arise from accretion onto the central object. We use equations 2.2 and 2.3 (see Zhang & Mészáros., 2001) to relate the continuous injection luminosity of the plateau, L (erg s^{-1}), and the rest-frame time at which the plateau breaks down, τ (s), to the magnetar magnetic field and initial period.

$$L \simeq 10^{49} B_{p,15}^2 P_{0,-3}^{-4} R_6^6 \quad (2.2)$$

$$\tau = 2.05 \times 10^3 I_{45} B_{p,15}^{-2} P_{0,-3}^2 R_6^6 \quad (2.3)$$

Equations 2.2 and 2.3 are produced using the standard adiabatic external shock afterglow model, assuming that the reverse shock is mildly relativistic. At any time the emission at a given frequency may be dominated either by the forward or reverse shock. These equations are derived using the slow cooling regime (Sari, Piran & Narayan 1998) which is usually satisfied. Zhang & Mészáros (2001) also assume the spindown of the proto-magnetar is mainly due to electromagnetic dipolar and gravitational wave radiation.

We use the GRB spectral shape and a k-correction (Bloom *et al.* 2001) to convert the observed 0.3–10 keV flux to the rest-frame 1–1,000 keV luminosity. B_p is the magnetic field strength at the poles where $B_{p,15} = B_p/10^{15}$ G, $P_{0,-3}$ is the initial rotation period in milliseconds, I_{45} is the moment of inertia in units of 10^{45} g cm² and R_6 is the stellar radius in units of 10^6 cm. If we use standard values for a neutron star (Stairs 2004) of mass $\sim 1.4M_\odot$ and $R_6 \sim 1$ then using Equations 2.2 and 2.3 we can infer the central object's initial rotation period and magnetic field strength. The correlation between the derived period and the magnetic field is shown in Fig. 2.8 calculated isotropically ($P_{0,\text{iso}}$ and $B_{p,\text{iso}}$) and with beaming.

Figure 2.8: The initial period and magnetic field for each of the GRBs examined. In the left-hand panel it was assumed that energy was released isotropically, whereas in the middle and right-hand panels it is beamed with an opening angle of 4 and 18 degrees respectively. GRBs with red filled circles have known redshifts and their internal plateaus occur during the prompt emission; GRBs shown by blue filled squares have known redshifts and their internal plateaus occur after the prompt emission; GRBs shown by green filled triangles have internal plateaus that occur during the prompt emission at unknown redshifts, and for which the redshift has been assumed to be equal to the median redshift of the *Swift* sample, meaning their parameters are more uncertain. The light grey shaded regions show limits based on the magnetic field and period limits discussed in the literature. See text for details. The darker grey shaded region shows where a progenitor would be violating the breakup spin-period of a neutron star.

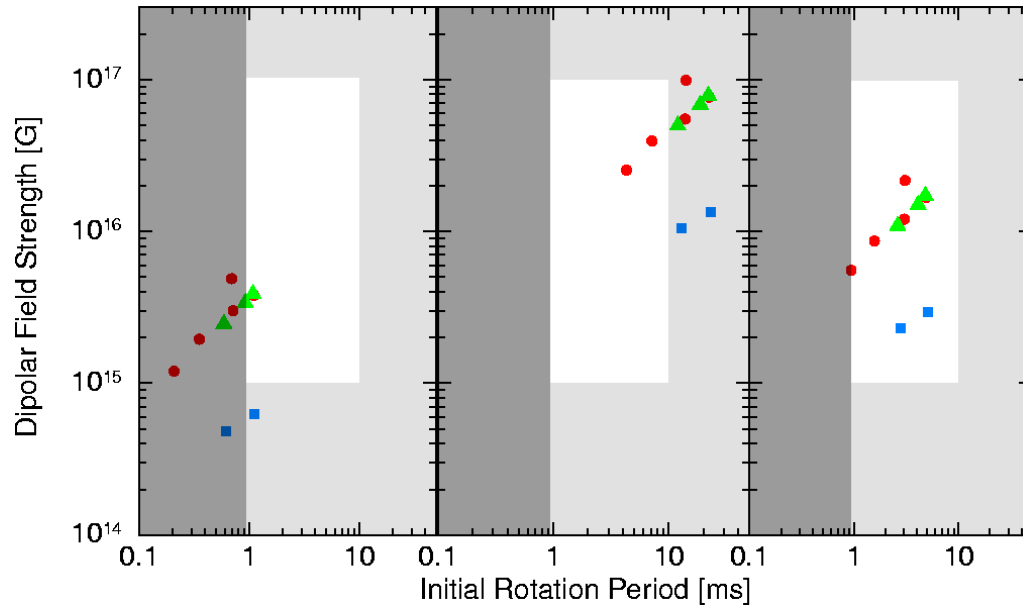
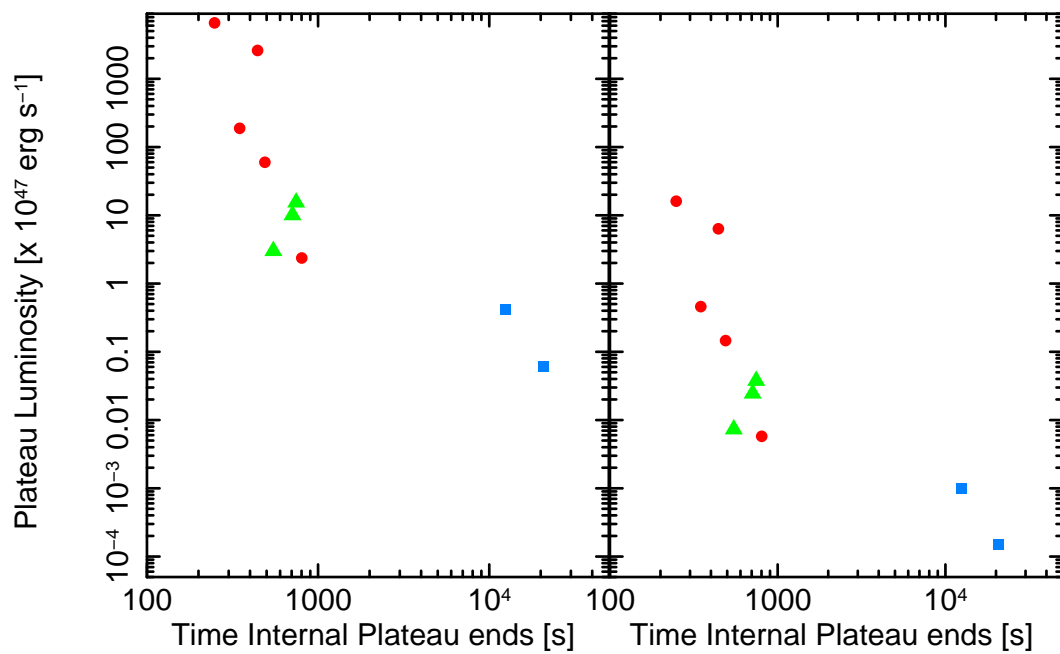


Figure 2.9: The relationship between the length of the internal plateau emission and its luminosity in the observers frame, where it was assumed that energy was released isotropically in the left panel and beamed with an opening angle of 4 degrees in the right panel. GRBs with red filled circles have known redshifts and their internal plateaus occur during the prompt emission, GRBs shown by blue filled squares have known redshifts and their internal plateaus occur after the prompt emission. The GRBs shown by green filled triangles have internal plateaus that occur during the prompt emission at unknown redshifts.



In theory there should be GRBs in the lower right portion of Fig. 2.8 with a relatively long period and low dipolar field strength. From Equation 2.2, a lower luminosity is expected for these GRBs and hence it may be the internal plateau is too faint to be observable. GRBs are unlikely to be present in the top-left as they would require extreme magnetic fields.

The derived periods are close to the sub-millisecond break-up limits for a neutron star, so it could be that most stars cannot support a temporary magnetar and collapse immediately to a black hole. If the initial rotation of the proto-magnetar violated the break-up limit for a neutron star's period it is unlikely it could become stable enough to survive for the lengths of time given in Table 1. This results in a natural boundary on the left-side of Fig. 2.8. Thus only a small group of GRBs may produce an observable plateau and this could explain the apparent correlation in Fig. 2.8.

The rotational energy reservoir of the magnetar given in Table 2 was calculated using Equation 2.4 with $R_6 = 1$ and is consistent with the total power of the internal plateau ($E_{\text{iso,plat}}$) as it should be given the way magnetic field and initial period are calculated.

$$E_{\text{rot}} = 2 \times 10^{52} M_{1.4} R_6^2 P_{0,-3}^{-2} \text{ ergs} \quad (2.4)$$

The plateau energy, $E_{\gamma,\text{iso}}$, was calculated assuming that the radiation is emitted isotropically but it is almost certainly collimated by a relativistic wind flowing through a cavity produced by the elongation of a bubble of plasma and magnetic field (Bucciantini *et al.* 2007). This can be corrected for using Formula 1.4 Chapter 1, Section 1.2.2, where θ_j is the opening angle of the beam. The max-

imum beaming angle ($\theta = 18^\circ$) was estimated by assuming the fastest possible period as the break up spin-period of a neutron star. Taking this angle as the beaming angle for each GRB, the corresponding beaming-corrected energies are shown in Table 2.2 along with an example of the beaming-corrected energies derived using a beaming angle of 4 degrees (Frail *et al.* 2001). A factor which effects the comparison of these energies is that the true initial rotation period is likely to be smaller than that derived from Equation 2.4 (Thompson 2007), so E_{rot} could be larger.

Table 2.2: The different beamed energies found for the plateau for different opening angles compared to the energy of the actual GRB and the energy available in the rotational energy reservoir. All energies in Table 2 are in ergs, the opening angles used to find the beamed energy respectively are 4 and 18 degrees. The GRB E_{iso} values were taken from *Swift* GCN Notices referenced above and in Chapter 6.

GRB	$P_{0,iso}$ ms	$B_{p,iso}$ $\times 10^{16}G$	Beamed P_0 ms	Beamed B_p $\times 10^{16}G$	E_{iso}	E_{rot}	$E_{iso,plat}$	$E_{\gamma 1,plat}$ $\theta_j = 4$	$E_{\gamma 2,plat}$ $\theta_j = 18$
080310	0.7	0.3	13.8	5.5	$2.91e+53^1$	$3.90e+52$	$4.00e+52$	$9.75e+49$	$5.29e+51$
071021	0.7	0.5	14.1	9.9	$3.53e+53^2$	$4.15e+52$	$4.25e+52$	$1.04e+50$	$8.45e+51$
070721B	1.1	0.4	22.3	7.7	$1.72e+53^3$	$1.64e+52$	$1.69e+52$	$4.11e+49$	$1.27e+51$
070616	0.6	0.2	12.0	5.0	$2.47e+54^4$	$5.74e+52$	$2.93e+53$	$7.13e+50$	$1.50e+52$
070129	0.9	0.3	18.7	6.9	$3.98e+53^5$	$2.34e+52$	$1.07e+53$	$2.62e+50$	$5.51e+51$
070110	1.1	0.06	23.2	1.3	$7.08e+52^6$	$1.61e+52$	$1.65e+52$	$4.02e+49$	$1.07e+51$
060607A	0.6	0.04	12.4	1.0	$2.13e+53^7$	$5.35e+52$	$5.48e+52$	$1.34e+50$	$8.89e+51$
060510B	0.2	0.1	4.2	2.5	$1.09e+54^8$	$4.64e+53$	$4.76e+53$	$1.16e+51$	$1.78e+52$
060202	1.1	0.4	22.0	6.9	$3.08e+53^9$	$1.70e+53$	$8.33e+52$	$2.03e+50$	$4.27e+51$
050904	0.4	0.2	7.1	4.0	$2.51e+54^{10}$	$1.61e+53$	$1.65e+53$	$4.01e+50$	$3.17e+52$

¹ Tueller *et al.* 2008 ² Barbier *et al.* 2007 ³ Palmer *et al.* 2007 ⁴ Sato *et al.* 2007 ⁵ Krimm *et al.* 2007 ⁶ Cummings *et al.* 2007 ⁷ Tueller *et al.* 2006 ⁸ Barthelmy *et al.* 2006 ⁹ Hullinger *et al.* 2006 ¹⁰ Sakamoto *et al.* 2005

The correlation between plateau luminosity and duration is shown in Fig. 2.9, which suggests that higher luminosity plateaus are generally of shorter duration. There are too few GRBs in the late internal plateau group to draw any firm conclusions. Their luminosities are lower, but not much lower than that of the early internal plateau group.

The mechanism producing this emission is still uncertain (Metzger *et al.* 2011), however if the emission is internal as suggested in the previous section it could be produced by forced reconnection at the forward shell (e.g. Lyubarsky 2003, 2005; Thompson 2006; Zhang & Yan 2011) or by upscattering forward shock photons (Panaitescu 2008). Alternatively if the emission, which while not certain is found to be external despite the steep decays it could be generated by refreshing the forward shock (e.g. Granot & Kumar 2006; Dall’Osso *et al.* 2010).

2.6 Discussion

We have identified a small number of GRBs which display a period of time during which the X-ray emission shows a smooth plateau followed by a steep decline. The internal plateau is challenging to interpret using accretion models as it requires a constant power jet component with a roughly constant radiation efficiency. This possibility has been examined by Kumar *et al.* (2008a), who suggest that the prompt emission of a GRB may be caused by the accretion of the outer regions of a stellar core and that the X-ray plateau could be caused by the fall-back and accretion of the stellar envelope. This model has problems accounting for the steep declines seen after the plateau. Even assuming a sharp edge to the region being accreted, the steepest decline expected is $\alpha \sim 2.5$ (Kumar *et al.* 2008b).

Here we argue that a more natural explanation may come from the magnetar model which predicts a period of constant spin-down power. This model starts with the assumption that the neutron star accretor can power the GRB prompt emission which while not certain, is feasible (Usov 1992; Thompson 1994; Bucciantini *et al.* 2007). Comparison of the luminosity and duration of the internal plateaus observed in our GRB sample with the dipolar spindown law (Zhang & Mészáros 2001) implies upper limits to the magnetic field strengths close to the maximum allowed for such objects and initial spin periods also close to the maximum allowed to maintain neutron star structural integrity. The upper limits for the dipolar magnetic field of the magnetar are particularly strong if the emission is strongly beamed.

The largest magnetic fields implied for isotropic emission are consistent with field strengths of $\times 10^{16}$ G which can be generated in magnetars born with spin of a few milliseconds (Thompson & Duncan 1993; Duncan 1998). A giant flare from SGR 1806-20 on 27th December 2004 demonstrated that unless such flares are much rarer than the rate implied by detecting one, magnetars must possess a magnetic field strength of $\sim 10^{16}$ G or higher. Indeed values up to $\sim 10^{17}$ G could not be ruled out (Stella *et al.* 2005). For the GRB sample in this paper this could allow beaming factors corresponding to jet opening angles of 4-10 degrees, consistent with values derived from Frail *et al.* (2001).

The number of GRBs that display internal plateau behaviour is very small. This perhaps is not surprising as we would expect them to only be detectable for quite a narrow combination of magnetic field strength and initial spin period. These rare features do provide limits on the magnetic fields surrounding the central engine around the GRB, and can help advance understanding of the mecha-

nisms behind prompt emission.

Chapter 3

The properties of GRBs at known distances

Abstract

In this chapter I study a sample of GRBs with a known distance and correct these GRBs to redshift zero, so that a range of properties such as the light curve morphology can be scrutinized for new correlations. As an extension these GRBs are then subdivided into those with flares and those with plateaus. The method used in Chapter 2 Section 2.4 is then applied to these plateaus to find parameters of the central engine, however we do not find any link between these parameters and flare behaviour.

3.1 Introduction

In this chapter I investigate all GRBs with a redshift measurement that are detected by *Swift* up to the end of April 2009. Gamma-ray bursts have been suggested as

potential cosmological probes of the Universe partially due to the huge distances from our galaxy at which they can occur, for instance the furthest long GRB detected is GRB 090423 which has a redshift of 8.2 this corresponds to a distance of 13.035 billion light-years from Earth.

Lamb *et al.* 2007 calculates the limiting redshift (z_{lim}) detectable with *Swift*, BATSE and HETE-II for 15 GRBs with well determined redshift and peak photon number fluxes. The number of these 15 GRBs that are observable (N_{obs}) at each redshift is displayed in Figure 3.1. Figure 3.1 shows that BATSE and HETE-II would be able to detect half the GRBs out to a redshift of 20, whereas *Swift* should be able to a redshift of 70, although that is unlikely that GRBs would occur at such high redshifts as there would not have been enough time to form stars as shown in Figure 3.2.

The star formation rate for the first stars (Population III stars¹) is thought to peak at redshifts $16 \geq z \geq 20$, while for Population II stars² there is a much larger and broader peak at redshifts of $2 \geq z \geq 10$, so it would be expected that GRBs would occur out to redshift 10 or possibly 15-20. Figure 3.2 shows where GRBs occur in the early universe compared to the most powerful cosmological probes currently being used called Quasars³ or Quasi-Stellar Objects (QSOs).

Gamma-ray bursts would have a few advantages over quasars as a cosmologi-

¹Population III stars are a hypothetical generation of stars, assumed to have been formed before Population II stars as their supernovae is required to produce the heavy elements seen in Population II stars (Ridpath *et al.* 1997).

²Population II stars are the oldest stars we see in the sky today and have fewer heavy elements than younger stars like the Sun. (Ridpath *et al.* 1997)

³A quasar is an object with a high redshift which looks like a star, but is actually the very luminous active nucleus of a distant galaxy. One of the oldest quasars ($z=6.28$) displays a Gunn-Peterson trough (a feature in the spectra due to the presence of neutral hydrogen, where electromagnetic radiation is suppressed) and have absorption regions in front of them indicating the intergalactic medium at that time was neutral gas(Becker *et al.* 2001).

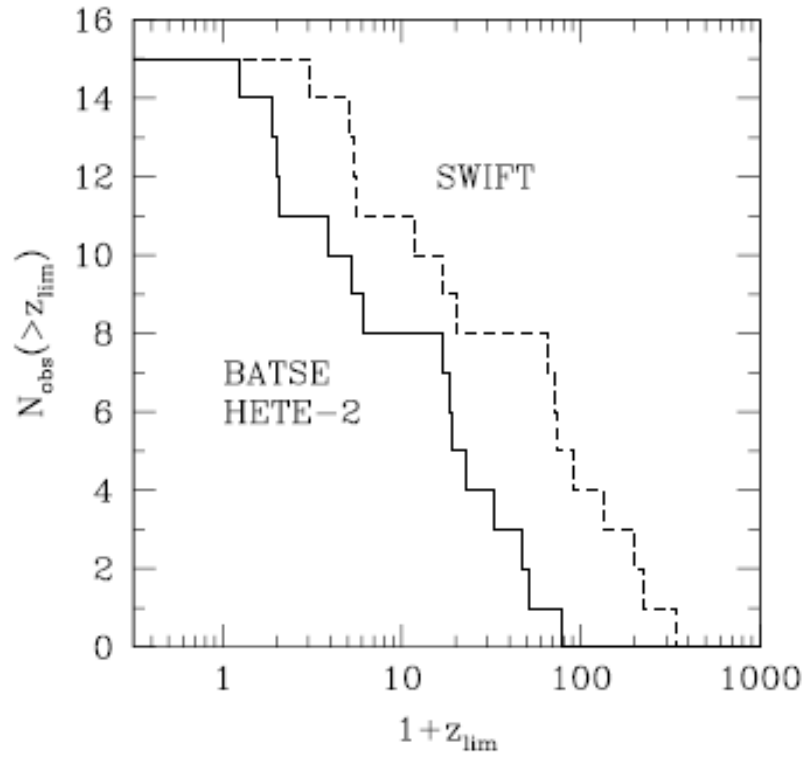


Figure 3.1: The cumulative distributions of the maximum redshifts at which 15 GRBs redshifts and published peak photon number fluxes would be detectable by BATSE, HETE-II and *Swift* (Lamb 2007).

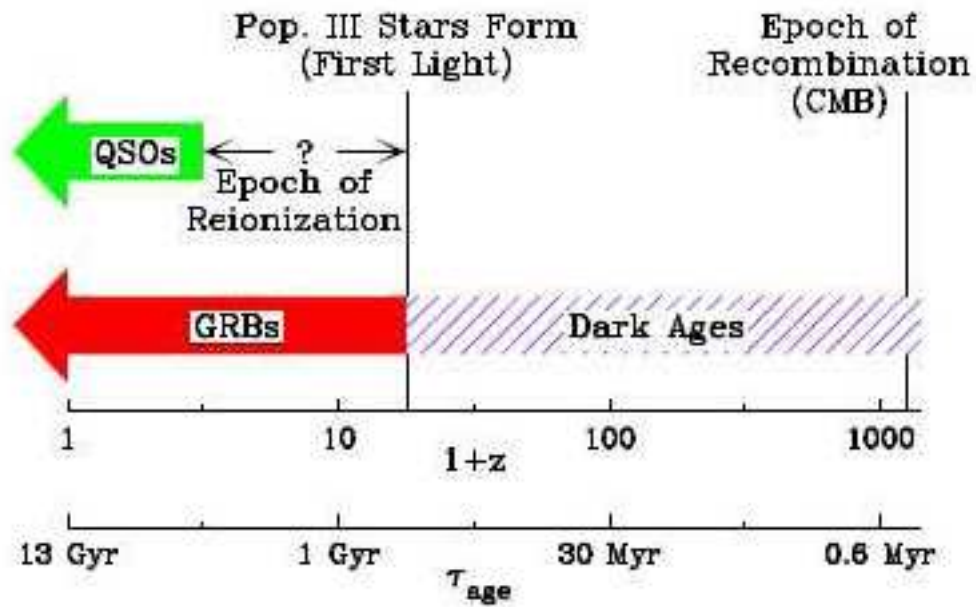


Figure 3.2: A diagram to place the maximum expected redshift of GRBs and Quasars in a cosmological context. The epochs of first light and re-ionization are shown on a scale of redshift and the age of the Universe (Lamb 2007).

cal probe, firstly GRBs have been detected out to a higher redshift. The afterglows can be from 100 to 1,000 times brighter at early times than quasars at high redshifts (Lamb *et al.* 2007). Finally quasars are strong UV sources often causing the ultraviolet background field to rise locally (Dall’Aglia, Wisotzki & Worseck 2008).

Type Ia supernovae are also used as cosmological probes, with the advantage that they each explode at the same mass, however they have a systematic error due to the uncertainties in dust extinction, whereas GRBs penetrate the dust avoiding these errors. The main difficulty using GRBs as cosmological probes is that their energy varies over three orders of magnitude and GRBs have very different properties.

For the first four years that *Swift* was operational it found either photometric or spectroscopic redshifts for $\sim 30\%$ of GRBs. In this study I only deal with known redshifts, consequently $\sim 70\%$ of bursts are excluded, also the derived star formation rate may be biased by the spectroscopic redshift effects (Xiao & Schaefer 2009).

For bursts without a redshift measurement a solution is to search for luminosity indicators, that link a measurable property of the prompt emission to the burst’s redshift, energy or peak luminosity. The observed fluence or peak flux can then be used (with the inverse square law) to derive a distance to the burst and the burst’s redshift for a given cosmology. The advantage is that it applies to all long GRBs, the disadvantage is that currently the uncertainties on the derived redshifts are much larger than those of the spectroscopic redshifts.

3.1.1 Light Curve Shape

One of the aims of this chapter is to examine light curve morphology for redshift indicators. With the launch of *Swift* the first 1,000 seconds of GRB light curves could be observed and subsequently a trend in GRB light curves was seen and so the canonical light curve was proposed (Nousek *et al.* 2006, Zhang *et al.* 2006 and Panaitescu *et al.* 2006). Nousek *et al.* (2006) noted that this behaviour is not seen in all afterglows and suggested this could be due to limited temporal coverage.

O'Brien *et al.* (2006) showed that the prompt emission seen in the BAT smoothly transitions into the emission seen in the XRT (discussed in Chapter 1, Section 1.4). Willingale *et al.* (2007) interpreted this as the combination of two components both decaying as an exponential relaxing into a power law. The first representing prompt emission and the second afterglow emission, under this model not all GRBs would exhibit all the segments of the canonical afterglow. For example the afterglow component can be sufficiently weak that it never dominates the prompt emission.

Evans *et al.* (2009) includes minor revisions from the automatic analysis software first presented in Evans *et al.* (2007). The updated software is used to produce high-precision positions, light curves and spectra for all *Swift* GRB data taken using the XRT up to the end of 2008, providing a sample of 318 GRBs. Evans *et al.* (2009) examines these GRBs in the observer frame as there was not enough redshift information to translate to the rest frame for most bursts.

In Evans *et al.* (2009) light curves are binned using the same criteria (defined in Evans *et al.* (2007)), the advantage is that light curves were generated in a uniform way, but also introduces the limitation that the binning is not always the

best representation of the data for an individual GRB.

The first group of early data taken in Photon-counting mode for the light curve is found using the analysis software on SPER data, which was designed for detecting a source and localizing it; no good time intervals are recorded. Thus to produce each light curve it is assumed that the data is continuous, this is a safe assumption unless the XRT switches back into Windowed Timing mode.

The method used to produce *Swift* light curves was automated and presented with analysis for 318 GRBs in Evans *et al.* (2009). This sample was reduced so that only light curves which had enough data that three phases of the canonical light curves could have been expected to be seen, also only light curves with at least 20 bins of data were included. The morphologies seen for these 162 light curves shown in Figure 3.3, 4% have no breaks, 30% have one break, 42% are canonical and 24% are oddball light curves.

The canonical light curve is described in detail in Chapter 1 Section 1.3.1, oddball light curves are by their nature unusual and cannot be summed up as a single group with common properties, and the findings from Evans *et al.* (2009) for the other light curve morphologies are discussed below.

Evans *et al.* (2009) finds light curves with no breaks (panel d) consistent with the Willingale Model providing we are observing the only power law phase of the light curve. Evans *et al.* (2009) finds that the lack of a steep decay phase is either due to the afterglow being bright enough to dominate at an early time or the prompt emission decaying very rapidly. Also that the lack of a plateau implies no energy injection, the outlier in this group is GRB 051221B, I do not examine this GRB as it has no redshift.

For light curves with one break and shallowing decays (panel b) Evans *et al.*

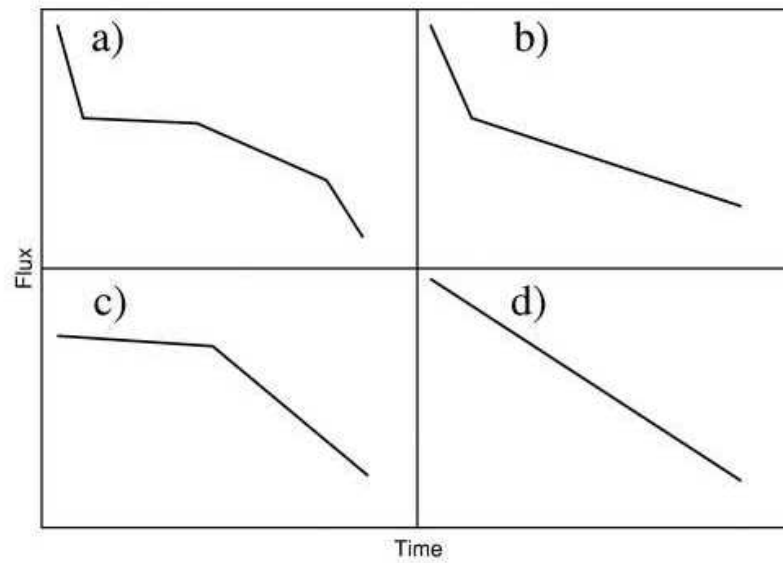


Figure 3.3: A schematic diagram of the different GRB morphologies (Evans *et al.* 2009). Panel a shows canonical light curves (also shown in Chapter 1 Section 1.1.4 Figure 1.6 Steep decay path), panels b and c show light curves with one break either flattening b or steepening c, panel d shows light curves with no breaks. Evans *et al.* (2009) also defines any light curves that do not fall into one of these morphologies as oddball light curves.

(2009) mentions that this behaviour could be described by the canonical model if the shallow phase is similar to the plateau phase. If so, it is at a lower rate of counts per second and is longer lived, continuing to the end of *Swift* observations in most cases ~ 1 day. Evidence of central engine activity injecting energy > 1 day has been seen in GRB 050502B (Falcone *et al.* 2006) and GRB 080810 (Page *et al.* 2009).

For light curves with one break and steepening decays (panel c) Evans *et al.* (2009) finds it unlikely that they correspond to the normal and post jet break phase of the light curve, due to the early time the break would need to occur ($\sim 1,000$ seconds). Evans *et al.* (2009) also finds it unlikely that they are drawn from the same population as Figure 3.3, panel b. One break steepening light curves were examined with the traditional plateau and normal decay following it, from the K-S test; there is 40% chance the steepening decay and the normal decay after a plateau represent the same population of times, but only a $< 0.1\%$ probability the decay slopes of the traditional plateaus and the shallowing behaviour (in Figure 3.3, panel c) are from the same population.

Other conclusions from this study that are relevant to this chapter are that each of the light curve morphologies can be explained by the Willingale Model. Also that there is energy injection in the plateau phase of the canonical light curve in agreement with previous studies (Nousek *et al.* 2006, Zhang *et al.* 2006 & O'Brien *et al.* 2006) and that some mechanism must cause a steepening of the light curve independent of energy injection, which must not cause any spectral change. Finally that there must be energy injection between the plateau and normal decay following it.

3.1.2 Prompt Pulses

As an extension to this chapter GRBs are divided into GRBs with flares and also GRBs with plateaus. The flares are then fitted with a prompt pulse fitting model. One of the key strengths of the *Swift* satellite over previous missions is the ability to observe the first 1,000 seconds of a GRB (Chapter 1 Section 1.1.4). The XRT has detected 95% of BAT detected triggers, this facilitated the study of the end of the prompt emission and of the early afterglow as discussed in Chapter 1 Section 1.3. For many GRBs a rapid decay phase which seems to be the smooth spectral and temporal continuation of the prompt emission (O'Brien *et al.* 2006). This suggests that this Rapid Decay Phase (RDP) is the tail of the prompt emission.

Several models have been proposed to explain this tail including the cooling of a hot cocoon around the jet (Pe'er *et al.* 2006) or a highly radiative blast wave which discharges hadronic energy in the form of ultra-high cosmic ray neutrals and escaping cosmic ray ions (Dermer 2007). However, the first would not apply to short GRBs and the later is unclear if it can simultaneously interpret the observed light curves and spectral evolution of the RDP. The most popular model is High Latitude Emission (HLE) or 'naked' GRB emission, which take place in areas of very low density interstellar medium (Fenimore *et al.* 1996, Kumar & Panaitescu 2000, Qin *et al.* 2004, Dermer 2004, Zhang *et al.* 2006 and Liang *et al.* 2006).

During HLE radiation is received from a region along the line of sight to the observed with an angular size Γ^{-1} , emission from higher latitudes $\theta > \Gamma^{-1}$ which is received over timescales that are long compared to the duration of the burst and away from the observer, however is at a significant magnitude detectable by *Swift*

for about an hour after the burst (Kumar & Panaitescu 2000). During HLE the temporal index of the decline cannot be larger than about 3, also spectral evolution is not expected.

GRB 060218 (Campana *et al.* 2006, Ghisellini *et al.* 2006) and GRB 060614 (Gehrels *et al.* 2006, Zhang *et al.* 2007 and Mangano *et al.* 2007) are two unusual GRBs detected by *Swift* in addition to that previously discussed in Chapter 1 Sections 1.1.4 & 1.8 respectively, they also show strong spectral evolution in the RDP. In the light of this Zhang, Liang & Zhang (2007) performed data analysis during the RDP of the light curves and spectra of 44 GRBs fitted with three models to investigate if additional components could be acting in the early afterglow.

The 44 GRBs were divided into 3 groups, Group A which showed no spectral evolution, Group B which have hard-to-soft evolution without flares and the remaining GRBs into Group C that have flares superimposed upon the tail. From the overall sample 33 of the GRBs showed clear hard-to-soft spectral evolution, thus the simplest HLE alone could not explain this feature. Zhang, Liang & Zhang (2007) fit each of their models to the tails that have smooth decline.

The first model examined was the curvature effect of a structured jet, successfully fit the 11 GRBs with no spectral evolution, but was unable re-produce the light curves of GRB 060218 and GRB 060614. The second model was the superposition of the curvature effect with an underlying power law, an afterglow-like soft component was seen between $10^4 - 10^5$ seconds for GRB 060218, this model failed to re-produce both the light curves and the spectral index evolution for GRB 060218 and GRB 060614. The third model was for the curvature effect using an evolving exponential spectrum with a cut-off energy, this is given by $E_c = E_0(t/t_0 - 1)^{\alpha_2}$, t_0 should correspond to the beginning of the internal shock

emission phase, where α_2 is the temporal index of the RDP. E_0 is the cutoff energy of an exponential cutoff power law spectrum.

The flickering features in some light curves make the reduced Chi-squared much larger than unity. This indicates that to describe the prompt pulse model a solution is needed that includes HLE. The evolution of the prompt pulse and the addition of the emission from several pulses so that the flux can be predicted from the prompt phase to later in the XRT light curve.

3.2 Method

3.2.1 K-corrections

As described in Chapter 1, Section 1.2.1 to compare energy, bolometric fluence or flux of two GRBs at different redshifts entails more than to allow for the inverse square law dimming, since the spectrum from these bursts would be redshifted by different amounts. Thus a k-correction is required given by Formula 1.3 (Chapter 1 Section 1.2.1), for comparison Figure 3.4 shows the uncorrected and corrected energies of a group of GRBs, the typical estimated uncertainty for a k-correction energy measurement is $\sim 20\%$ (Bloom *et al.* 2001).

A script provided by Dick Willingale was used to calculate the k-corrections, this script required the peak energy, redshift, break energy, energy range and also the flux measured in the BAT and XRT. The break energy was assumed to be 20 keV and the peak energy (E_p) was assumed to be 116 keV when none was recorded as this is the median peak energy for *Swift* GRBs. The high energy spectral index was also assumed to be 2.3, the rest of the inputs were taken primarily from an

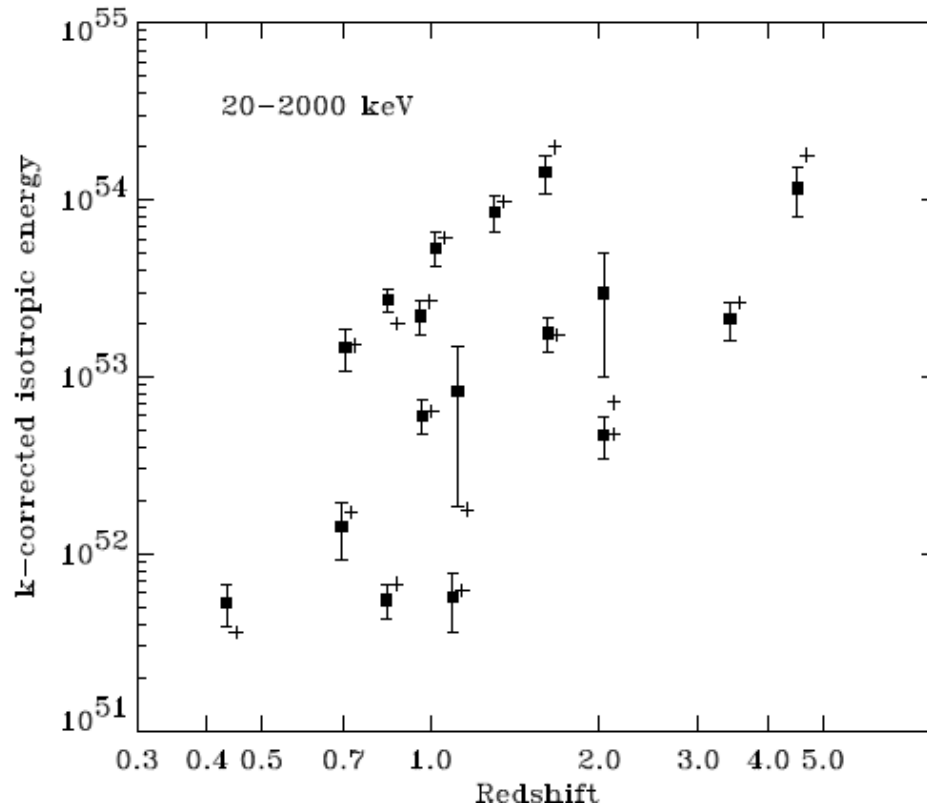
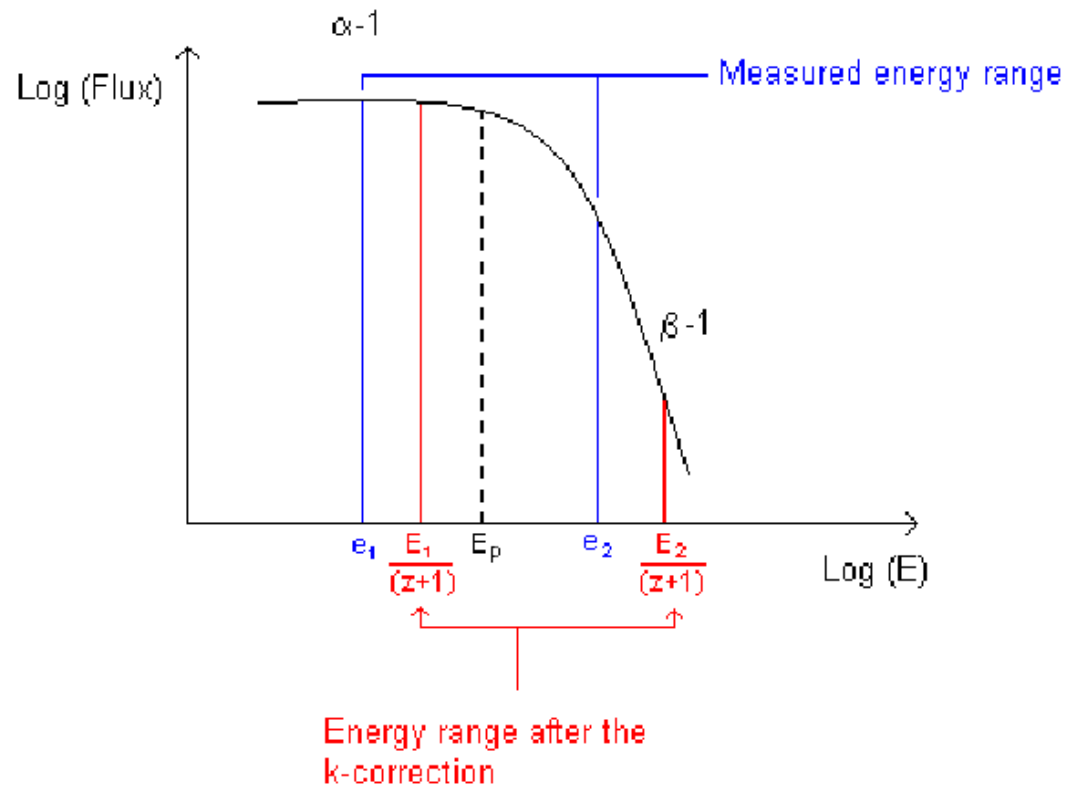


Figure 3.4: The energy release over 20-20,000 keV of 17 cosmological GRBs. The k-corrected energies and their estimated errors are indicated by dark squares and the uncorrected energy by a cross (Bloom *et al.* 2001)

online spreadsheet for all *Swift* GRBs compiled by Kim Page and where necessary from GCN reports for each GRB.

The script finds the k-correction by taking the ratio of the desired energy range to the energy range observed where the desired energy range is outside the range measure as is shown in Figure 3.5. The energy range observed for the BAT is 15-150 keV and for the XRT is 0.3-10 keV, a separate k-correction is calculated for each instrument which can be used from 10-10,000 keV.

Figure 3.5: A schematic diagram of a GRB's flux and energy, which has been annotated with some of the parameters used to find each k-correction. Figure 3.5 also shows the measured energy range detected using *Swift* compared to the k-corrected energy range.



In Figure 3.5 $E/(z+1)$ takes the energy range you want to correct the spectra to and applies a redshift shifting it into the observed frame, then the program uses Formula 1.2 (Chapter 1 Section 1.2.1) to calculate the k-corrections. The spectral data for GRBs are often sparse, hence for this thesis the Band function (Chapter 1 Formula) is used to provide the spectral shape for the GRB emission required to determine the k-correction.

At low energies this function provides a power law continuum with an exponential cut-off that provides the spectral shape in Figure 3.5 where $\alpha = \text{photon index} - 1$. At higher energies where the $\beta - 1 = \text{photon index}$ the Band function produces a broken power law that is used to describe the spectral shape.

3.2.2 Interpolating the data

Some GRB light curves have only around ten data points, whereas others have hundreds. To examine the data at given times, this left one of two alternatives: the first to focus on a single part of the light curve, for example that detected in the BAT (15-150 keV) and to fit this data, then extrapolate⁴ to other parts of the spectrum. The second option was to use interpolation to estimate what is happening between each data point.

The extrapolation method has the advantage that by looking at a single part of the light curve it will be able to follow the light curve out to further energies than interpolation, which will be unreliable past the last data point as it will continue at the previous gradient. The problem with this method is that the GRB light curve changes as it evolves, so looking at one smaller part would probably not

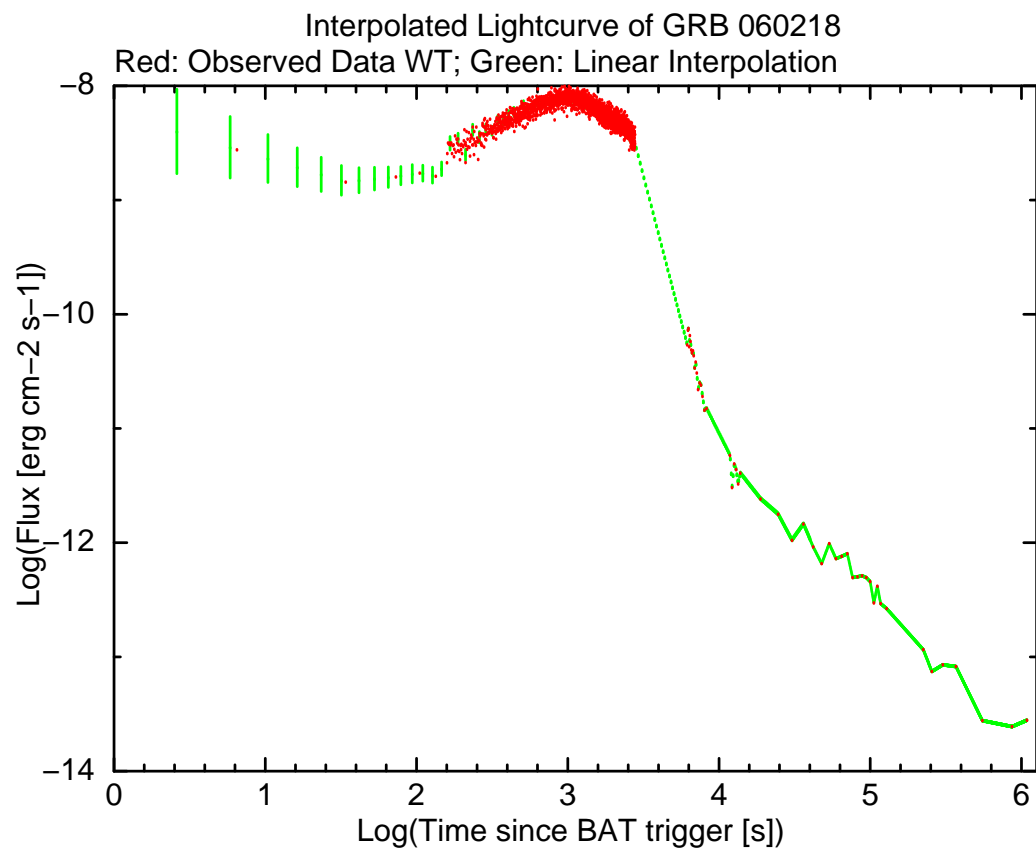
⁴Extrapolation creates new points outside a discrete set of known data points as opposed to interpolation which creates new points between data points.

give an accurate fit out to later energies as the function of the light curve will probably have changed considerably. Also it has been found that the results from extrapolation are often less meaningful and subject to greater uncertainty (Katz 2005).

The interpolation method has the advantage that it uses every data point available to estimate the light curve, using this method flares and other features will be included in the complete light curve. Thus interpolation is the method used for this chapter, there are three types of interpolation that are commonly used: linear, polynomial and spline interpolation. Polynomial interpolation suffers from Runge's phenomenon⁵, so was eliminated as a method.

⁵Runge's Phenomenon occurs when high order polynomials are chosen by the interpolation routine that then cause unnecessary oscillations between data points.

Figure 3.6: The light curve of GRB 060218 and the linear interpolation between each datapoint. The original data points in red and in green the linear interpolation and the error on each interpolated point.



The spline interpolation fails to fit the data convincingly, usually linear interpolation would have straight lines of changing gradients between points. However the interpolation has been performed on a logarithmic scale, so when you move back to normal space this becomes a curve giving a smooth transition between data points. Linear interpolation managed to fit reliably all of the light curves in the sample from the beginning to the end of the data as shown in Figure 3.6, thus this method was used to measure the flux at given times for each light curve.

3.2.3 Pulse fitting flares

Willingale *et al.* (2010) uses an analytical expression for pulse profiles derived from the internal shock model incorporating the spectrum and decay indices from fast cooling regime and a tail arising from high latitude emission. Each pulse is assumed to originate from an expanding thin shell ejected from the central engine using the emission profile given in Genet & Granot (2009).

The Lorentz factor is assumed to be constant, if fast cooling applies to the luminosity for sychrotron emission $d = -1$ and $a = 1$. The comoving luminosity is then integrated over the equal arrival time surface (EATS) giving the number of photons N per unit photon energy E , area A over observed time T as

$$\frac{dN}{dEdAdT}(E, T \geq T_{ej} + T_0) = P(T - T_{ej}, T_{rise})B\left(\frac{E}{E_f} \times \frac{T - T_{ej}}{T_f}\right) \quad (3.1)$$

where B is the magnetic field strength and the pulse profile (P) is

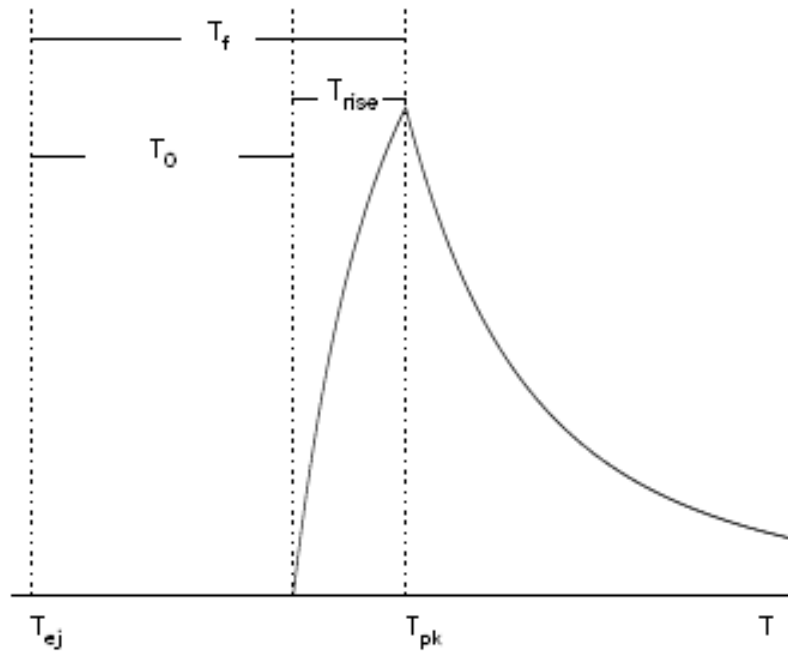


Figure 3.7: A schematic diagram showing important parameters for the pulse fitting model, where the pulse rises over time T_{rise} until it reaches a peak T_{pk} . The characteristic times of the pulse T_f and $T_0 = T_f - T_{rise}$ are the arrival times of the last photon and the first photon emitted from the shell, along the line of sight measured with respect to the ejection time T_{ej}

$$P(T - T_{ej}, T_f, T_{rise}) = \left[\left(\min\left(\frac{T - T_{ej}}{T_f}, 1\right)^{\alpha+2} - \left(\frac{T_f - T_{rise}}{T_f}\right)^{\alpha+2} \right) \times \right. \\ \left. \left(1 - \left(\frac{T_f - T_{rise}}{T_f}\right)^{\alpha+2} \right)^{-1} \right] \left(\frac{T_f - T_{rise}}{T_f}\right)^{-1} \quad (3.2)$$

Where E_f is the characteristic energy of the pulse at time T_f , d is the index at the peak frequency of the $\nu F\nu$ spectrum and a is the temporal index. This spectral profile governed by index d and the pulse profile function gives the rise and fall of the pulse as shown in Figure 3.7.

3.2.4 Analysis

A sample of 130 GRBs were downloaded, but 9 of these were not able to be processed due to there not being enough information about the burst to provide the inputs required to calculate the k-corrections. Another problem encountered was where the k-corrections were not given as a number, this in cases where no peak energy was detected and where the true peak energy was substantially less than the assumed value of 116 keV. To resolve this problem β for the XRT was set to equal α and α was set to the previous value for β in the XRT.

To investigate the integrated flux of the GRBs a program was written to find the area under the interpolated data. This program used the Trapezium Rule to create a reasonable estimate for the area shown in Figure 3.8.

The GRB's T_{90} was used as an input for the integration program that gives the time integrated flux as an output, which was then used to calculate the isotropic energy E_{iso} of each GRB using Formula 1.3 (Chapter 1, Section 1.2.1). The flux

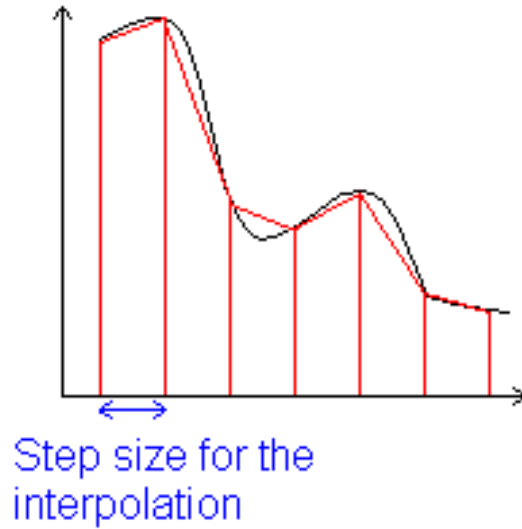


Figure 3.8: A simplified diagram of how the program uses a series of trapeziums to estimate the area under the light curve of each GRB. Since the step size of the interpolation program is very small this was taken to be the width of the trapezium.

was then used to find the luminosity of each GRB within the sample to examine how it changes with time in the observed frame and the rest frame, the relationship between the luminosity and E_{iso} was also explored.

In Figures 3.9 to 3.14 the results from plotting the luminosity against the isotropic energy are shown at different time intervals. A line of best fit was used to investigate how the scatter in luminosity at 1σ from the line of best fit varies at each time interval. The scatter was calculated by using Formula 3.3 where y_{obs} is the luminosity in ergs s^{-1} at a given time step, x_{obs} is the E_{iso} in ergs, m is the gradient of the line of best fit, c is the intercept and N is the number of GRBs with a luminosity at a given time step.

$$\text{Scatter} = \left[\frac{\sum (y_{\text{obs}}^2 - (mx_{\text{obs}} + c)^2)}{N} \right]^{\frac{-1}{2}} \quad (3.3)$$

At $10^3 - 10^4$ seconds the scatter is at its greatest ~ 5.1 dex compared at 10 (scatter ~ 0.1 dex), 10^5 and 10^6 seconds when the scatter drops to ~ 2.5 . O'Brien *et al.* (2006) found that after ~ 10 seconds the decay from a GRB follows two paths; either a steep decay in which the flux can fall by a factor of 3 or more gradual decay. These two possible paths are shown in Figure 1.6 in Chapter 1, Section 1.1.4 where the difference in flux between these two paths begins just before 100 seconds which agrees with my results where the scatter increases to 1.94 dex. Figure 1.6 also shows the difference between these paths reducing between $10^4 - 10^5$ seconds, as is seen in my results where the scatter drops at 10^5 seconds.

In Figure 1.6 the time where there is the greatest spread in GRB luminosities is between 100 and 1,000 seconds, this is plotted with light curve shape in Figure 3.15, to examine if GRBs with certain shapes are grouped together.

In the observer frame Evans *et al.* (2009) finds there is a significant chance of a break from $\sim 100 - 10^5$ seconds, but that there are two peaks one from $\sim 1 - 300$ seconds and at $\sim 10^4$ seconds, which they suggest reflect common start and end times of the plateau phase. Again, this is consistent with the scatter seen in Figures 3.9 to 3.14 in the rest frame.

Figure 3.9: The relationship between the luminosity of a GRB (ergs s^{-1}) and its isotropic energy (ergs) in the rest frame 10 seconds after the initial burst, for which the scatter in luminosity is 0.12 dex.

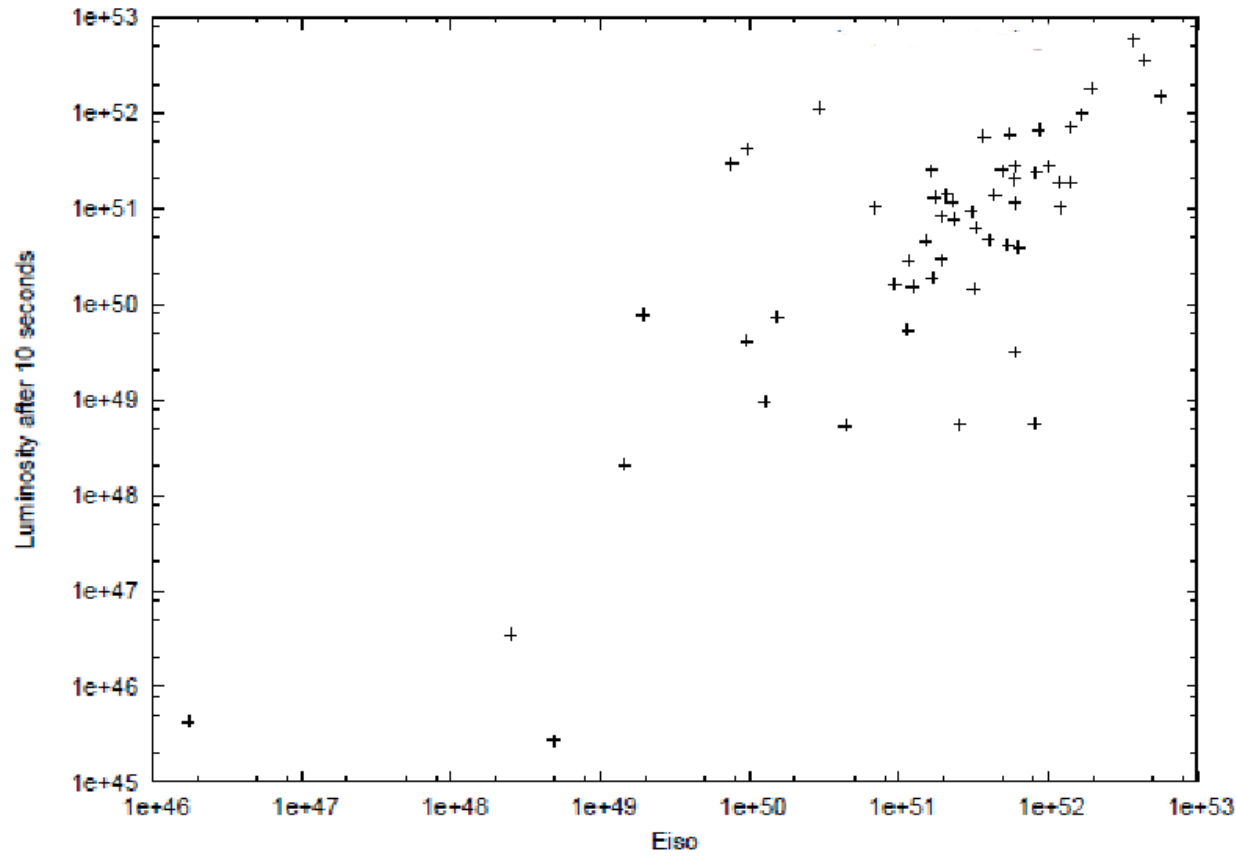


Figure 3.10: The relationship between the luminosity of a GRB (ergs s^{-1}) and its isotropic energy (ergs) in the rest frame 100 seconds after the initial burst, for which the scatter in luminosity is 1.94 dex.

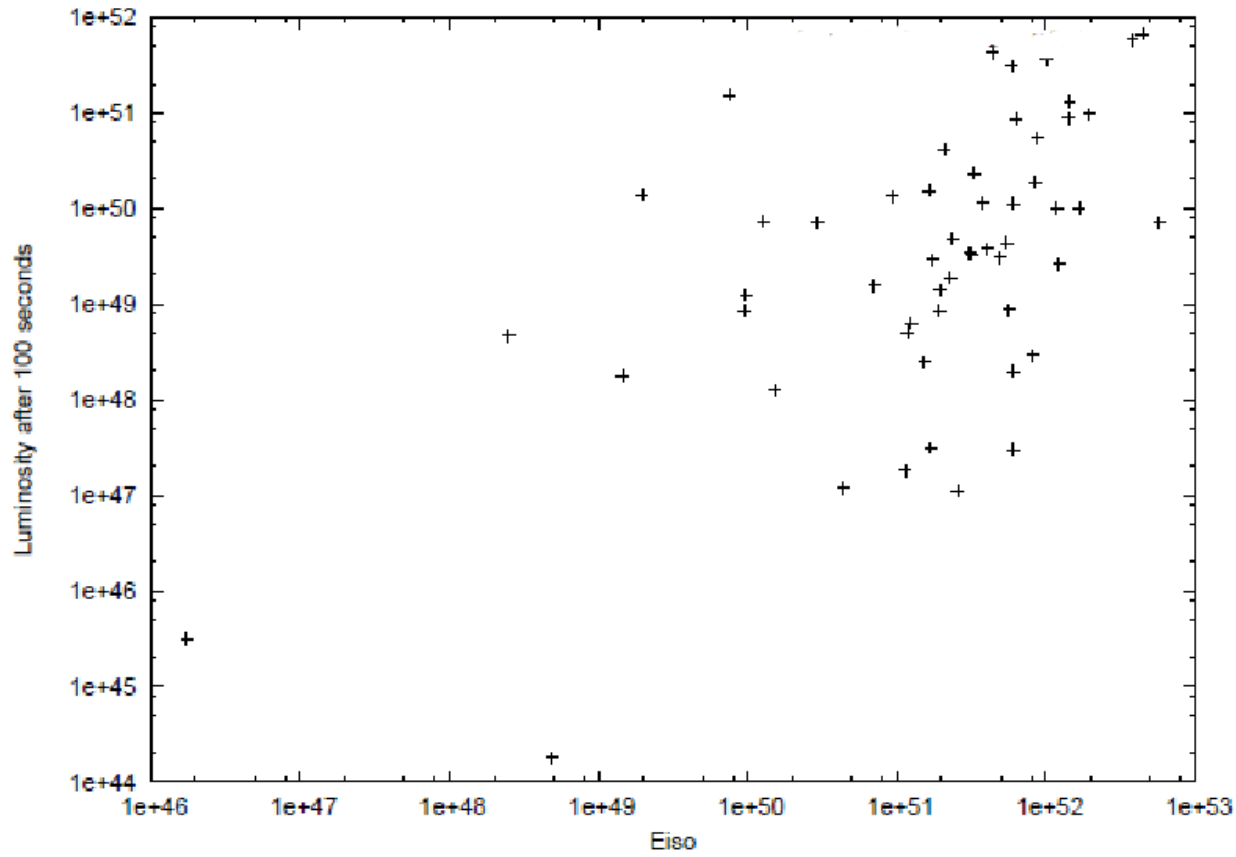


Figure 3.11: The relationship between the luminosity of a GRB (ergs s^{-1}) and its isotropic energy (ergs) in the rest frame 10^3 seconds after the initial burst, for which the scatter in luminosity is 5.06 dex.

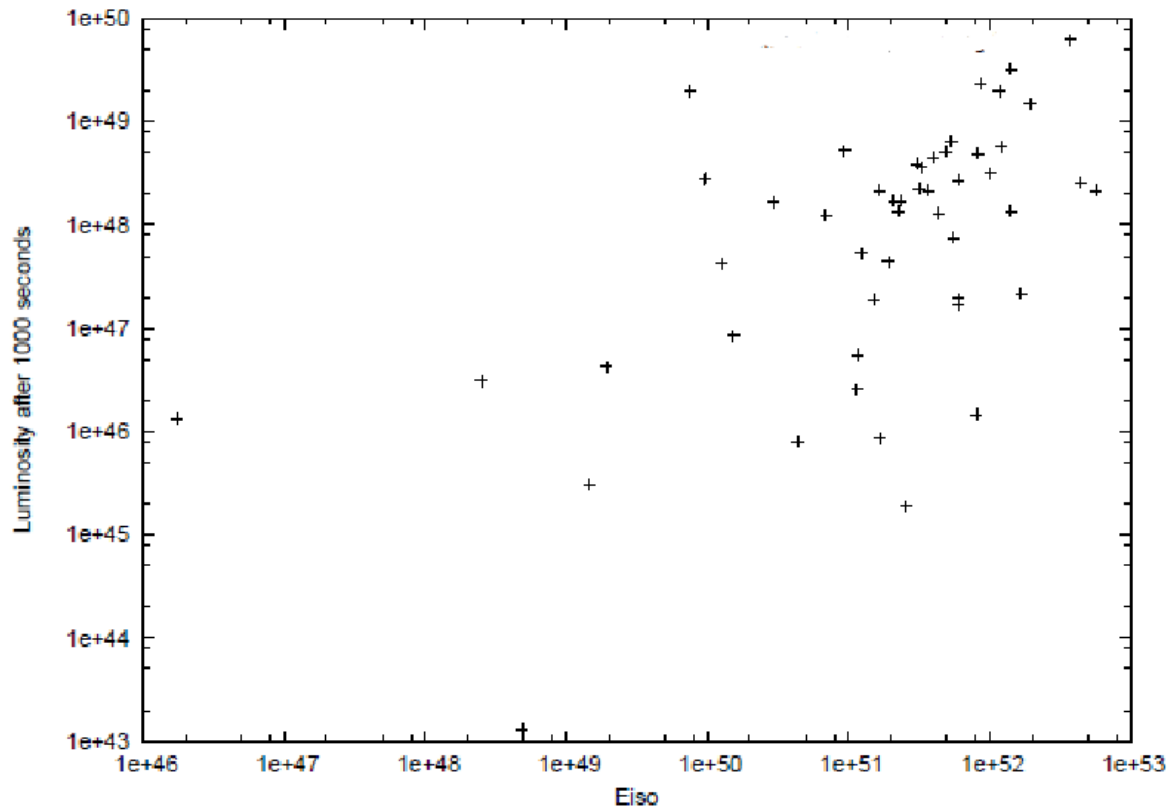


Figure 3.12: The relationship between the luminosity of a GRB (ergs s^{-1}) and its isotropic energy (ergs) in the rest frame 10^4 seconds after the initial burst, for which the scatter in luminosity is 5.16 dex.

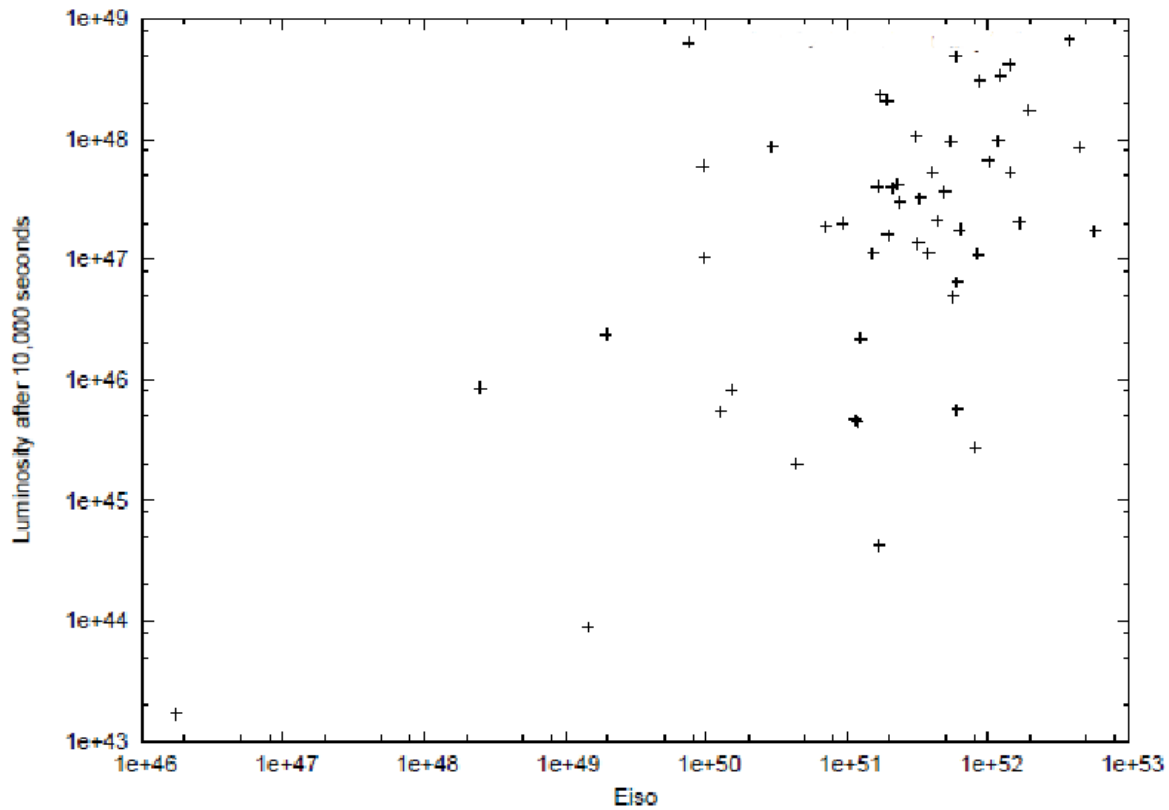


Figure 3.13: The relationship between the luminosity of a GRB (ergs s^{-1}) and its isotropic energy (ergs) in the rest frame 10^5 seconds after the initial burst, for which the scatter in luminosity is 2.54 dex.

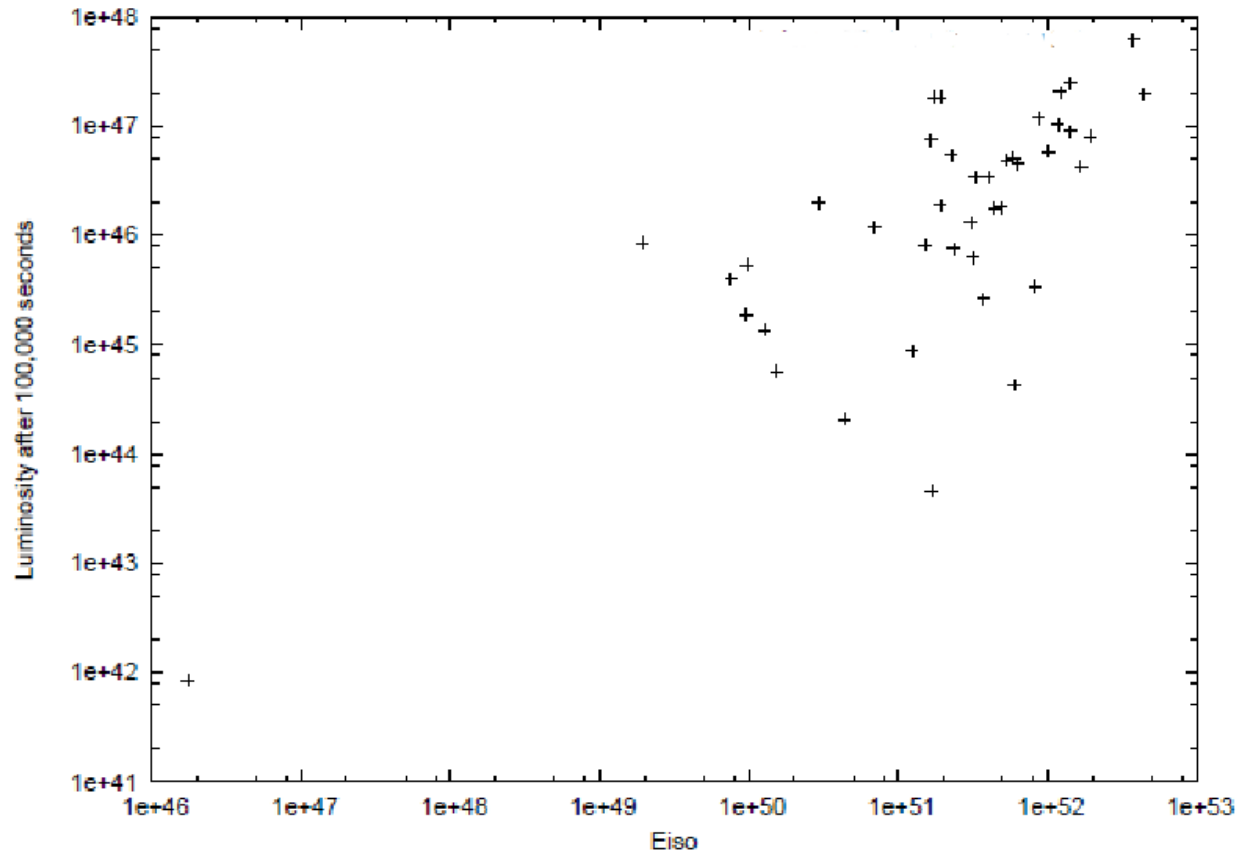
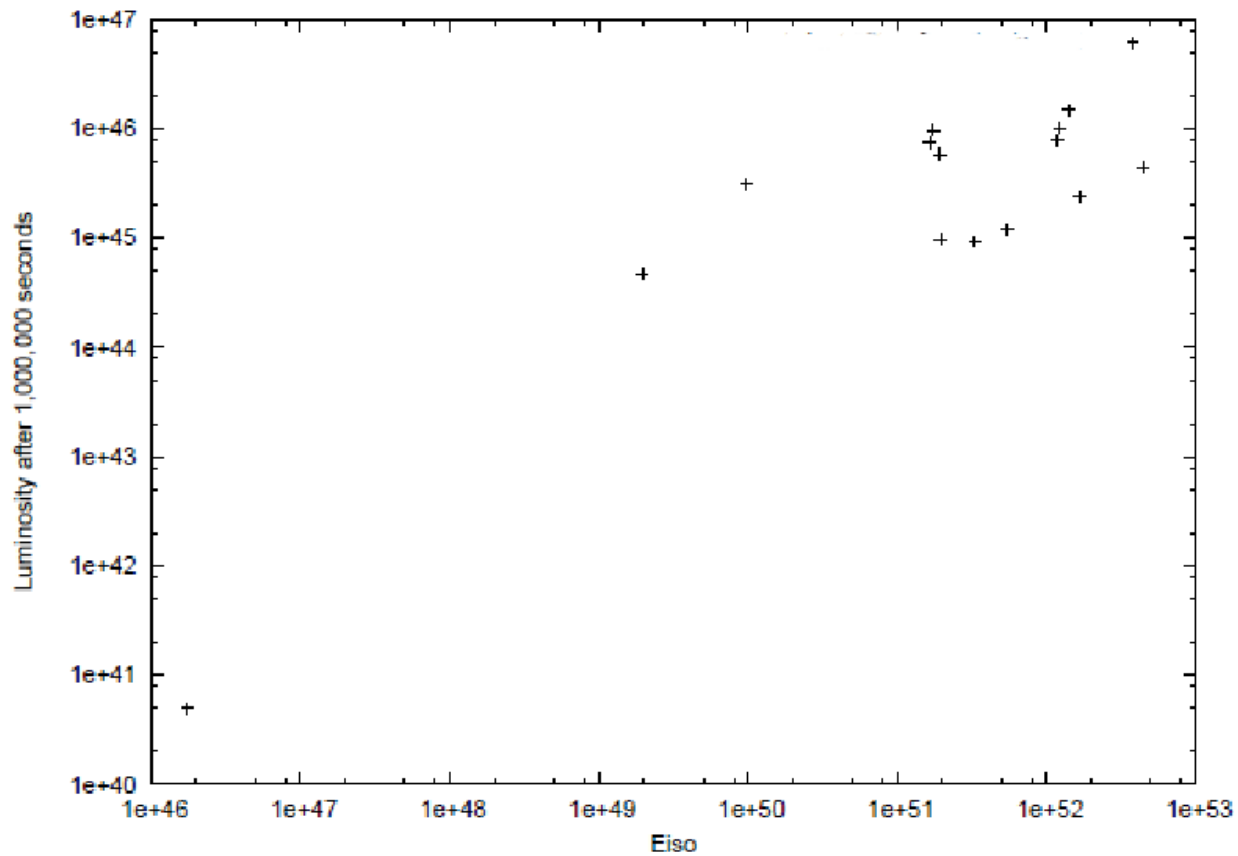
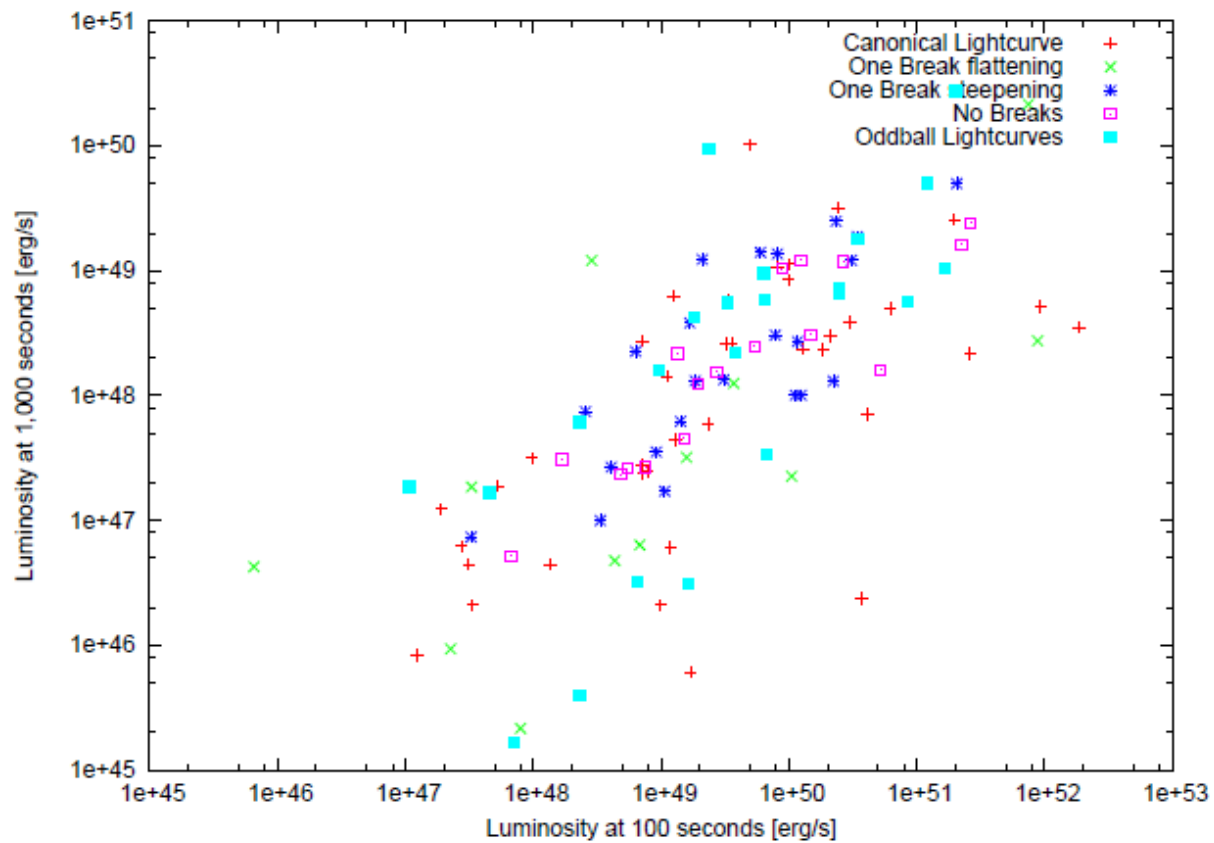


Figure 3.14: The relationship between the luminosity of a GRB (ergs s^{-1}) and its isotropic energy (ergs) in the rest frame 10^6 seconds after the initial burst, for which the scatter in luminosity is 0.32 dex.



The outliers in Figures 3.9 to 3.14 are GRB 050803, GRB 060218 and GRB 060502B. GRB 050803 had a relatively low flux (1.48×10^{-10} at 10 seconds), which helped give a relatively low value for the isotropic energy at early times. GRB 060218 was an unusual burst in that as well as the usual non-thermal X-ray spectrum, there was also a thermal component thought to be the break out of a shock driven by a mildly relativistic shell into the dense wind surrounding the progenitor (Campana *et al.* 2006). Also the peak flux of GRB 060218 was an order of magnitude lower than any other GRB-SNe except XRT 020903 which had an even softer spectrum (Sakamoto *et al.* 2004). Finally it is also a relatively low redshift burst and a short burst which tend to have lower isotropic energies (but not low enough to separate them from the lower energy long GRBs).

Figure 3.15: The luminosity of each GRB at 100 and 1,000 seconds, when there should be a larger separation in luminosity due to spectral shape O'Brien *et al.* (2006). The GRBs are displayed colour-coded by their light curve shape.



In Figure 3.15 the luminosity at 100 and 1,000 seconds is plotted, no group of GRB light curve shapes clearly stand out as being separate from other GRBs. Overall it can be seen that each group of GRBs have dropped by one magnitude between 100 and 1,000 seconds. The oddball light curve luminosities do not seem to be that unusual compared to other GRBs. One break flattening light curve have more variation in luminosity than one break steepening GRBs, this is unsurprising as the former would have already undergone a steeper decline so any variation in α or time the light curve flattens would lead to a larger spread in luminosity. The group of GRBs with the tightest correlation are those with no breaks and a gradual decline which is not unexpected, however I would have expected canonical GRBs with a sharp decline at this time to have lower luminosity.

In Figures 3.16 to 3.19 a light curve of each shape GRB has been plotted at different redshifts to compare the efficiency. The efficiency η of GRBs is interesting because it could give us further insight into the energy dissipation process. Efficiency of a given GRB is given in Formula 3.4 where E_γ and E_K are the isotropic gamma-ray energy and the kinetic energy of the afterglow respectively.

$$\eta = \frac{E_\gamma}{(E_\gamma + E_K)} \quad (3.4)$$

The difficulty with finding the efficiency is that although E_γ can be measured from the gamma-ray fluence for bursts with known redshift, the measurement of E_K requires detailed afterglow modelling. The shallow decay phase in the canonical light curve (Chapter 1 Section 1.1.4) is the most relevant in terms of refreshed shocks are the origin of this phase then the initial afterglow energy must be lower than estimated using late time data, leading η to be underestimated.

For GRBs with a very shallow flux decay lasting from $\sim 10^{2.5}$ to $\sim 10^4$ seconds, the decay implies in a model independent manner, a very large efficiency, typically $\geq 90\%$ (Eichler & Granot 2006). Thus about 90% of energy goes into gamma-ray radiation and about 10% goes into the blast wave. It could be expected that the afterglows which don't break to be more luminous than GRBs with a canonical shape until late times ($\sim 10^5$ seconds). In Figure 3.16 to 3.19 GRBs have been selected as close as possible to each redshift step (maximum scatter in redshifts is 0.15) and in three panels the luminosity of the canonical light curves becomes \geq that of the light curves with no breaks as expected. This result is consistent with Shao *et al.* (2010) that interprets the lower luminosity light curve of no break afterglows as disfavoured energy injection. However this interpretation disagrees with Evans *et al.* (2009) where the relationship between the spectral and temporal indices of GRBs are plotted with a dark grey band representing the areas permitted by afterglow closure relationships. A significant fraction of the no break light curves are above this band implying energy injection.

Early in the light curve in three out of four of the panels it is \leq the canonical luminosity. Oddball light curves and GRBs with one break where the decay then flattens seem to be relatively luminous at early times, but this is hard to tell due to the small number of light curves present.

Figure 3.16: The complete lightcurve of a GRB chosen from each light curve morphology with redshift closest to $z = 1$. Each GRB light curve is then colour-coded by shape

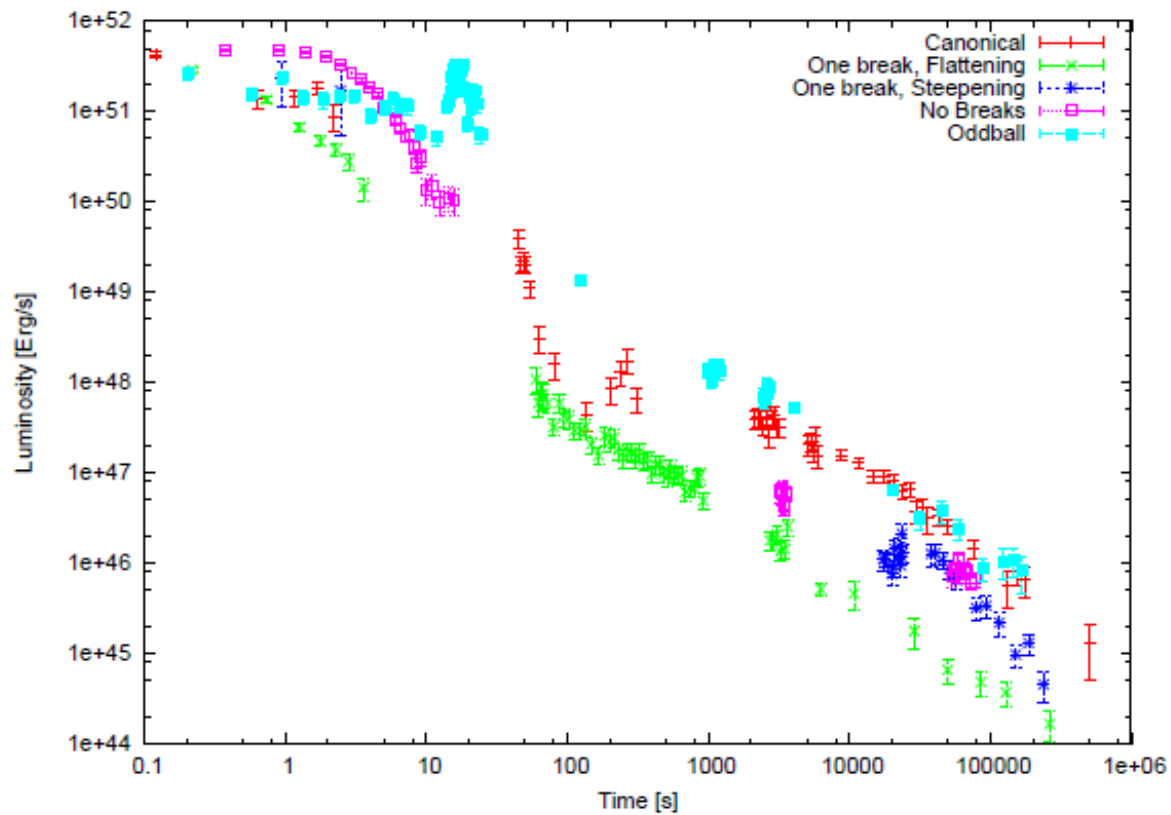


Figure 3.17: The complete lightcurve of a GRB chosen from each light curve morphology with redshift closest to $z = 2$. Each GRB light curve is then colour-coded by shape

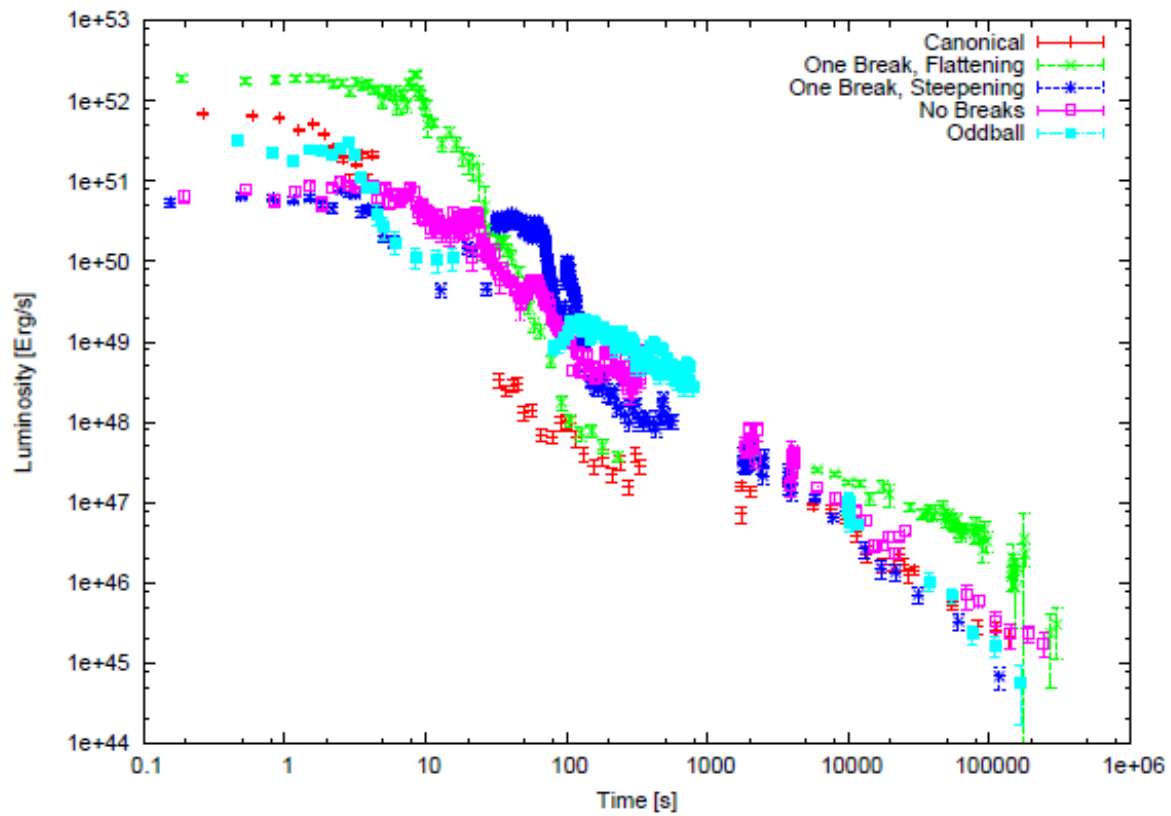


Figure 3.18: The complete lightcurve of a GRB chosen from each light curve morphology with redshift closest to $z = 3$. Each GRB light curve is then colour-coded by shape

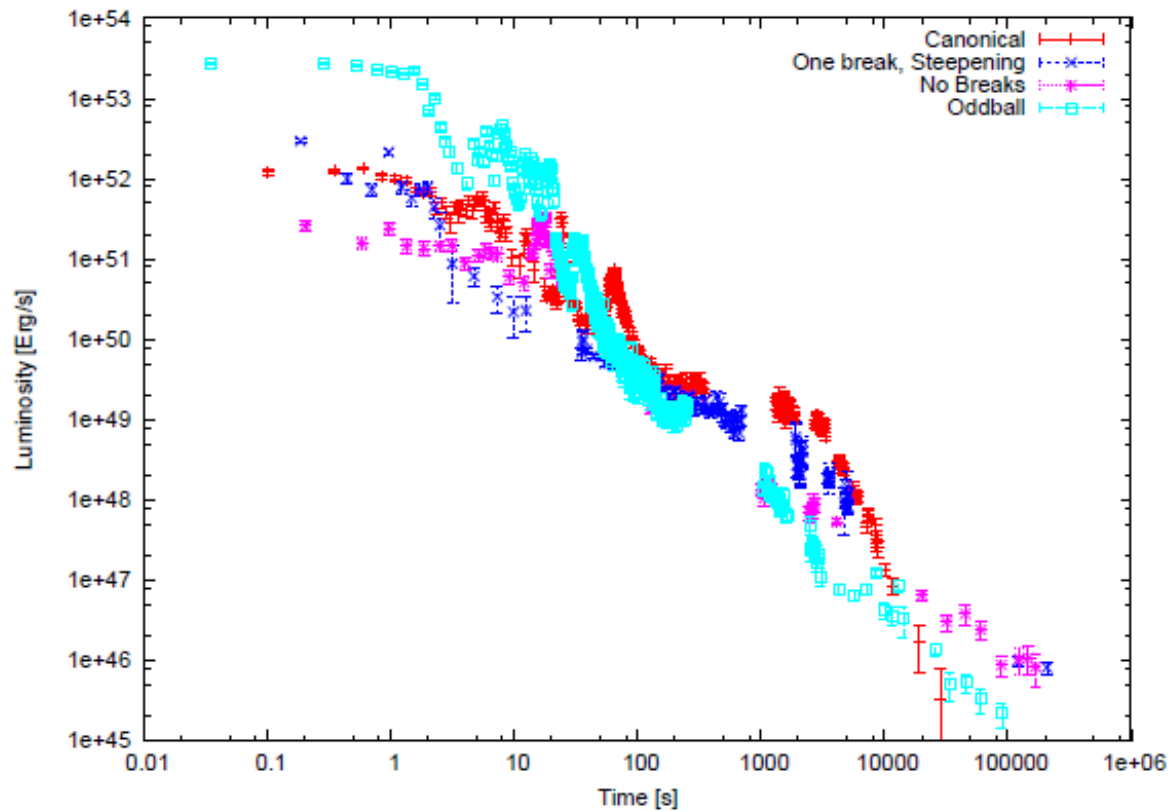
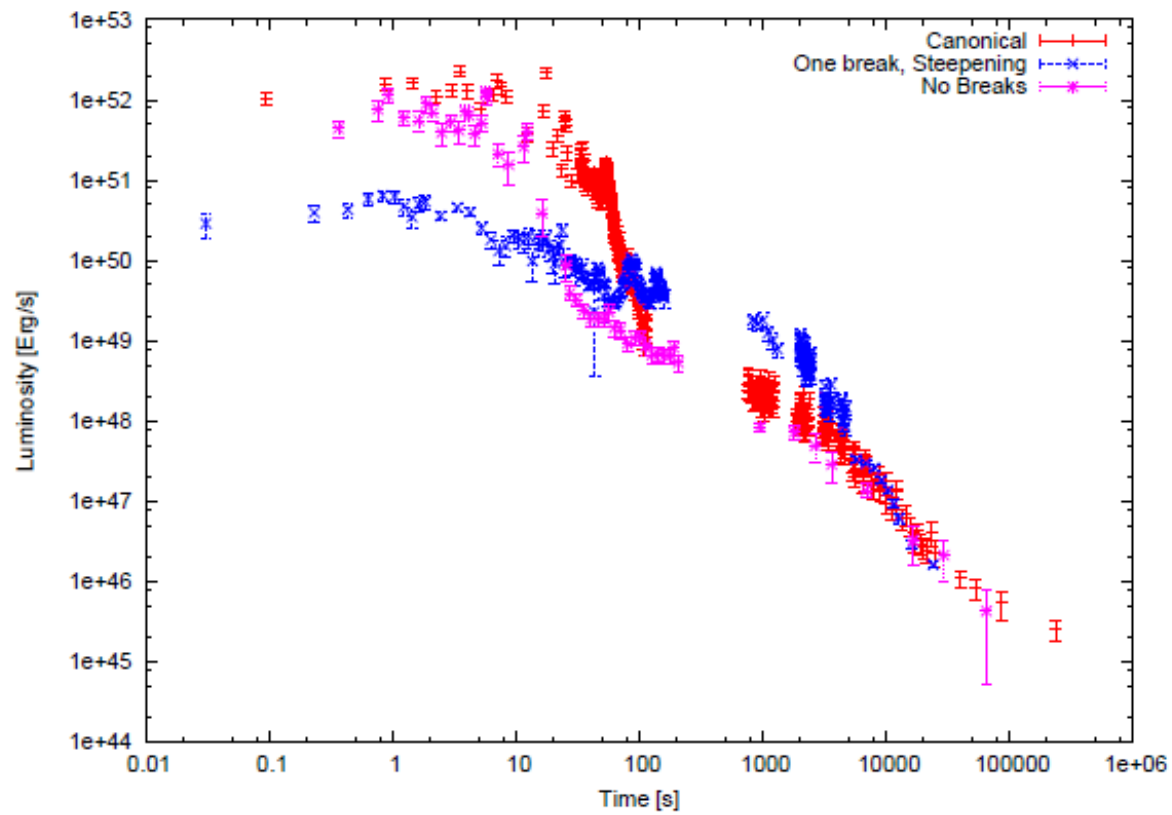


Figure 3.19: The complete lightcurve of a GRB chosen from each light curve morphology with redshift closest to $z = 4$. Each GRB light curve is then colour-coded by shape

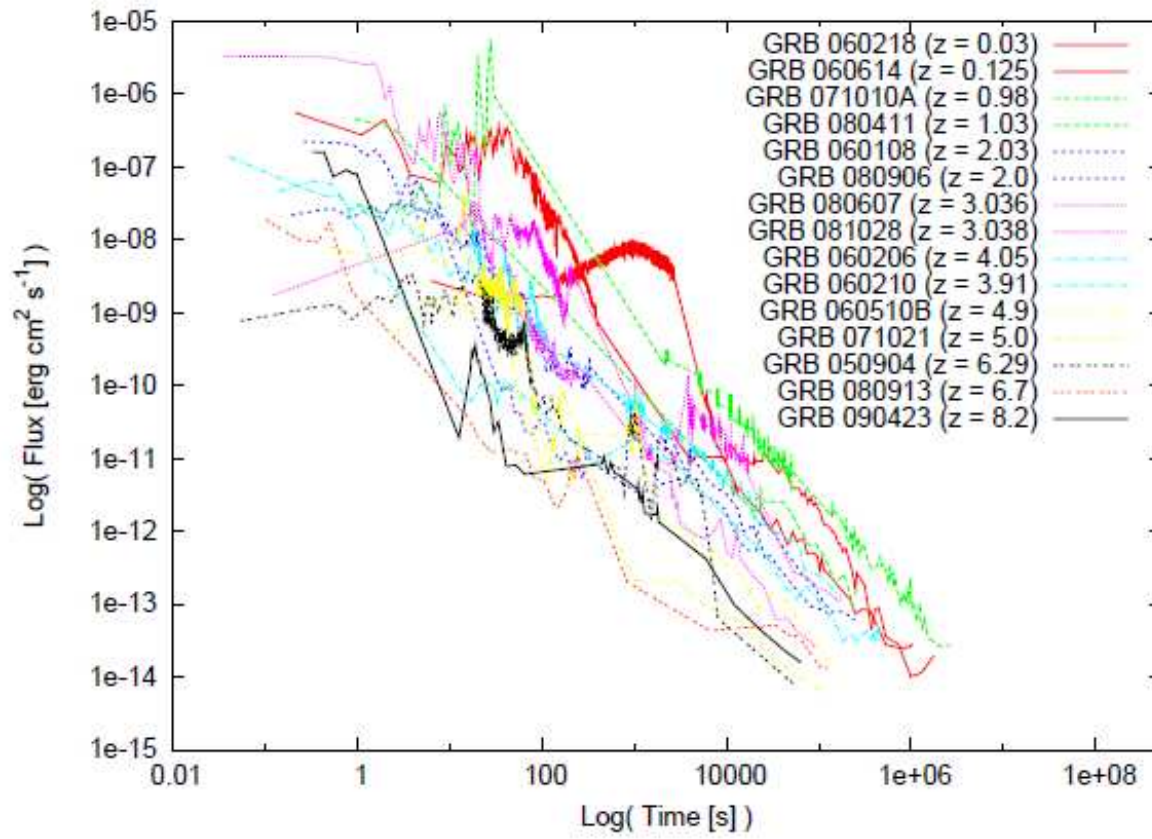


Although the star formation rate for Population III stars is expected to peak at $16 \leq z \leq 20$ (Valageas & Silk 1999), Campana *et al.* (2001) states that if a GRB was observed at very high redshift ($z \geq 6$) with no intrinsic absorption (and free of intervening systems) it will be a good candidate for having been produced by a Population III star. Good GRB candidates would be expected to be high energy up to $\sim 10^{57}$ erg and long-lived with a rest time duration $\sim 10^4$ seconds (Toma, Sakamoto & Mészáros 2011).

The sample of *Swift* GRBs with redshift contains three GRBs with $z \geq 6$, in Figure 3.20 the rest frame⁶ light curves of 15 GRBs with increasing redshifts are plotted to investigate if there are any significant differences between high redshift and low redshift GRBs. In Figure 3.20 no defining feature of difference can be seen in the light curve as the GRB redshift increases.

⁶The time was corrected into a rest frame time by using $t_R = t_{OBS}/(z + 1)$ where t_R is the time in the rest frame and t_{OBS} is the time in the observed frame.

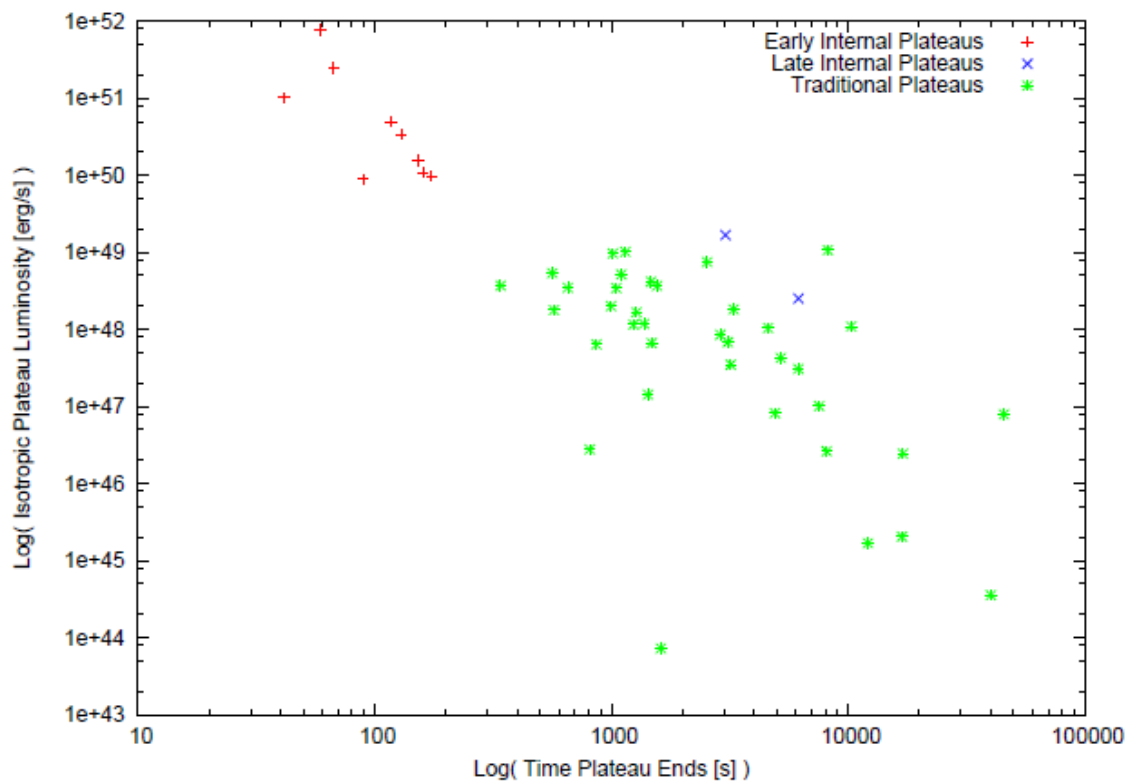
Figure 3.20: The light curves of two GRBs plotted in the rest frame at each redshift step.



3.2.5 GRBs with plateaus

During Chapter 2 GRBs with internal plateaus were used to find information about the central engine powering the burst, in the sample of GRBs used in this chapter, 37 have light curve with a traditional plateau (see Chapter 1, Section 1.14, Figure 1.6). The luminosity of this plateau and time it ends (shown in Figure 3.12) were used as inputs for Formulae 2.2 and 2.3 (Chapter 2 Section 2.4). Figure 3.22 shows the rotational period and magnetic field strength found from these formulae.

Figure 3.21: The variation in luminosity and end time of the plateau for GRBs with traditional plateaus and GRBs with internal plateaus. Early internal plateaus are shown in red, blue shows late internal plateaus and traditional plateaus are green.

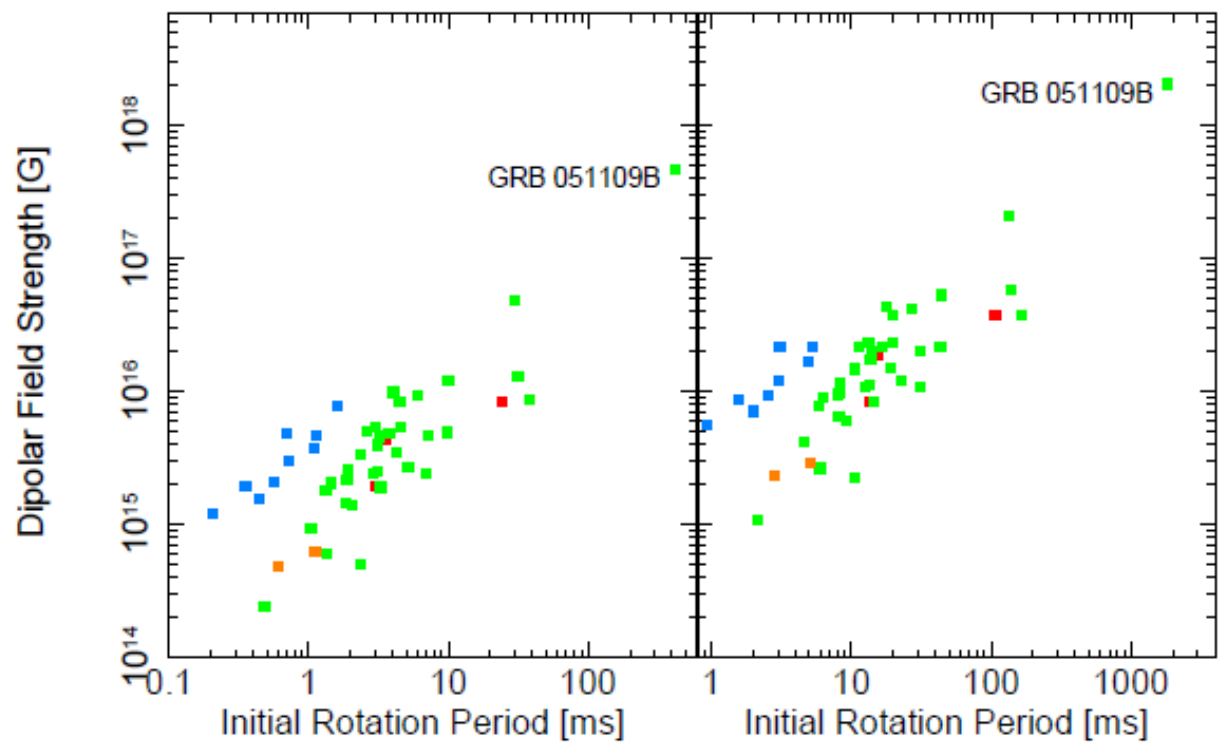


The early internal plateaus clearly stand out in Figure 3.21 as separate from the traditional plateaus, even the late internal plateaus which end on a similar timescale to traditional plateaus have a more extreme luminosity than most traditional plateaus. It is also interesting in Figure 3.21 that the traditional plateaus seem to follow on from the internal plateaus albeit with more scatter. The relationship between the luminosity and break time of traditional plateaus has been examined as a possible tool for constraining cosmological parameters by extending the Hubble diagram⁷ to very high redshifts (Cardone *et al.* 2010, Dainotti *et al.* 2008 & Dainotti *et al.* 2010). The Willingale *et al.* (2007) model (discussed in Chapter 2, Section 2.2) enables all *Swift* GRBs to be fit by the same expression, which gives the break time of the plateau as one of its parameters, this gives an advantage to using this relation to constrain cosmological parameters. In Cardone *et al.* (2010) it is stated that more high luminosity GRBs are needed to help determine between current models, the early internal plateaus sit at a higher luminosity in Figure 3.21 and appear to follow the same relation as traditional plateaus.

The central engines that produce early internal plateaus in the light curve have higher magnetic fields for a given rotational period than those that could produce shallow plateaus. The defined gap between these objects and the other plateaus implies that central engines that produce internal plateaus as different and more extreme objects than central engines that produce other plateaus. The gap in the bottom right of Figure 3.22 seems to support the idea presented in Chapter 2, Section 2.4 that it could be other plateaus are being hidden beneath the afterglow emission.

⁷A diagram that allows the cosmological parameters such as the Hubble Time to be found

Figure 3.22: The relationship between period and magnetic field found for GRBs with an internal plateau compared to those with a traditional plateau. Early internal plateaus are shown in blue, orange shows late internal plateaus, traditional plateaus are green and red shows traditional plateaus which also have an internal plateau in their light curve



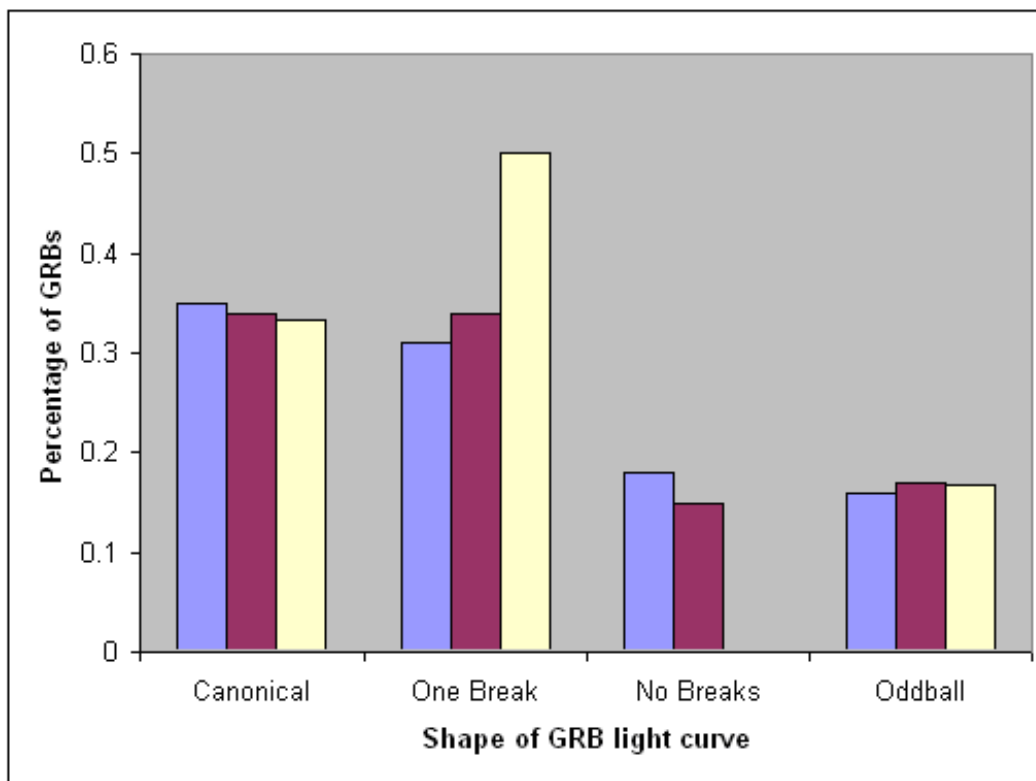
For GRBs that produce late internal plateaus perhaps it is not surprising that they would be similar to the traditional plateaus as mentioned previously both types of plateau end on a similar timescale. However if the traditional plateaus were due to the collapse of a spinning magnetar, where are they gaining the energy to support their shallow decay? Also if this is true and the steep decline in internal plateaus is due to the magnetar becoming unstable and collapsing to a black hole, how can it then produce a traditional plateau?

3.2.6 Light curves of GRBs with flares

The GRB light curves used in this chapter were scrutinized for flares, to ensure that variations in the light curve were not wrongly included I have assumed that a flare must have a flux at least three times greater than the underlying afterglow. Using this criteria 86 flares were found in 53 GRB light curves.

GRB afterglows with no breaks (Section 3.1.1 Figure 1.3) are likely to be dominated by the afterglow component (See Chapter 2 Section 2.2) from the beginning of *Swift* observations (Liang *et al.* 2009), thus I'd expect that these GRBs would show a limited flaring component. The fraction of GRB light curves with each light curve shape and flares are examined in Figure 3.23. The standard flares seem to have a similar percentage population as all GRBs with redshift, though mainly canonical and light curves with one break show flares and the group with the least flares are light curves with no breaks. The giant flares do not follow the same behaviour they are more common in light curves with a single break.

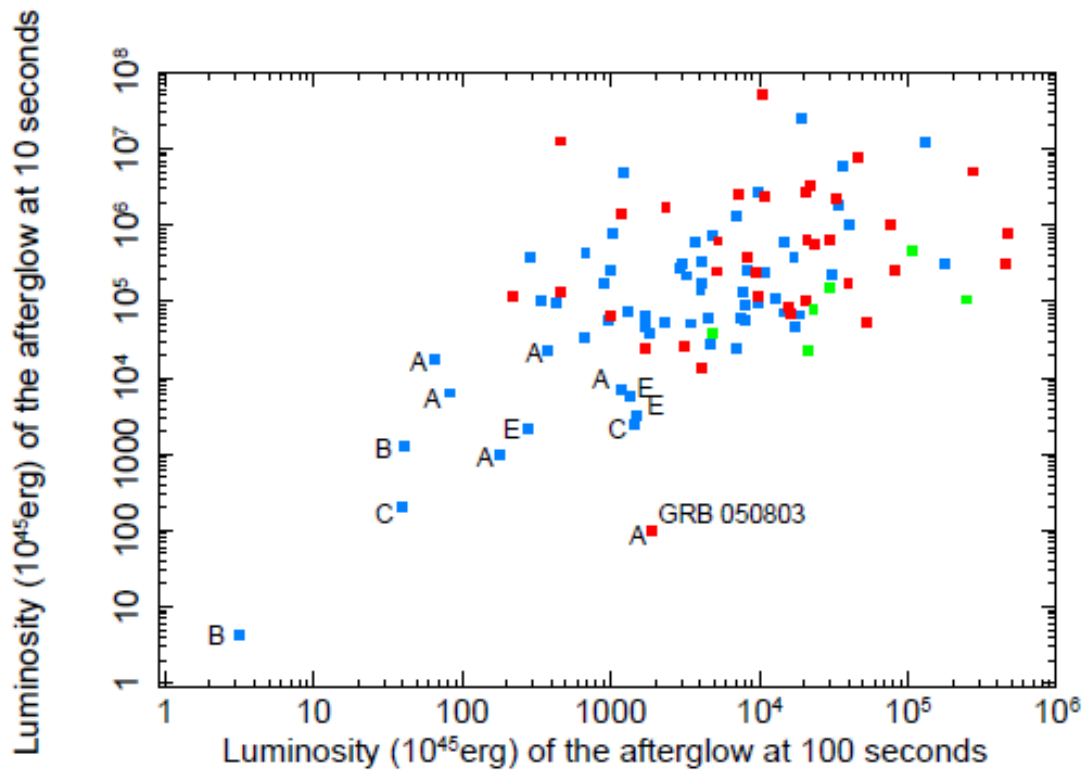
Figure 3.23: The population of each light curve shape for all GRBs with redshift and no flares (blue), for all GRBs with redshift and normal flares (red) and GRBs with giant flares (beige) and measured redshift.



GRBs with normal flares have a very similar population to flareless GRBs with redshift, but with a slight favouring for one break afterglows. Margutti *et al.* (2010) finds that mainly canonical and light curves with one break contain flares, they investigated flare and afterglow morphology for all GRBs discussed in Evans *et al.* (2009) and 113 GRBs with flares from Chincarini *et al.* (2010). We also find that as a percentage the morphology of the underlying light curve is more important for giant flares which seems to favour one break light curves, however only a small number of GRBs afterglows satisfy the conditions used in Chapter 4 for giant flares meaning the error on this group is greater. Taking the result that giant flares are more likely to be found in one break afterglows, if this was due to the brightness of the afterglow then it implies that flares have an independent origin or it could mean that flaring emission is being suppressed instead of being hidden beneath other emission.

As flares need to be brighter than the underlying afterglow emission to be observed, upon initial inspection it would be expected flares would be prevalent in fainter afterglows. In Figure 3.24 the brightness and shape of GRB light curves that contain flares are plotted and surprisingly the afterglows that contain flares are amongst the brightest afterglows and the fainter GRB afterglows have no flares. However it should be noted that for giant flares the afterglows are slightly fainter than many GRBs.

Figure 3.24: The luminosity of afterglows with flares (red), giant flares (green) or without flares (blue). The letters represent different light curve morphologies where A, B, C, and E are canonical, one break flattening, one break steepening and oddball light curves respectively



The fainter afterglows (which do not contain flares) do not favour any particular shape although it is worth noting that the afterglows with no breaks are not part of this group. An unusually faint afterglow which contains a flare is GRB 050803 which was not mentioned in Section 3.3 as having a low flux at 10 seconds relative to other afterglows this changes at later times in Figure 3.8. Figure 3.24 seems to be suggesting that flares are not being hidden by the afterglow at early times, favouring that flaring emission is suppressed in fainter afterglows, but if so it is not clear how the flare is being produced in GRB 050803.

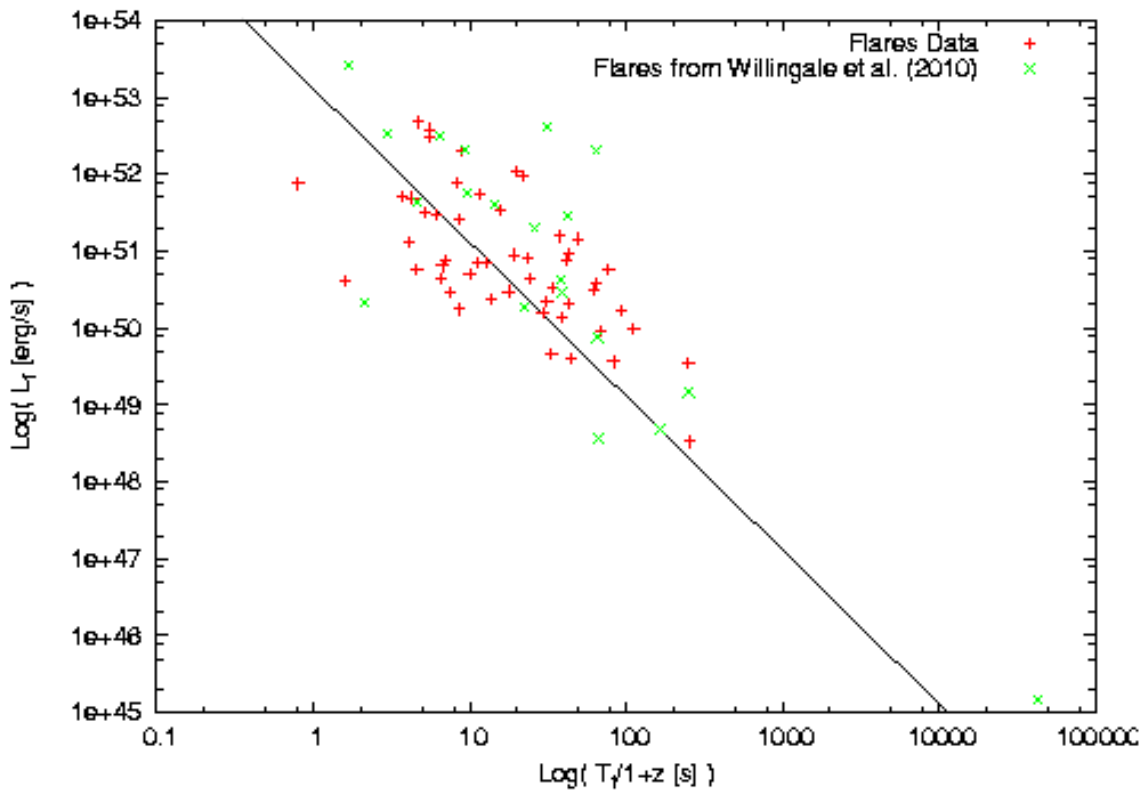
3.2.7 Flares

To investigate the flux density of individual pulses a program was produced (Willingale *et al.* 2010), this program also gives the characteristic time for 12 GRBs, however shown in Figure 3.25 there is a gap in the data from 200 to 1,000 seconds followed by a single pulse at 43,000 seconds. From the global sample of GRBs 34 had flares that could be fit reliably enough to provide the inputs needed for this model, thus this correlation is re-plotted for my sample to see if this can support the relation by filling in some of this gap.

Unfortunately no pulses were found past 300 seconds, although it does support the correlation found in Willingale *et al.* (2010). The latest T_f in Willingale *et al.* (2010) is GRB 050724 at $43,000_{-13,000}^{+15,000}$ seconds, this was classified as a short burst with extended tail emission. Interestingly this is the only short GRB in the Willingale *et al.* (2010) sample, for the GRBs fit in this chapter there is GRB 090423 which may be a short burst, but it is not certain (Krimm *et al.* 2009). GRB 090423 has a $T_f = 43.1$ seconds and a flare peak luminosity $L_f = 2.09 \times 10^{50}$ erg

s^{-1} , placing it amongst the relation with the long GRBs. It could be that GRBs with central engine activity this late are rare, so more GRB observations should fill in this gap. Alternatively that flares may occur in more luminous afterglows (as suggested in Section 3.3, Figure 3.23) and that after a few hundred seconds (in the rest frame) most flares are hidden by the afterglow. Excluding GRB 050724 as it is a short GRB with rapidly decaying afterglow.

Figure 3.25: The correlation between the flare peak luminosity and T_f found in Willingale *et al.* (2010), plotted with GRBs from this chapter.



The equivalent width of the flares in Figure 3.25 does not seem to correlate unless you assume the 5 GRBs on the right of the main population are a separate group. I have examined the T_{90} , flare luminosity, flare peak time, afterglow luminosity, redshift, UVOT magnitude, afterglow morphology and initial decay of the afterglow without discovering anything else that sets these GRBs apart.

Figure 3.26: The relation between the time the pulse peaks and the time between pulse ejection and the time the flare peaks; the equivalent width of flares.

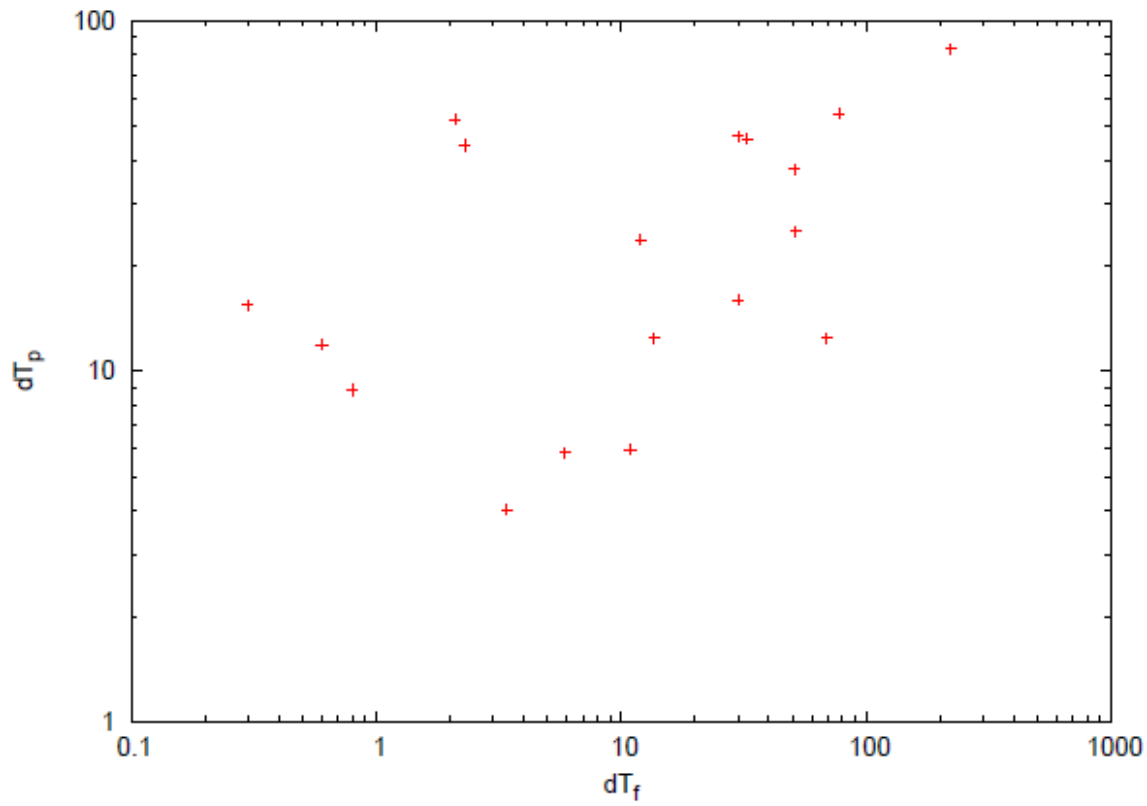


Figure 3.26-3.28 show the best relations found between the central object parameters and the parameters found for flares with the pulse fitting program. Other factors that did not correlate are flare luminosity, flare characteristic time, flare isotropic energy, initial rotation period of the central object, dipolar magnetic field, luminosity of the plateau and the time the plateau ends. For GRBs with a traditional plateau and an internal plateau, the plateau with the end time closest to the flare peak time was analysed. As flares are thought to be caused by central engine activity this seems surprising, maybe this suggests an unstable magnetar could not power traditional plateaus and that energy injection cannot explain the lack of the steep decline expected to be the signature of the magnetar collapsing to a black hole. So far there is only one GRB in Figure 3.28 with parameters taken from an internal plateaus so it is too early to draw any links between internal plateaus and flare behaviour.

Figure 3.27: The relation between flare energy and the magnetic field strength of the central object. The magnetic field strength was found using the end time of traditional and internal plateaus which are indicated separately.

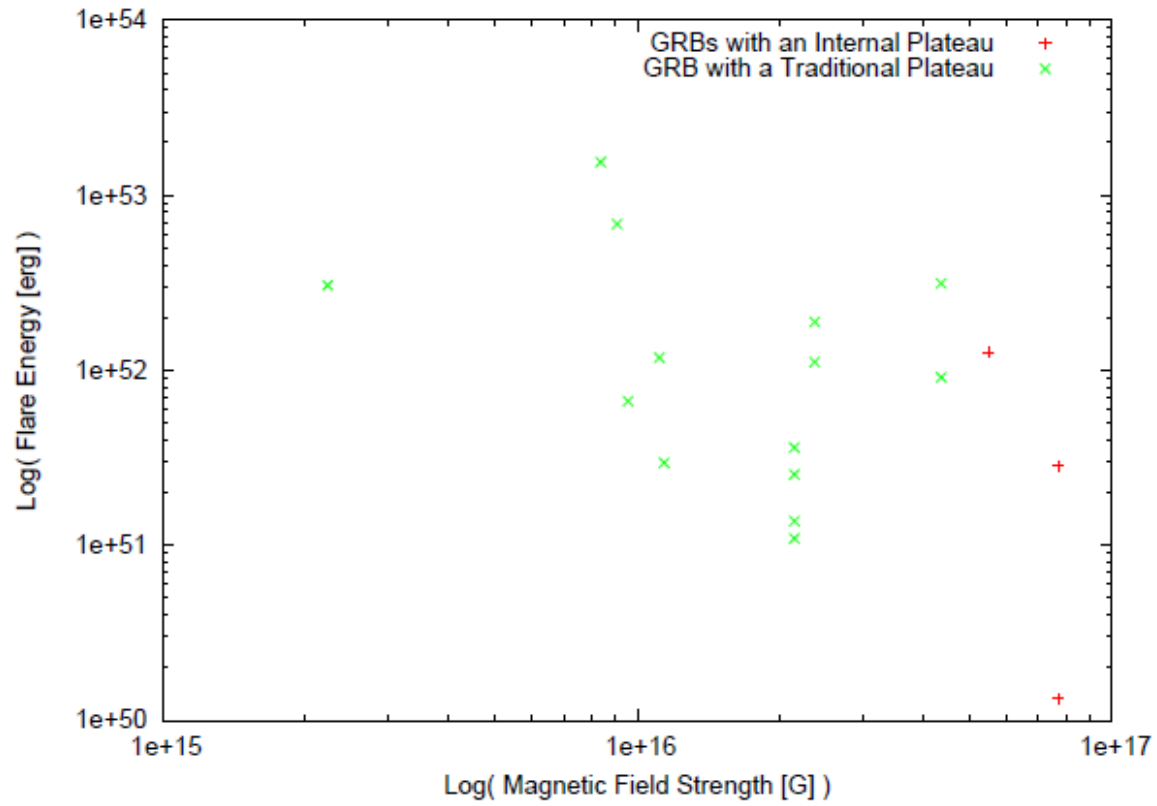
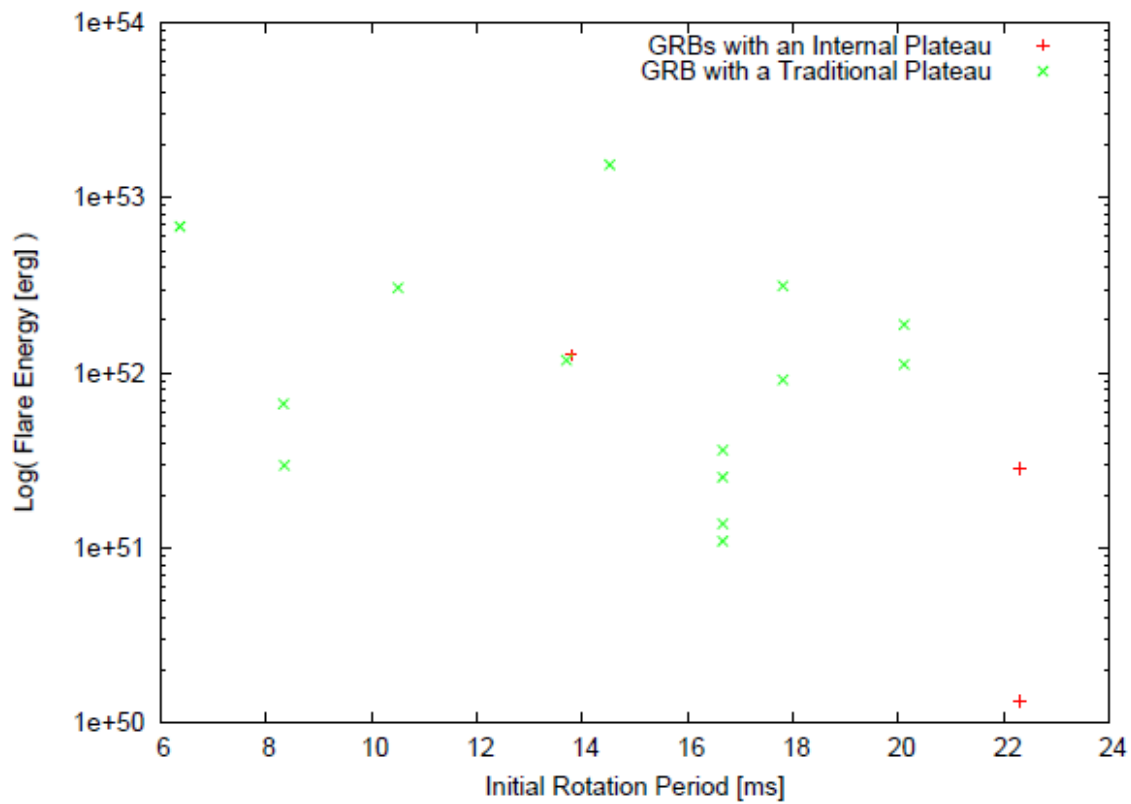


Figure 3.28: Flare energy plotted against the initial rotation of the central object. The central object's initial rotation was found using the end time of traditional and internal plateaus which are indicated separately.



3.3 Conclusions

This study finds there is more variability between the luminosity of different GRBs between 100 and 100,000 seconds, which supports the results from O'Brien *et al.* (2006). It is not clear why at late times the GRBs begin to converge.

No significant difference was observed between the light curves of GRBs at high redshift compared to those at lower redshifts, this could be because the largest recorded redshift is 8.2 (see Chapter Section 1.1.4), this is too low to be from Population III stars (see Figure 3.2). Thus the stars at redshift 8 may not be different enough in composition or other properties to produce an obvious difference to GRBs at closer redshifts, produced by other Population I or II stars.

GRBs with flares tend not to have faint afterglows at early times, for normal flares a similar percentage occur in each light curve shape as all GRBs with a redshift measurement suggesting they occur independently to light curve shape. Giant flares however seem to preferentially occur in light curves with one break. Additional GRBs did not fill in the gap between characteristic times in the $L_f T_f$ relation Willingale *et al.* (2010). We suggest that either the GRBs with central engine activity this late ($43,000^{+15,000}_{-13,000}$ seconds) are rare so more GRB observations should fill the gap or it could be that flares generally occur in more luminous afterglows (as suggested in Section 3.3.2, Figure 3.23) and after a few hundred seconds (in the rest frame) most flares are hidden by the afterglow.

The early internal plateaus clearly stand out in Figure 3.21 as separate from the traditional plateaus, even the late internal plateaus end on a similar timescale to traditional plateaus have a more extreme luminosity than most traditional plateaus. The central engines that produce early internal plateaus in the light curve have

higher magnetic fields for a given rotational period than those that could produce shallow plateaus. The defined gap between these objects in Figure 3.22 implies that central engines that produce central engines are different and more extreme than central engines that produce other plateaus.

For GRBs that produce late internal plateaus perhaps it is not surprising that they would be similar to traditional plateaus, as mentioned previously, both types of plateau end on a similar timescale. The gap in the bottom right of Figure 3.22 seems to support the idea presented in Chapter 2 Section 2.4 that it could be other plateaus are being hidden beneath the afterglow emission.

Finally no correlation is found between central object parameters (found assuming the plateau the collapse of an unstable magnetar to a black hole) and flare parameters (found using pulse fitting). This may suggest that an unstable magnetar could not power traditional plateaus and that energy injection cannot explain the lack of the steep decline expected to be the signature of the magnetar collapsing to a black hole. However if it were the case that traditional plateaus were due to the collapse of a spinning magnetar, additional problems would be how they are gaining the energy to support their shallow decay. Furthermore for GRBs with an internal plateau and also a traditional plateau it is unclear how the later traditional plateau can be produced by a magnetar when by internal plateaus theory the magnetar should have already collapsed to a black hole.

Chapter 4

Giant flares: Could they be the main burst?

Abstract

About 50% of *Swift* GRBs have flares in their lightcurves, however in some cases the peak of this flare is comparable to the initial burst. In these cases how is it possible to be sure that the main burst is the first pulse and not a precursor so that what has been classified as a flare is actually the GRB? In this chapter I compare large flares to the burst and examine both with known precursors and the accompanying GRB.

4.1 Introduction

The standard model for GRB afterglows is a spherical blastwave expanding into a uniform density ambient medium, this should produce relatively smooth afterglow light curves. However, data from the *Swift* mission has shown $\sim 50\%$ of GRBs

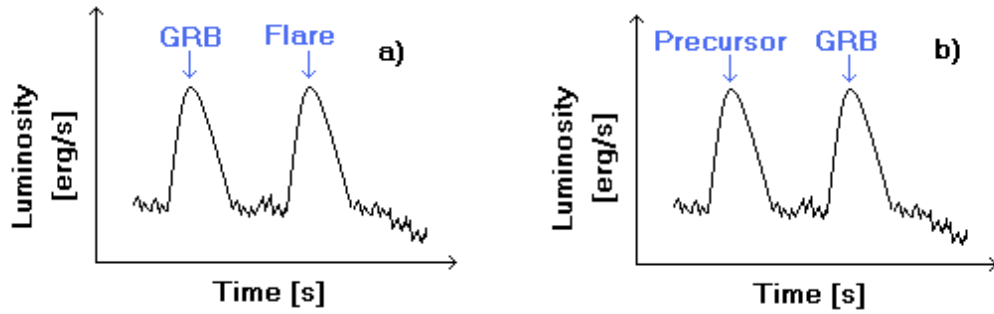


Figure 4.1: A schematic diagram of the luminosity of a GRB and giant flare as time passes. Panel a shows the usual definition of GRB and flare, for this chapter I investigate the scenario in panel a compared to precursors and the giant flares to examine if the scenario in panel b could be correct for some GRBs

have afterglows containing flares, although usually these flares have a fluence of only about 1 – 10% of that of the prompt emission, however in some GRBs the energy of the X-ray flare is comparable to that of the prompt emission.

Giant flares with a high fluence are studied in this Chapter, they are very bright and often beyond the burst T_{90} . In Section 4.1.2 we show that the definition of a precursor varies, I argue that due to the uncertainty in the classification between the GRB, giant flares and precursors, it is possible in these GRBs that the flare is the actual GRB and the burst before this is a precursor as shown in Figure 4.1, in this chapter I examine a sample of GRBs in this context.

4.1.1 Models for large flares

Burrows *et al.* (2005) suggests that these large flares are due to extended central engine activity, this activity has also been suggested to explain extended GRB tails seen by the BATSE instrument. In the light curve of GRB 050502B there is a second flare $\sim 10^5$ seconds this would imply that internal shocks are continuing

about a day later in the observer frame possibly due to fall back on to the black hole (MacFadyen, Woosley & Heger 2001, King *et al.* 2005).

Alternatively they suggested that external shocks encountering dense clumps in the nearby interstellar medium (Lazzati *et al.* 2002) could also explain giant flares. However since Burrows *et al.* (2005) there has been strong evidence that flares are not caused by external shocks i.e. the rapid rise and decay of most flares, some flares are superimposed on pre-existing decays which continue after the flare, observations of flares in ‘naked’ afterglows (e.g. GRB 050421) with no evidence for forward shock emission and (most relevantly for this chapter) the enormous flux increase in giant flares. (Chincarini *et al.* 2007, Burrows *et al.* 2007). These factors can be explained if flares are produced by internal shocks, additional observational evidence supporting this theory is the similarity between the shapes of X-ray flares and peaks in the prompt emission, also the spectral evolution of flares (discussed more in Section 3.01). The late internal shocks required to explain the flares in GRB 050502B could have been generated in two ways:

1. In the model proposed in Rees & Mészáros (1994) the central engine expels shells (discussed in more detail in Chapter 3, Sections 2.3 and 3.3) of material moving at different Lorentz factors, this causes collisions in the relativistic outflow generating internal shocks. These collisions can occur over a range of times, with late time collisions produced by two shells with very similar Lorentz factors. However in this model the resulting internal shock at late times may not carry enough internal energy to produce observable emission (Zhang 2006, Lazzati & Perna 2006).

2. Alternatively the central engine could be active at these late times erratically ejecting shells; Kobayashi, Piran & Sari (1997) found a strong correlation between the time a pulse is observed and the ejection time from the central engine, thus GRBs with flares observed $\sim 10^5$ seconds imply an ejection time days after the prompt emission is over. This model was tested in Liang *et al.* (2006) which found that the slope of the decay in flares is compatible with the aftermath of the curvature effect¹.

Chincarini *et al.* (2010) presents a sample of 113 X-ray flares detected by *Swift*, 43 of these flares have a measured redshift examines the evolution of flare temporal properties with energy, Margutti *et al.* (2010) takes 9 bright flares from the Chincarini *et al.* (2010) sample investigates the time lag for flares compared to prompt pulses. Both studies then fit flares with using a function proposed in Norris *et al.* (2005) that is the inverse of the product of two exponentials and is determined using the peak time, pulse width, asymmetry, the rise time and decay time of the flare.

Chincarini *et al.* (2010) examine the evolution of flares with energy in four X-ray bands and find that flares are sharper at larger energies where the flare width $w \propto E^{-0.5}$ similar to prompt emission, they also find that flares have an asymmetric shape where the time it takes a flare to decay is twice the time it takes to rise. Chincarini *et al.* (2010) concludes that flares are closely linked to the prompt emission and that no model is currently able to account for their observations.

Margutti *et al.* (2010) finds that although flares occur in all light curve morphologies they are more often superimposed in one break and canonical after-

¹The curvature effect describes the possible consequences due to the expanding fireball surface (Qin *et al.* 2006). For example emission along the line of sight stops and the emission is dominated by the radiation coming from the edge of the surface

glows. This flares in this study follow the same time lag (t_{lag}) luminosity ($L_{\text{p,iso}}$) relation as prompt pulses i.e. $L \propto t_{\text{lag}}^{-0.95 \pm 0.23}$ suggesting that prompt emission and flares are produced by the same origin.

In Chapters 2 & 3 GRB light curves are corrected into the rest frame for study partially due to time dilation i.e it should be mentioned that for GRBs with unknown redshift (which thus cannot be converted to the rest fame) time dilation delays the arrival time and broadens flares. However this cannot account for all late flares i.e. GRB 050724 is a short GRB with a flare ~ 1 day after the trigger, also demonstrating that the central engines of both long and short bursts can produce this behaviour.

If the central engine is still injecting significant energy into the blast wave at late times, how does it explain the short duration of gamma-ray emission? This can be explained by higher bulk Lorentz factors, which results in lower magnetic fields at the larger radius reached by the internal shocks at these late times (Burrows *et al.* 2007). Due to an earlier, more energetic GRB outflow expanding into the medium, the bulk Lorentz factor of X-ray flares cannot be determined by most models used to find the Lorentz factors of GRBs i.e. in Sari & Piran (1999) and Zou & Piran (2010), in these studies this. For internal shocks there are two speculations for the bulk Lorentz factor of flares: (1) The typical bulk Lorentz factor of flares is just tens, considerably less than that of the prompt outflow (Fan & Wei 2005) or (2) The typical bulk Lorentz factor of flares is just higher than that of the prompt outflow (Burrows *et al.* 2005, Zhang *et al.* 2006). Panaitescu *et al.* (2008) suggest that for the x-ray flare model of up-scattered emission from a forward shock emission, late outflow a bulk Lorentz factor $\sim 10^5$ is required. In this chapter we use a method developed in Jin, Fan & Wei (2010) to find the Lorentz

factor where possible for giant flare in my sample (discussed in more detail in Section 2.2).

4.1.2 Precursors

In many GRB models the main burst is preceded by a weaker burst with a thermal spectrum called a precursor, there is then a period where little or no emission is detected before the main bursting episode begins. Precursors were first proposed as occurring in Type II supernovae, though they were quickly incorporated into GRB theory. Colgate (1973) suggested that where the shock develops in a low density environment, the temperature behind the shock may be relatively low i.e. a few $\times 10^7$ K. The radiation mechanisms bremsstrahlung and inverse Compton scattering are slow compared to ion-ion thermalisation, thus a high-temperature ion precursor forms.

The first detected precursor was GRB 900126 roughly 10 seconds before the main burst as well as a tail of X-ray emission for 30 seconds. The spectra of the precursor was best fit by a blackbody model with $kT = 1.58^{+0.26}_{-0.23}$ keV (Murakami *et al.* 1991). In Section 1.3 we summarize the findings of the four studies searching through samples of GRBs for precursor emission.

Theoretical models of precursor emission can be separated into three classes: fireball precursors (Li 2007; Lyutikov & Blandford, 2003; Mészáros & Rees, 2000; Daigne & Mochkovitch, 2002; Ruffini *et al.* 2001), progenitor precursors (Ramirez-Ruiz, MacFadyen & Lazzati, 2002; Lazzati & Begelman 2005) and the ‘two step engine’ model (Wang & Mészáros 2007).

Fireball Precursors

The fireball model (Goodman 1986, Paczyński 1986) has been the standard model for GRBs discussed in detail in Chapter 1 Section 1.4. In this scenario it is assumed that a radiation dominated, optically thick and baryon-poor plasma fluid is suddenly produced in a compact volume. The radiation drives the fireball into relativistic expansion so that a significant fraction of the initial energy is converted into kinetic energy (Paczyński 1990, Shemi & Piran 1990). Later the fireball becomes optically thin and thermal radiation begins to escape, as the fireball expands its kinetic energy is converted to the prompt gamma-ray emission.

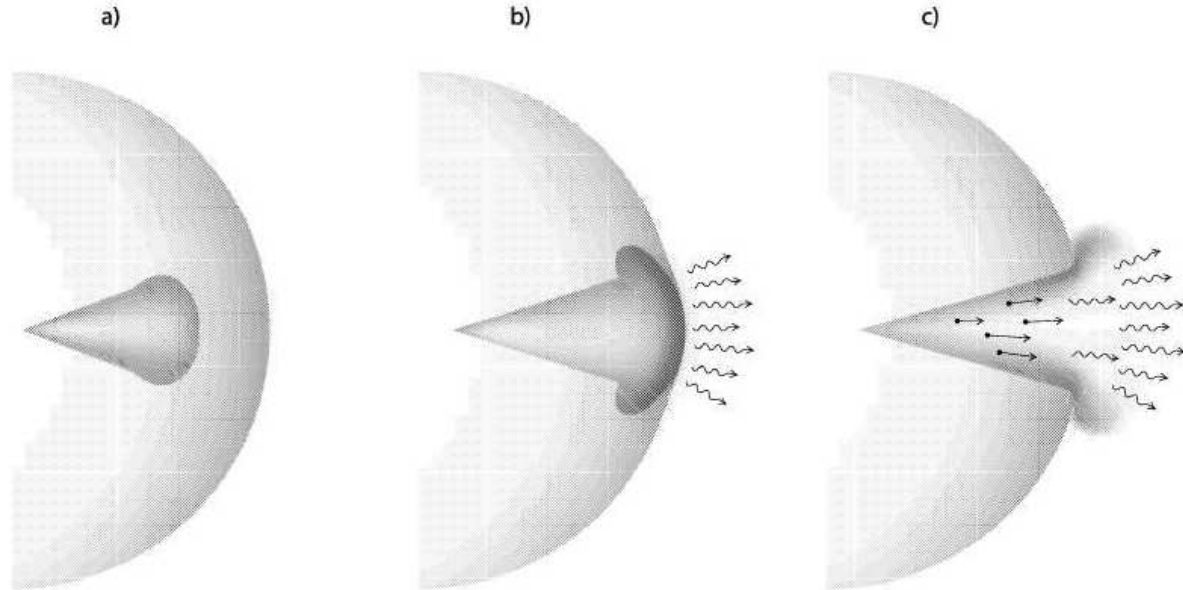
The radiation in the fireball has a finite energy, thus the remnant event must have a finite duration, the remnant event starts when the fireball is still optically thick, while the main episode occurs when the fireball is already optically thin (Li 2007). So the remnant occurs before the burst and thus at a smaller distance from the central engine than the main burst. As the remnant is produced by emission from the fireball photosphere it should have a quasi-thermal component, thus in a high energy band the remnant should appear weaker than the GRB. The remnant event should be observed as the precursor to the GRB (Li 2007).

Progenitor Precursors

The GRB emission is thought to be produced in shocks after the relativistic jet breaks free from the stellar envelope. Initially the jet is decelerated in the star causing a bow shock, which propagates ahead of the jet as shown in Figure 4.2, this is expected to produce transient emission, seen as a precursor with an expected blackbody spectrum. Although Ramirez-Ruiz *et al.* (2002) suggests that

the precursor could interact with the jet and produce a non-thermal spectrum via inverse Compton scattering if the jet is optically thin at the star's surface and non-thermal particles are present. (Ramirez-Ruiz, MacFadyen & Lazzati, 2002)

Figure 4.2: The propagation of the jet through the stellar mantle, initially the jet is unable to move the envelope material to a speed comparable to its own and is thus abruptly decelerated. As the jet propagates a bow shock propagates ahead (a), a strong thermal precursor is produced as the shock breaks the stellar surface and exposes the hot shocked material (b). The fireball escapes the stellar envelope and interacts with very dense photon emission (c) (Ramirez-Ruiz, MacFadyen & Lazzati 2002).



In Waxman & Mészáros (2003) it is shown that a series of shorter and harder thermal X-ray pulses are produced as successive shock waves pass through the stellar material as the jet pushes it beyond the boundary of the stellar envelope. In Ramirez-Ruiz MacFadyen & Lazzati (2002) it is suggested that these precursors could provide the radius of the progenitor, initial Lorentz factor of the fireball, the radial distance gamma-rays are produced and also the external medium surrounding the progenitor. One problem is that models predict that these precursors cannot be more than 10 seconds before the burst (Wang & Mészáros 2007), whereas precursors are observed much further before the burst than 10 seconds (Burlon *et al.* 2008).

Two step engine

The two step engine was proposed in Wang & Mészáros (2007) to account for the longer than expected delays (~ 100 seconds) between the precursor and burst. The 100 second gap was reminiscent of the timescales calculated for the fallback collapsar model (MacFadyen *et al.* 2001) where fallback begins minutes to hours after the initial core collapse. In this new model the collapse of the core produces a supernova and the star collapses to a proto-neutron star. The supernova shock is insufficient to eject all matter outside the star.

During the initial collapse of the star, a weak jet could be launched with an energy of few $\times 10^{50}$ ergs, either through magnetohydrodynamic processes in the core or propeller effects associated with a proto-neutron star (Wheeler *et al.* 2000). If this doesn't disrupt the star the fallback accretion described above produces the main burst. The progenitor is thought to have a non-thermal spectrum as it should be produced by internal shocks or reconnection.

Multiple precursors

Multiple precursors were first observed in GRB 011121 (Piro *et al.* 2005) and later GRB 030329 (Vanderspek *et al.* 2004). In more recent studies GRB 070306 has a precursor beginning at 118 seconds before the trigger a second precursor is detected 10^6 seconds later, each successive pulse is more powerful than the one before. Multiple precursors could be explained by an unstable jet with a constantly operating central engine with a modulated relativistic wind, causing gaps in emission (Ramirez-Ruiz *et al.* 2001).

Another suggestion for a three stage collapse is that a black hole or rapidly spinning neutron star (spinar) forms first (primary pulse) then a heavy accretion disc forms (second pulse), followed by a fatal collapse involving hyper-accretion of the star to a black hole. Another theory is that the accretion disc aggregated at some stage of a spinar evolution (Lipunova *et al.* 2009).

This raises the question why most GRBs (with precursors) do not display this three stage collapse, Fryer (1999) states that the fallback scenario works for GRBs that are not too weak or too strong. A weak explosion leads to a direct collapse to a black hole or a spinar if it has enough rotational energy to support it. Theoretical and computational evidence argues that rotation weakens the bounce and hence the explosion (Monchmever 1991, Yamada & Sato 1994) making a direct collapse more likely.

Previous searches for precursors

One of the key difficulties in studying precursors is the lack of objective criteria for exactly what emission is classified as a precursor, also searching for a precu-

sor implies looking for an emission episode before a GRB triggers the observing telescope or that the precursor is bright enough that it fulfils all the requirements for a GRB even though it is before the main burst. Here I examine the results of four previous studies; Koshut *et al.* (1995) hereafter K95, Lazzati *et al.* (2005) hereafter L05, Burlon *et al.* (2008) hereafter B08 and computer simulations by Lipunova *et al.* (2009) hereafter L09, each has differing definitions for a precursor.

The percentage of GRBs with a precursor in K95 is $\sim 3\%$ of BATSE GRBs detected before May 1994, in L05 $\sim 20\%$ of bright long bursts in the final BATSE catalogue are found to have precursors and in B08 found that $\sim 14\%$ from 105 GRBs observed before March 2008 by *Swift*. All these studies use different criteria to select bursts from observed GRBs, L09 uses a synthesized population to find a rate for GRBs with precursors of $\sim 10\%$ of all GRBs (roughly consistent with the rates found by previous observational studies).

K95 define a precursor as being from the same sky position as the GRB, having a smaller count rate than the main burst, that its emission must drop below the background before the main episode begins and the time it drops to this level to the main burst must have a separation at least as large as the duration of the main burst.

K95 finds that the typical separation between precursor and burst is ~ 100 seconds. K95 also finds that there is a correlation between the duration of the precursor and the duration of the GRB, however overall they find no substantial evidence that the properties of the main burst are dependent on the precursor emission.

L05 defined precursors as emission that must be detected and beginning to

decay before the GRB trigger, this is designed to pick up weak precursors, but exclude slowly rising GRB emission. Precursors were found to have a typical delay of ~ 30 seconds and had a non-thermal softer spectra contrary to the model predictions in Sections 1.21 and 1.22

B08 requires that precursor emission has a smaller flux in the *Swift* BAT (15-350 keV) light curve and that the flux falls below the background level before the star of the GRB. The two previous studies lacked known distances and hence could not pin down the energetics of each precursor, however B08 finds that the spectra and energetics of the precursor are indistinguishable from the main burst.

The spectra could appear to be non-thermal due to the convolution of black-body emission at different temperatures and/or from different locations consistent with a predicted thermal character. However on average the power-law fit spectral indices are very similar to the main event, this paired with the large energetics of the precursor is hard to explain. B08 suggested that the model discussed in Section 1.23 could reproduce this, or that this is a sign of the same mechanism producing the prompt emission. B08 finally investigate two ‘postcursors’, in GRB 060210 they find that the spectra is softer and the energetics weaker than the burst and the precursor. As this is only one burst no general conclusions can be drawn.

L09 predicts that precursors could occur $\sim 10^3$ seconds before the main burst for the model discussed in Section 1.23, they find pulses could occur $\sim 10^6$ seconds before the main burst, but that these pulses could be too weak to be detected or form a jet. L09 predicts that separations ≥ 1000 seconds as separations of ~ 100 seconds in the rest frame have been seen (Burlon *et al.* 2008) and bursts with $z \geq 10$ are expected to be found (Salvaterra *et al.* 2008).

4.2 Method

4.2.1 Spectral Energy Distributions

To produce a spectral energy distribution (SED), first the overlap between the BAT datafile and data taken in Windowed Timing (WT) mode was found, using the `fkeyprint` command to compare the start and end time of files to the trigger time. The time interval the spectra would need to be extracted for in each datafile was recorded. The bat spectra was extracted over these times using `batbinevt` command with an energy bin list set to `CALDB:80`² and then create a response file was created (so that the data could be read into Xspec) using the `batphasyserr` and `batdrngen` commands.

For the X-ray data `xselect` was used to produce region files for the burst and the background areas in the image, the spectra was then extracted in these regions over the selected times. The `xrtmkarf` command was used to produce a Ancillary Response Function (ARF) file, this was then grouped with the background spectra and the WT response file using the `grppha` command. The BAT and WT spectra were then read into Xspec with channels outside the 15-150 keV and 0.3-10 KeV respectively were ignored, finally the following models were fit to the BAT and WT spectra: a powerlaw, a broken power law, a powerlaw plus black body emission and a power law with an exponential cutoff.

²This uses the 'standard' 80 channels which are defined in the calibration database

4.2.2 Obtaining Lorentz factors

Jin, Fan & Wei (2010) propose a method to estimate the Lorentz factor for giant X-ray flares, based on the curvature effect interpretation of the quick decline of the flare. This method provides a tightly constrained Lorentz factor, but can only be applied to some giant flares as the half opening angle of the jet θ_j is required.

The rapid decline of X-ray flares may have placed a tight constraint on the emission radius R_x (Zhang 2006, Lazzati & Begelman 2006) provided the decay is high latitude emission (Fenimore *et al.* 1996, Kumar & Panaitescu 2000) (discussed in more detail in Chapter 3 Section 1.2). If this is true it requires a high variability timescale δT (Fan & Wei 2005), thus if R_x and δT can be estimated then the bulk Lorentz factor can be found using $\Gamma_x \approx [R_x/(2c\delta T)]^{1/2}$ (Jin, Fan & Wei 2010), where all following timescales are in the rest frame. Jin, Fan & Wei (2010) then use $\delta T \sim T_p - T_0$ the bulk factor in terms of luminosity and radius (Mészáros & Rees 2000, Nakar, Piran & Sari 2005, Fan 2010) and an approximation of the net flux in colliding shells to produce Formula 4.1. Where T_0 is a good approximation of the ejection time of the last dominant pulse, T_p is the peak time of the dominant pulse, β is the spectral index and R is the ratio of the flare peak flux $F_{x,p}$ and the flux where a cutoff emerges $F_{x,c}$.

$$\Gamma_x \approx R^{1/[2(2+\beta)]}/\theta_j \quad (4.1)$$

In this chapter using the rest frame lightcurve I fit a powerlaw to the afterglow plus a gaussian to fit the flare for the time it peaks, after this the time at which the gaussian crosses the powerlaw is recorded. The flux at these times is then used to calculate R . In Racusin *et al.* (2009) they find the opening angles for jet breaks

in *Swift* afterglows, opening angles for possible jet breaks are found for GRB 060124 and GRB 060525, these are used to estimate the flare opening angle using $\theta_{j,\text{flare}} \sim 0.7\theta_{j,\text{GRB}}$ (Jin, Fan & Wei 2010), for the other GRBs in this sample the opening angle was assumed to be the mean of the prominent jet break group i.e. 5.56 degrees giving a standard error for on each opening angle of ± 0.83 degrees. Finally β is found using the relation $\beta = \text{Photon Index} - 1$. After obtaining a Lorentz factor I use Formula 4.2 to estimate the accretion rate (Jin, Fan & Wei 2010), where L_{50} is the flare luminosity in units of $10^{50} \text{erg s}^{-1}$

$$\dot{M} \sim 5 \times 10^{-6} L_{50} \Gamma_x^{-1} M_{\odot} \text{s}^{-1} \quad (4.2)$$

4.3 Data Analysis

The flares selected to be examined in this Chapter had a high count rate of ≥ 85 counts per second and were a factor of ≥ 30 brighter than the afterglow flux, as a final requirement both the rise and decay of the flare needed to be observed. The GRBs with giant flares used in this sample are shown in Figures 4.4 to 4.6 and discussed briefly below:

GRB 050502B has the longest giant flare, also a smaller flare at $\sim 10^5$ seconds (discussed in more detail in Section 1.1) and in Jin, Fan & Wei (2010) was found to have Lorentz factor of 22.

GRB 060124 is interesting as well as a giant flare beginning at ~ 350 seconds and it also has a precursor 1.5 seconds before the trigger. It also has a redshift of 2.298 and evidence of a second pulse during the giant flare.

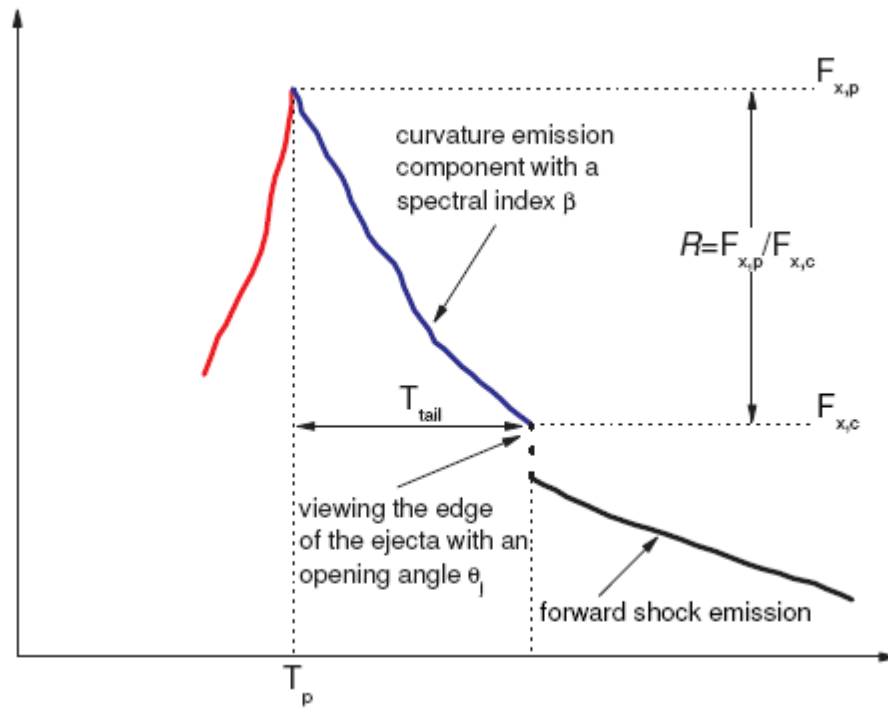


Figure 4.3: A schematic diagram of the curvature emission component that is used for the method used to find giant flare Lorentz factors. Where R is the ratio between the peak flux of the X-ray flare $F_{x,p}$ and the flux when a cutoff emerges $F_{x,c}$. T_{tail} is the time the curvature emission component ends (Jin, Fan & Wei 2010).

GRB 060526 has an upper limit on the GRB Lorentz factor of 247 and evidence of another shell collision during the flare. This GRB also has a redshift of 3.21.

GRB 061121 has the highest count rate ($\sim 3,200$ counts per second) for the giant flare in this sample and also a precursor 5 seconds before the trigger time. This GRB also has a redshift of 1.314.

GRB 070704 has a giant flare beginning at 256 seconds.

GRB 100619A had the earliest giant flare, beginning just 42 seconds after the burst, most interestingly it also has a second giant flare in its light curve has the latest start time in the sample 850 seconds.

Chincarini *et al.* (2010) also find that flare width evolves with the flare peak time (T_p) linearly so that $w \sim 0.2T_p$, which distinguishes it from prompt emission pulses where the width is constant (Norris *et al.* 2005). Margutti *et al.* (2010) finds that the bright flares also become wider at later times, with lower luminosities and softer emission. The sample selected in this chapter are extreme even for bright flares, three of these flares are included in Chincarini *et al.* (2010), too few to derive a relation, however using their fitted parameters for these bursts, only one flare lies within a standard deviation of $w \sim 0.2T_p$.

Table 4.1: The observed and rest frame properties of the GRBs and giant flares in my sample. Where E_{iso} is the isotropic energy released in either the GRB or the flare, denoted by the subscript

GRB	T_{90} Seconds	Peak Flux (0.3-10 keV) $10^{-8} \text{ erg cm}^{-2} \text{ s}^{-1}$	Start time Seconds	End time t_e Seconds	Rest frame t_e Seconds	$E_{\text{iso,flare}}$ 10^{52} erg	$E_{\text{iso,GRB}}$ 10^{52} erg
050502B	17.1	0.418	284.54	1827.31	567.5	4.17	0.546
060124	13.6	4.05	178.11	950.09	125.2	5.42	1.78
060526	298.2	4.94	198.16	608.67	318.3	11.2	11.5
061121	81.3	25.5	34.61	217.48	54.5	4.53	4.93
070704	380	1.03	256.87	676.26	173.5	3.62	6.2
100619A	97.5	12.6	42.10	197.60	47.7	14.4	28.1
100619A	97.5	0.796	854.90	1558.0	466.9	3.87	28.1

Temporal & Spectral Analysis

The long bursts in Table 4.1 all have T_{90} longer than 10 seconds implying that they cannot be a progenitor precursor. For these GRBs no thermal component is reported during the burst for any GRB in this sample (Cannizzo *et al.* 2010, Markwardt *et al.* 2007, Page *et al.* 2007, Page *et al.* 2006, Markwardt *et al.* 2006, Fenimore *et al.* 2006 & Cummings *et al.* 2005) which is also expected for both the fireball and progenitor precursor models, although a possible explanation for the lack of a thermal component is given in Section 4.1.2. Due to the relatively long T_{90} measurements, lack of thermal emission and powerful central engine activity here I favour the Two Step Engine (discussed in Section 1.24) as the central engine causing this activity if the GRB is a precursor for the giant flares excluding those in GRB 100619A.

It has been found that precursors are generally softer than the burst (K95, Murakami *et al.* 1991, L05), in Figures 4.4 to 4.6 the giant flares vary in the hardness ratio the flares appear to be harder than the initial burst, however in GRB 100619A the photon index in each flare appears to be getting softer for each successive pulse. For GRB 100619A the only model for precursors that can explain the second giant flare is that of multiple precursors, if this were the case the final giant flare should be the most powerful due to the fatal collapse discussed in Section 4.1.2 following the behaviour also seen for GRB 070306 with multiple precursors (Ramirez-Ruiz *et al.* 2001). For GRB 100619A each progressive giant flare producing less flux than the flare (or GRB) preceding it which disagrees with this hypothesis. Chincarini *et al.* (2010) also find that when a GRB contains multiple flares each flare is on average softer than the previous one,

so the softening of successive flares in GRB 100619A also agrees with normal flare behaviour.

B08 (in Section 4.1.2) found that the spectra of precursor and burst are indistinguishable (contrary to my previous findings in this Section) thus they suggested that same mechanism produces the prompt emission in the burst and progenitors, B08 also investigates flares in a GRB as ‘postcursors’. For completeness I use spectral energy distributions to model the spectra of the flares, the results from the best-fitting models are shown in Table 4.2, where n is the absorbing column density. For GRB 050502B, GRB 060124 and the second flare in GRB100619A there was no overlapping data between the BAT and WT mode, in these cases the WT data is modelled alone. In all of the giant flares in Table 4.2 no thermal component is seen.

Table 4.2: The time cuts used for the model fitting of each giant flare and the results for the best fitting models to the giant flare spectra.

GRB	Time Cut Seconds	Best Model	Photon Index	n atoms cm^{-2}
050502B	550-1000	Power law	2.27 ± 0.1	0.27×10^{21}
060124	400-850	Power law	1.40 ± 0.02	6.02×10^{21}
060526	150-170	Power law	1.86 ± 0.53	2.73×10^{21}
061121	62-138	Power law	1.37 ± 0.06	2.33×10^{21}
070704	160-289	Cut-off Power law	1.89 ± 0.062	1.22×10^{22}
100619A	81-125	Power law	1.25 ± 0.12	4.58×10^{21}
100619A	905-1250	Power law	2.21 ± 0.06	4.47×10^{21}

The hardness ratios in Figures 4.4 to 4.6 show that the giant flares showed

the standard flare spectral tendencies (Burrows *et al.* 2005, Falcone *et al.* 2006, Romano *et al.* 2006) i.e. the spectra were harder than the underlying afterglow and an evolution from hard to soft was seen over time where the peak hardness occurred before the peak in the light curve. The photon indices during the flare show spectral evolution beginning with a dip which turns over \sim to the peak of the flare in the light curve (except for GRB 050502B where there is a gap in the photon index around where a dip could be expected and continues to rise throughout the flare). In GRB 060526 & GRB 070704 the dip in the photon index can be seen before the giant flare dominates the afterglow emission.

For three of the six GRBs there is a gap in the data or a single data point with large errors so there is no way to conclude if there is any spectral evolution during the quiescent period between the prompt emission in the burst and in the giant flares. For the remaining three no identifiable spectral evolution is seen during this period. The quiescent periods between the precursor and main burst are periods of low flux thus it has not been possible to extract meaningful spectra during these times, also the hardness ratio had large errors (Hurkett *et al.* 2008b), thus it is not possible to conclusively state if spectral evolution is taking place over these times.

No well defined spectral evolution trend can be seen throughout the burst although in four of the six bursts there are a small number of data points and in GRB 050502B large error bars, of the remaining bursts GRB 100619A and GRB 061121; GRB 100619A shows the most complex behaviour with multiple peaks and troughs - also the trough at ~ 2 seconds appears similar in size to that the later giant flares, at early times (≤ 4 seconds) GRB 061121 seems to also show less pronounced variations. In the part of the light curves detected by the BAT the flares that can be seen have a relatively similar flux as the giant flares present in the

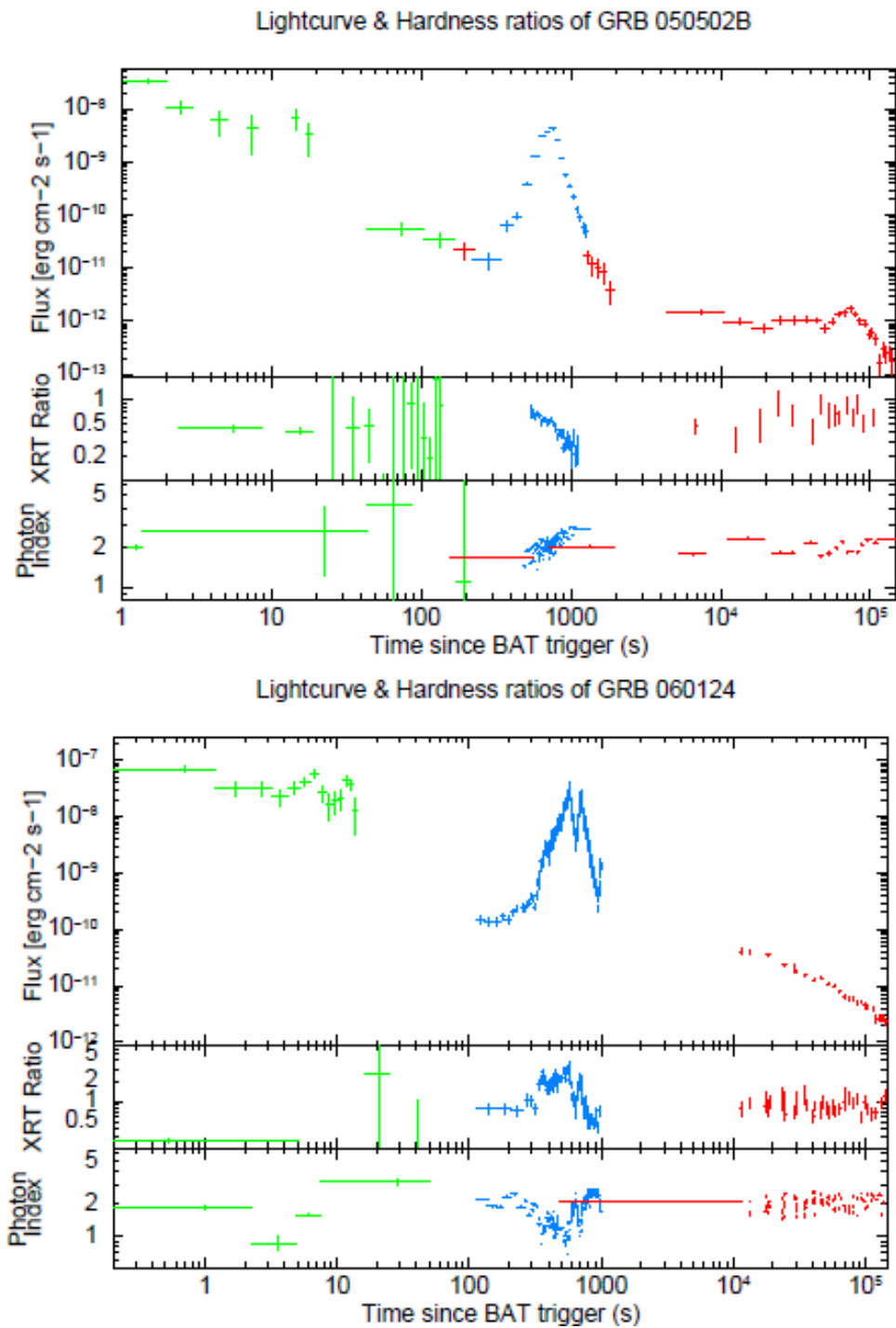


Figure 4.4: The lightcurves, hardness ratios and photon indices of GRB 050502B and GRB 060124. The photon indices were supplied by the UK Swift Science Data Centre at the University of Leicester (Evans *et al.* 2007)

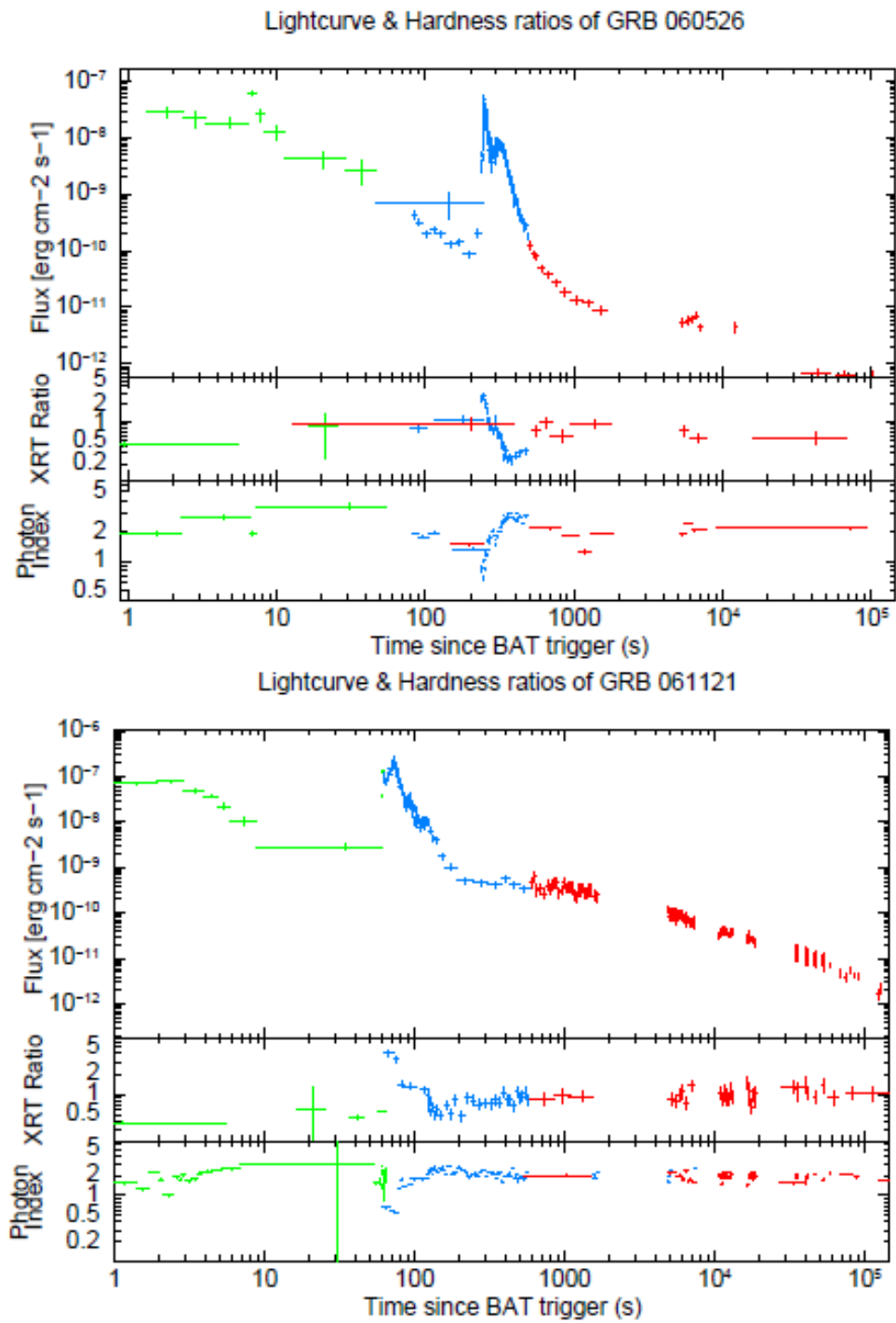


Figure 4.5: The lightcurves, hardness ratios and photon indices of GRB 060526 and GRB 061121. The photon indices were supplied by the UK Swift Science Data Centre at the University of Leicester (Evans *et al.* 2007)

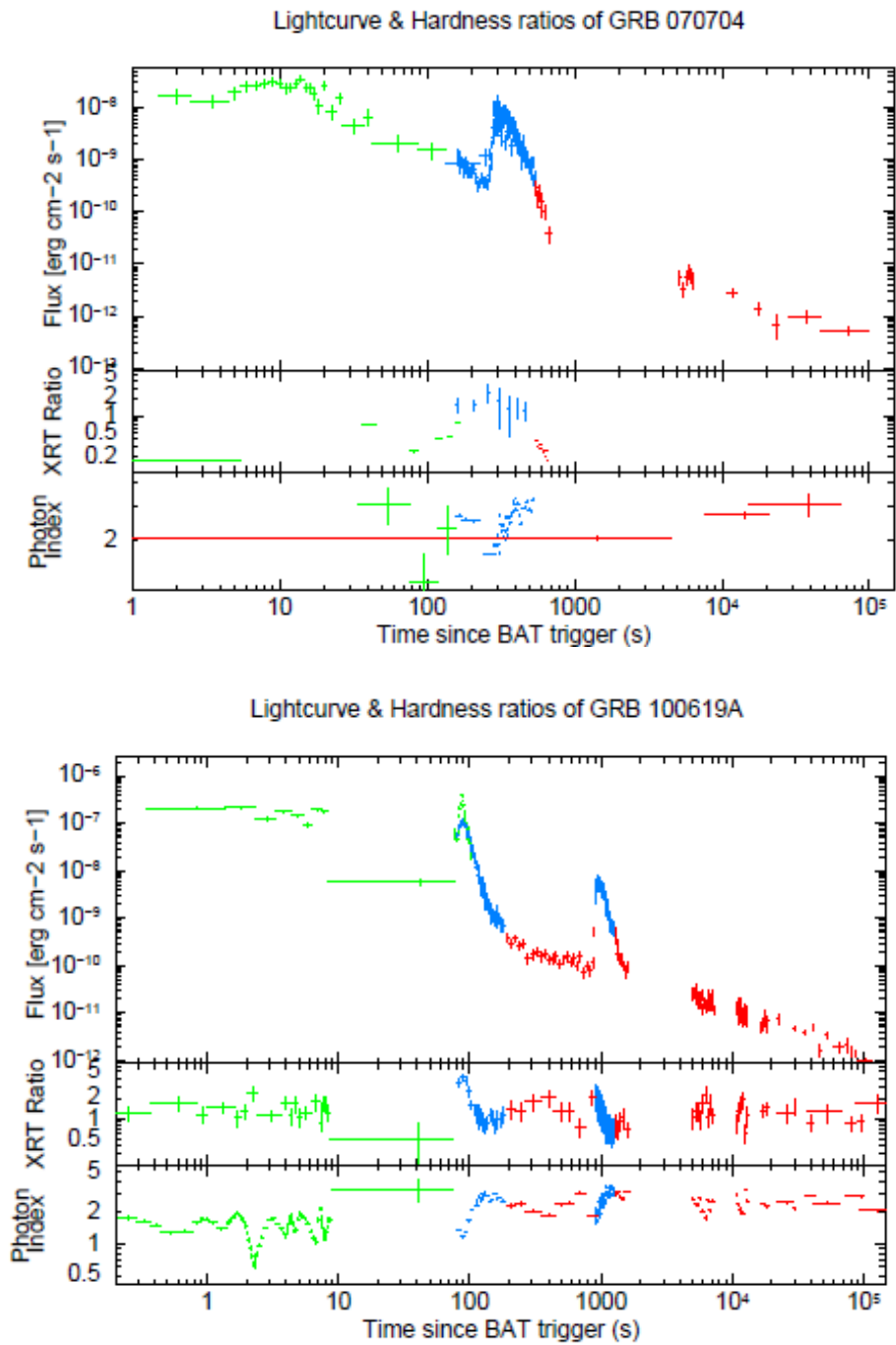


Figure 4.6: The lightcurves, hardness ratios and photon indices of GRB 070704 and GRB 100619A. The photon indices (and hardness ratio for GRB 100619A) were supplied by the UK Swift Science Data Centre at the University of Leicester (Evans *et al.* 2007)

XRT data, save that if the each of the troughs in the BAT data in GRB 100619A correspond to a flare of similar flux to the giant flares observed in the XRT data there multiple pulses are ejected in in the first 10 seconds of these long bursts to produce the isotropic energies similar to the single (or in two cases double) pulse in the giant flares.

Dado & Dar (2010) find that the evolution of the spectral index for GRB 050502B is well described by the cannonball model³ with inverse Compton scattering during a flare. In this chapter I do not investigate the cannonball model, but as well as modelling spectral evolution for flares it also makes a prediction that flares which can be modelled by this scenario and do not have accompanying detectable gamma-ray emission should have relatively smaller Lorentz factors due to the weakening of the central engine as the accretion material is consumed. The Lorentz factors of the giant flares are examined later in this section.

GRB 100619A has the longest lasting spectral evolution in the BAT showing clear peaks and troughs; and also a significantly higher $E_{\text{iso,GRB}}$ (almost double that of the first giant flare). Alternatively it could be that these pulses are producing more much energetic GRB emission and other GRBs with large errors on the BAT data do not have significant spectral evolution over the GRB, hence why the isotropic energy of the burst is much more similar to the giant flare for these GRBs. However, it should also be noted that GRB 100619A is also the only burst in this sample with two giant flares, so extra internal energy is going into launching a second flare, this GRB emits $\sim 14\%$ of its burst isotropic energy in the two

³The many similarities between the prompt emission pulses in GRBs and flares during the fast decay and afterglow phases of GRBs suggest a common origin. In the cannonball model of GRBs this common origin is mass accretion episodes of fall-back matter on a newly born compact object (Dado & Dar 2010)

flares.

Comparison with B08

Some of the GRBs in my sample are also recorded as having precursors in B08, hence I compare the properties of the bursts with giant flares in my sample to their precursors and also GRBs in general with precursors (in B08). One of the requirements for precursors in B08. For five out of seven of the giant flares the GRB has a higher E_{iso} in Table 4.1 and is that they have less flux than the GRB (in the band 15-350keV), thus it is unsurprising that the giant flares are more energetic in Figure 4.7. If we consider the scenario defined in Figure 4.1 panel b, could not be precursors according to the criteria set in B08. The bursts with giant flares also have a greater range in isotropic GRB energies and do not seem to be correlated with the GRB isotropic energy. They also do not appear to have a relation with precursors in their light curve.

In Figure 4.8 there appears to be a correlation where GRBs with long durations produce shorter quiescent intervals for between the burst T_{90} and the quiescent period. The one outlier being the only GRB in my sample with a second giant flare, however when taking into account the other GRBs with precursors in B08, three new outliers are produced two of which are for GRB 070306 which has two precursors, I would have expected that the second precursor may be an outlier, it seems strange if this is the case that the first precursor would be an outlier, but GRB 100619A's first flare not also being one. Alternatively the two outlier GRBs are have a longer duration by 100s than any other GRB producing a precursor in B08.

Drago A. & Pagliara (2007) models quiescent periods for GRBs in the BATSE

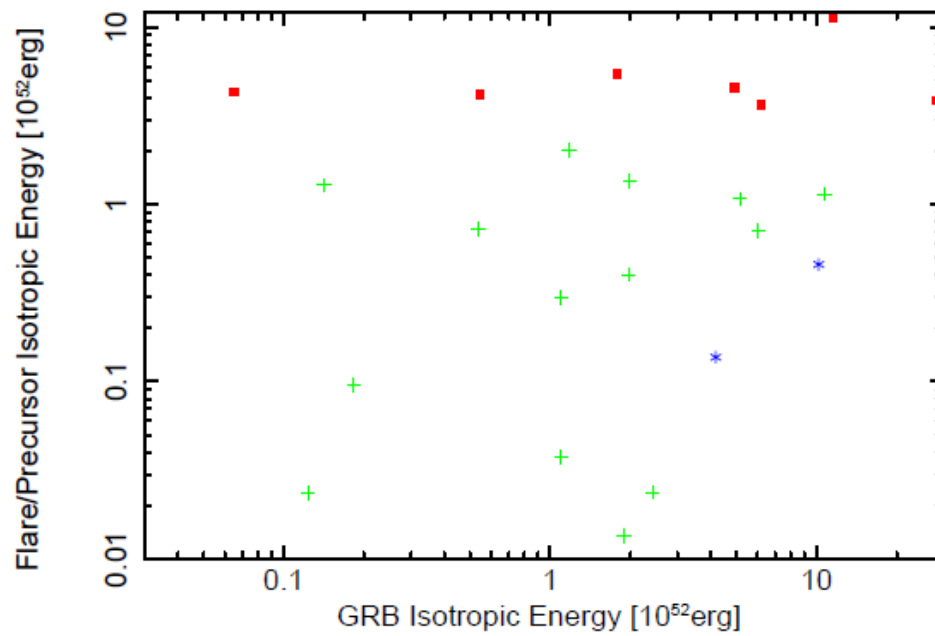
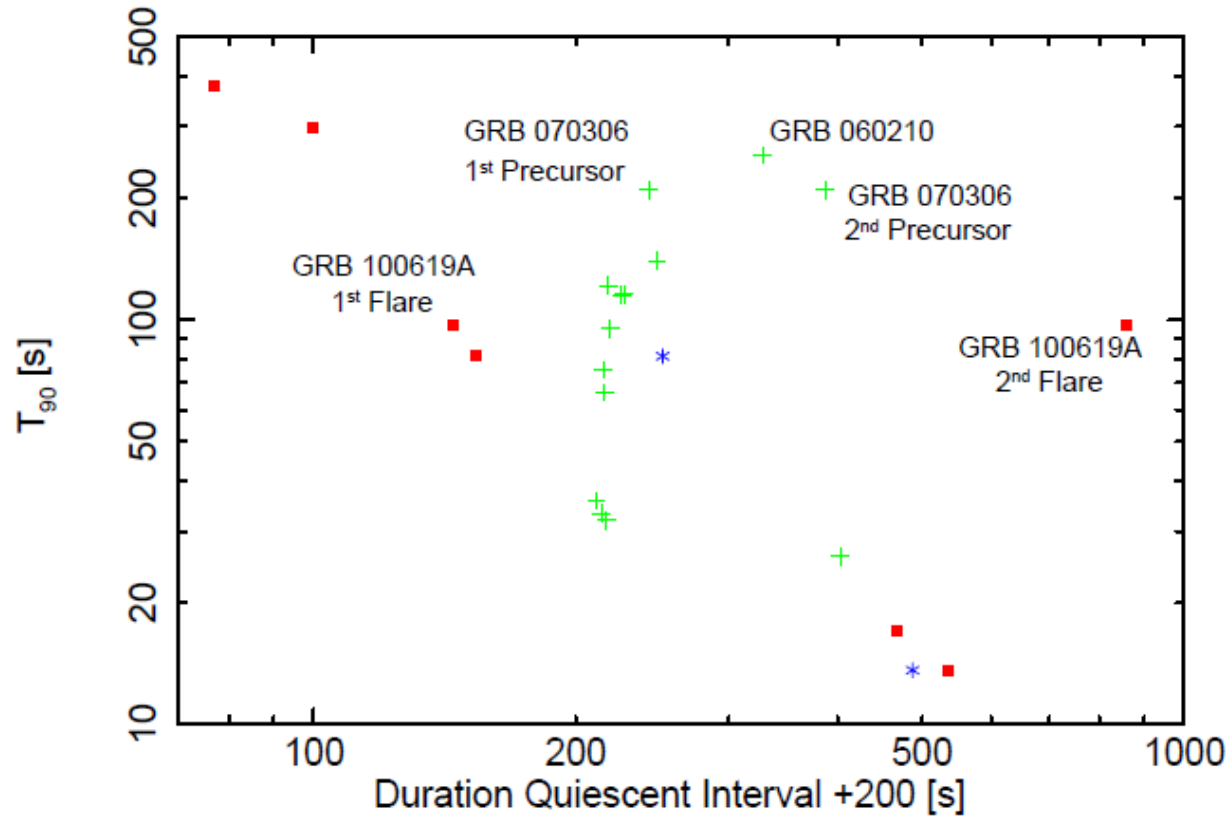


Figure 4.7: The isotropic energy of the giant flare/precursor plotted against the isotropic energy of the GRB. GRBs with giant flares (red spots) are then compared to GRBs with precursors from B08; where blue stars denote GRBs that are also in my giant flare sample and green crosses all other GRB in B08

band (55-350 keV) examining periods of central engine activity lasting a few tens of seconds, could accurately describe the progenitors in B08, but not the giant flares. They find that the emission after the quiescent period lasts about twice as long as the emission preceding it, this is not the case for precursors in Figure 4.8 and is also not for giant flares.

Figure 4.8: The relationship between the burst T_{90} and the quiescent period between GRB and flare or precursor. The GRBs with giant flares are shown by red spots, whereas the blue stars are GRB with precursors that are in B08 and also in my giant flares sample, all other GRBs with precursors in B08 are represented by green crosses.



Lorentz Factors

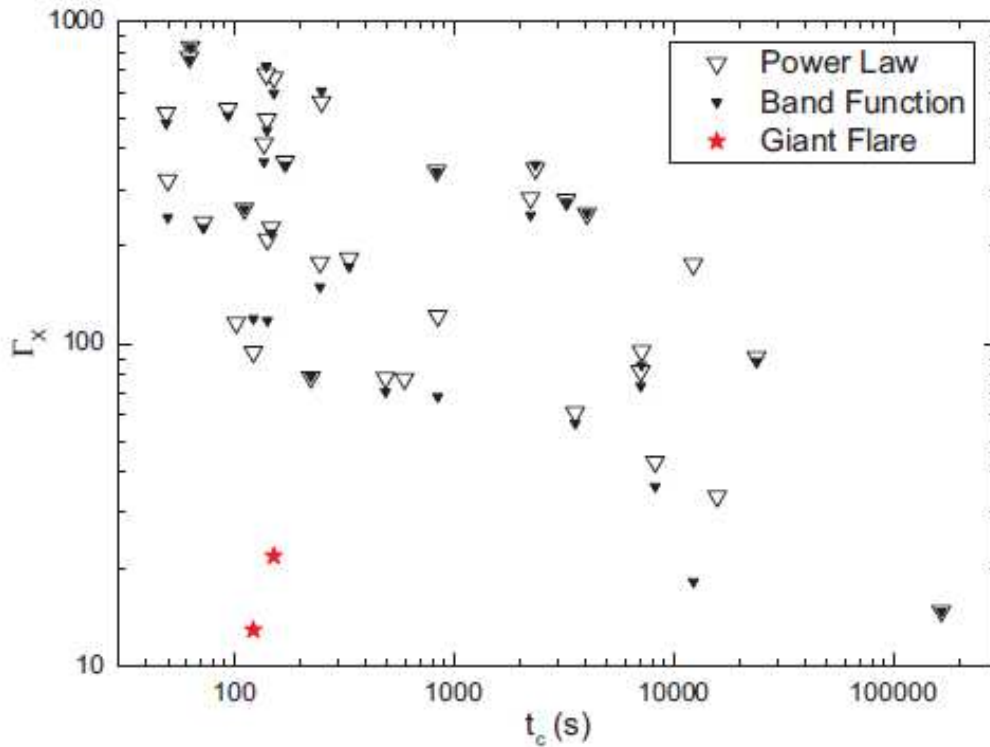
The Lorentz factors are $\ll 10^5$ and thus are inconsistent with the expectations from Panaitescu *et al.* (2008) (discussed in more detail in Section 1.1) this could be because the acceleration is from something other than thermal pressure or due to the shocks generating flares being produced by energy dissipation (discussed in Section 1.1).

Table 4.3: The parameters found for each giant flare using Formula 4.1, the results for the giant flare for GRB 050502B is found in Jin, Fan & Wei (2010), the centre time of each flare is also included for comparison with results found in Jin, Fan & Wei (2010).

GRB	θ_j	R	β	Γ	T_c [s]	$\dot{M}[10^{-7}M_{\odot}s^{-1}]$
050502B	0.13	1100	1.3	~ 22	771.4	3.65
060124	0.013	257	0.3	~ 261	386.0	3.24
060526	0.023	110.	1.0	~ 95	205.3	24.6
061121	0.034	253	1.05	~ 72	91.4	18.5
070704	0.034	54	1.4	~ 52	209.7	3.79
100619A	0.034	111	0.17	~ 87	77.8	27.9
100619A	0.034	70	1.04	~ 59	351.6	1.72

Jin, Fan & Wei (2010) compare the time of the centre of the flare T_c to the Lorentz factor of normal and two giant flares as shown in Figure 4.9. The giant flares in Table 4.3 all occupy the same region as the two giant flares in Jin, Fan & Wei (2010), separate from normal flares. Dado & Dar (2010) predict that the giant flare GRB 050502B should have a relatively small Lorentz factor which is supported by the lorentz factors in Table 4.3, but this is a small sample group of flare

Figure 4.9: The upper limits of the bulk Lorentz factor of the outflow powering GRB flares and the centre time of the flares. The hollowed and filled triangles are where the spectrum is assumed to be modelled by a single power law and the band function respectively. In black are normal flares and the red stars are two giant flares (Jin, Fan & Wei 2010).



Lorentz factors. A future study could expand upon this sample and also model other GRBs to see if the spectral evolution can be modelled by the cannonball model with inverse Compton scattering during the flare.

Unfortunately there is not a recorded Lorentz factor the GRBs in my sample, so it is not possible to compare the Lorentz factors of the flares to the Lorentz factors of the same burst. Liang *et al.* (2010) has a list of initial Lorentz factors for 16 GRBs which vary from 110-1000, these Lorentz factors are derived by the detection of the X-Ray onset bump, Optical forward shock peak time or by a tight

limit for the onset time of the forward shock emission. Comparing these GRB initial Lorentz factors to the values in Table 4.3 this provides a further way to distinguish between the burst and giant flares for 6 of the 7 giant flares.

If we assume that this range of Lorentz factors (Liang *et al.* (2010)) is constant for the prompt emission, most of the flares in table 4.3 have Lorentz factors closer to the Fan & Wei (2005) speculation favouring late internal shocks produced by an unsteady refreshed outflow generated by the central engine after the prompt emission. GRB 060526 has a recorded upper limit on the Lorentz factor of the GRB of 247 (Oates *et al.* 2009), which seems to support Burrows *et al.* (2005) & Zhang *et al.* (2006). Overall my sample seems to imply that this is not the typical bulk Lorentz factor of flares, but that for some flares the bulk Lorentz factor \sim tens as is found in (Fan & Wei 2005). Although this is a very small sample with only one upper limit on a GRB Lorentz factor for comparison, future studies with a large number of flare and GRB Lorentz factors may find that this is not the case.

4.4 Conclusions

If the GRBs in my sample were really precursors as shown in Figure 4.1, I favour the precursor model for a short lived neutron star which then collapses to a black hole (discussed in Section 1.24), due to the lack of thermal emission found in the spectra and also the long durations of central engine activity required for some GRBs (i.e. up to a maximum of ~ 450 seconds in the rest frame).

In comparison to GRBs with precursors in B08 I find that bursts with giant flares also have a greater range in isotropic GRB energies and do not seem to be correlated with the GRB isotropic energy or have a relation with precursors in

their light curve, or other GRBs with precursors. I find a possible correlation that GRBs with a short duration tend to have shorter quiescent intervals between either the precursors and GRB or giant flares and the GRB.

In Section 4.3 I find some evidence of evolution during the burst and also the giant flares, suggesting that the GRB is the product of many shells colliding producing the observed emission, whereas for giant flare usually a smoother evolution with at most evidence of one other pulse contributing to the emission. Perhaps for GRBs with good BAT data this could be used to distinguish between the giant flare and the main burst. This also seems to go against the idea that the GRBs in my sample could be precursors and the giant flares the main burst episode as in B08 it was found that precursor emission is indistinguishable from other prompt pulses. Unfortunately I do not find enough evidence to state if spectral evolution is occurring during quiescent times.

For 6 of the 7 giant flares the Lorentz factors are outside the range given by 17 GRBs with known initial Lorentz factors, providing a further way to distinguish between a GRB and giant flare of similar fluence. The Lorentz factors of these giant flares imply that for some flares the bulk Lorentz factor \sim tens as is found in (Fan & Wei 2005). Although this is a very small sample with only one upper limit on a GRB Lorentz factor for comparison, future studies with a large number of flare and GRB Lorentz factors may find that this is not the case.

To conclude there is some evidence that these giant flares are different to normal flares - occupying a different region from normal flares in Figure and also not obeying the relation for normal flares $w \sim 0.2T_p$ found in (Chincarini *et al.* 2010). Overall my findings in this Chapter do not rule out that the GRB could be a precursor and that the giant flares are the real GRB as shown in Figure 4.1, how-

ever it seems unlikely as five out of seven of the giant flare are not more energetic than the original GRBs which would rule out the GRBs as precursors by the criteria set out in B08, also for GRB with good BAT data the spectral evolution is different during the GRB and giant flares. The Lorentz factors found for most of my sample also lie outside that of published GRB initial Lorentz factor also providing an distinguishing factor between GRBs and flares of similar fluence, although this is based on a relatively small sample providing an upper limit on the GRB Lorentz factor.

Chapter 5

Conclusions & Future Work

5.1 Thesis Overview

The first investigation performed in this thesis was examining an unexpected feature in the light curves of some GRBs which looked like the signature of a magnetar (i.e. a period of constant emission followed by a steep decline). This feature could not be fitted by the Willingale model as being produced by the prompt or afterglow component and was called an internal plateau to differentiate it from the traditional plateau.

The dipolar spindown law (Zhang & Mészáros 2001) was used with the luminosity and end time of the internal plateau to place constraints for the rotational period and the magnetic field of the central object. These were consistent with a proto-magnetar and theoretical limits i.e. the breakup-spin of a neutron star. Bucciantini *et al.* (2007) suggests a method for proto-magnetars to produce collimated outflows, thus I also investigated the beaming angles of 4 and 18 degrees. The largest magnetic fields implied for isotropic emission are consistent with field

strengths of $\sim 10^{16}\text{G}$ which can be generated in magnetars born with a spin of a few milliseconds (Thompson & Duncan 1993, Duncan 1998), but need to be collimated to produce periods that do not violate the break-up spin of a neutron star.

Next I wanted to compare traditional plateaus for GRBs with known distance to the internal plateaus found in the previous chapters to see if these could be formed by the same process. The early internal plateaus stand out as separate from the traditional plateaus in terms of the magnetic field and rotational period of their central engine, even the late internal plateaus which end on a similar timescale to traditional plateaus have a more extreme luminosity than most traditional plateaus.

This was expanded to consider the global trends of GRBs with a known redshift and also flares in their light curves. Like internal plateaus, flares are thought to be produced by central engine activity, so for GRBs with plateaus I then compared the limits they placed on the central engine to the properties of flares in each of these light curves, however, no correlations were found. The shape of the light curve was also investigated in Chapter 3 with flaring behaviour. Normal flares tended to have a similar percentage occurring in each light curve shape as all GRBs with a redshift measurement suggesting they occur independently to light curve shape. Giant flares however seem to preferentially occur in canonical light curves or light curves with one break.

Since finding that giant flares behaved differently than smaller flares I decided to investigate giant flares compared to the main episode of emission, questioning if they might be the burst and the GRB actually a precursor. Contrary to the fireball and progenitor models for precursors I did not find a thermal component in the GRB spectra, this combined with the long duration required of activity from the central engine implied that the GRB is not a precursor. However the case that the

GRB is a precursor, I find that it is likely to be from a short lived neutron star, providing up to 1,000 seconds for central engine activity Lipunova *et al.* (2009). Finally I used a new method proposed in Jin, Fan & Wei (2010) to find lorentz factors of giant flares and estimated the baryon loading on to the central object.

5.2 Thesis Summary

Swift has detected over 500 GRBs since its launch, for 96% an X-ray afterglow is also found, while the optical/UV afterglow is found for 60% of GRBs (Burrows *et al.* 2008). This large number of GRBs with multi-wavelength data has enables this thesis to find features in the light curve that relate to the progenitor or central engine of the burst. In this section I will discuss how three key topics in the GRB research field and how this thesis has contributed to this field.

5.3 What is the central engine?

The first issue I investigate is the central engine, it has been determined that it must be a compact star with radius $> 10^7$ cm that converts a fraction of its graviational energy into collimated jets (Nakar 2010). However there are two main models for the object powering the GRB emission; the first model is for accretion onto a black hole and in thesecond model a millisecond proto-magnetar has been suggested (Usov 1992, Thompson 2007).

In Chapter 2 I consider the collapse of a massive star and suggest that it may temporarily form a rapidly rotating neutron star before collapsing to a black hole, producing a plaateau followed by a steep decline ($\alpha \geq 4$) which cannot be pro-

duced by other models such as fall-back accretion (Kumar *et al.* 2008). For 10 GRBs that display this feature I find the largest magnetic fields of the progenitor implied isotropic emission are consistent with field strengths of $\sim 10^{16}$ G which can be generated by in magnetars with a spin of a few milliseconds (Thompson & Duncan 1993; Duncan 1998) assuming radiation is beamed. Thus these limits could provide a method for identifying GRB engines if found consistent with theoretical limits (such as the break-up spin of a neutron star) for a large sample of bursts.

Subsequent study in Rowlinson *et al.* (2010) has further constrained the forbidden regions for these proto-magnetars in Figure 5.1 by using the causality argument i.e. the speed of sound on a neutron star cannot exceed the speed of light to place tighter limits on the minimum radius and mass of the neutron star. This study also found an internal plateau in a short burst GRB 090515 which would be consistent with theoretical limits for a proto-magnetar assuming if it collapsed by a merger progenitor that it had a redshift of $0.2 \leq z \leq 4.4$.

In Chapter 3 I asked if energy injection could be reducing the steepness of the plateau decay observed for internal plateaus, so that traditional plateaus could also signal the collapse of a proto-magnetar. I found that GRBs with internal plateaus clearly stand out separately from traditional plateaus, with central engines that produce early internal plateaus in the light curve having higher magnetic fields for a given rotational period than central engines which could produce traditional plateaus.

This may suggest that an unstable magnetar could not power traditional plateaus and that energy injection cannot explain the lack of steep decline expected to be the signature of the magnetar collapsing to a black hole. However if it were the case

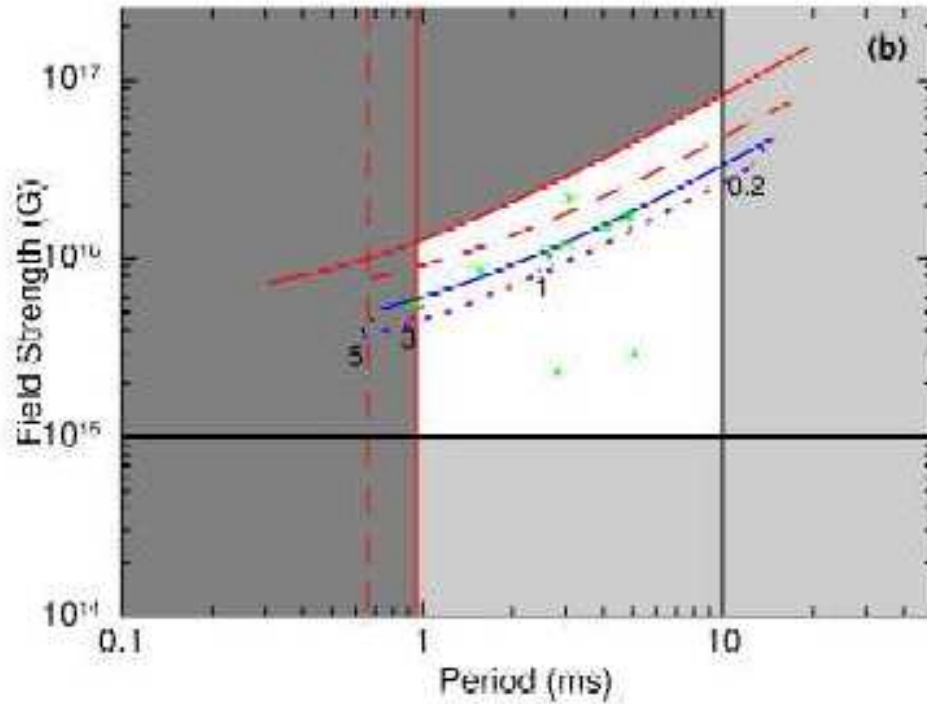


Figure 5.1: The curved red line indicates the new forbidden zone (also shaded in dark grey), the black lines show theoretical limits in Lyons *et al.* 2010. The dotted lines indicate the merger model for short GRB 090515 and the solid blue line the collapsar model for GRB 090515. Green data points represent the long GRB sample with internal plateaus.

that traditional plateaus were due to the collapse of a spinning magnetar, future work could address how they are gaining energy to support their shallow decay or how GRBs with an internal plateau and also a traditional plateau can be produced by a magnetar when by internal plateaus theory the magnetar should have already collapsed to a black hole. Also future work could model the rate these unstable proto-magnetars are likely to form, so that if these are an internal plateau or if unstable proto-magnetars were more common than this signature could be both internal and traditional plateaus.

5.4 Central Engine Activity

Strong evidence has been found that late flares such as those seen in GRB 050502B and GRB 050724 (with a rest frame at $\sim 5 \times 10^4$ seconds) are produced by internal shocks (Chincarini *et al.* 2007, Burrows *et al.* 2007) which indicates that the central engine is long-lived (Lazzati & Perna 2006). It has been suggested that traditional plateaus could be produced by central engine activity (Zhang & Mészáros 2001 and discussed in Chapter 2 Section 2.4), although these plateaus could also be produced by refreshed shocks (Nousek *et al.* 2006), it is not currently possible to distinguish between these two models.

In Willingale *et al.* (2009) a correlation between the characteristic times of a pulse and its peak luminosity was found, this correlation had a gap from 300 - 43,000 seconds. In Chapter 3 I re-plot this correlation with all *Swift* GRBs up to April 2009 that could be fitted by the pulse fitting method. These flares fail to close this gap, implying that these late flares are relatively rare.

In Margutti *et al.* (2010) it is found that flares occur preferentially in GRBs

with a one break or canonical light curve and suggest that flares are often hidden or suppressed in other GRBs. In Chapter 3 I find that there are more flares in GRBs with canonical or one break afterglows, however when the percentage of GRBs (at known distances) with each light curve morphology are compared to the percentage of normal flares in each light curve I find them independent of GRB morphology in disagreement with In Margutti *et al.* (2010). I also find that the weakest afterglows generally do not have flares, which is surprising if flares are commonly hidden by the afterglow. To distinguish if these flares are hidden or being quenched in GRBs if different shape could provide clues to the physics behind the central engine activity at varying times. Future work could superimpose flares found in one break or canonical beaks to the light curves of GRBs with no breaks to test if they would be hidden had they occurred in a GRB with no brakes. If this work found these GRBs would not be hidden it would suggest that flares may be quenched.

In Chapter 4 I also find a possible correlation that GRBs with a short duration tend to have shorter quiescent intervals for between the precursors and GRB and also between giant flares and the GRB. The fact that the possible correlation does not distinguish between these three different types of prompt pulse seems to imply they could each be produced by the same mechanism. This is supported by Burlon *et al.* (2008) which finds that the spectra and energies of the precursor are indistinguishable from the main burst, but contradicted by Koshut *et al.* (1995), Murakami *et al.* 1991 and Hurkett (2008).

A breakthrough in understanding the central engine would occur if it could be probed directly i.e. by gravitational waves. For example in the case of a GRB associated with proto-magnetar (discussed in Chapter 2 Section 2.4) a rate of 40 -

$80 \text{ Gpc}^{-3} \text{ year}^{-1}$ would be required for a detection by the two Einstein Telescopes in the next year (Howell *et al.* 2010). Without a ground breaking observation, future work could be invested in a major effort in theoretical and computational modelling in order to produce testable predictions for different central engines.

5.5 Probing high redshifts

The second major topic touched on by this thesis is one of the most important issues in modern cosmology; how can we extend the cosmological ladder up to high redshifts? In Chapter 3 I examine a sample of GRBs with known redshifts and correct their light curves into the rest frame. I examined the luminosity and isotropic energy of these GRBs in time bins from $10 - 10^5$ seconds. However I did not find a distinct difference between GRBs of varying redshift.

Although the star formation rate for Population III stars is expected to peak $16 \leq z \leq 20$. Campana *et al.* (2001) states that if a GRB was observed at very high redshift ($z \geq 6$) with no intrinsic absorption in the X-ray or UV afterglows (and free of intervening systems) it will be a good candidate for having been produced by a Population III star (whereas at lower redshifts Population II and I stars are seen). Lamb 2007 conflicts with this stating that the star formation for Population III stars peaks at redshifts $16 \leq z \leq 20$, thus it is unlikely Population III stars would be common at ($z \geq 6$).

The sample of *Swift* GRBs with redshift contains three GRBs with $z \leq 6$, hence in Chapter 3 the rest frame light curves of 15 GRBs with increasing redshifts are plotted to investigate if there are any significant differences between the high redshift and low redshift GRBs. No defining feature of difference can be seen in

the light curve as the GRB light curve increases, this implies that this is too low to be from Population III stars. Thus the stars at redshift 8 may not be different enough in composition or other properties to produce an obvious difference to GRBs at closer redshifts, produced by Population I or II stars.

5.6 Conclusions

In this thesis I have set limits on the magnetic field and rotational periods of the central engine for a small group of GRBs with emission thought to be the signature of a magnetar, these parameters are consistent with theoretical limits for a proto-magnetar. I also repeat this model for GRBs with traditional plateaus and find that it is unlikely that they can produce as extremely magnetic fields and periods. I raise theoretical problems for consideration when using this theory for traditional plateaus. For giant flares, I have proven that it is unlikely that they are actually the GRB (and the measured GRB is unlikely to be a precursor). Further more for GRBs with good BAT data I find that the spectra could distinguish between the GRB and a giant flare with similar fluence. Finally I have also shown that for GRBs with known distances there are no new trends that could be used to indicate redshift one their light curves are corrected to the rest frame.

Chapter 6

References

- Amati L. *et al.* A & A, 390,81
- Band D. *et al.* 1993, ApJ, 413, 281
- Barbier L. *et al.* 2007, GCN 6966
- Baring G. 1993, ApJ, 418,391
- Barthelmy S. *et al.* 2005, Space Science Review, 120, 143
- Barthelmy S. *et al.* 2006, GCN 5107
- Barthelmy S. *et al.* 2009, GCN 10251
- Becker R. H. *et al.* 2001, AJ, 122, 2850
- Berger E., *et al.* 2003, Nature, 426, 154
- Berger E., *et al.* 2005, ApJ, 634, 501
- Bloom, J., S. *et al.* 2001, ApJ, 121, 2879
- Bloom, J., S. *et al.* 2003, ApJ, 594, 674
- Briggs M. S. *et al.* 1996, ApJ, 459, 40
- Bucciantini, N. *et al.* 2007, MNRAS, 380, 1541
- Burlon D. *et al.* 2008, ApJ, 685, 19

- Burrows D., N. *et al.* 2005, *Space Science Review*, 120, 165
- Burrows D., N. *et al.* 2005, *Science*, 309, 1833
- Burrows D., N. *et al.* 2007, *RSPTA*, 365, 1213
- Burrows D., N. *et al.* 2008, *SPIE*, 6686, 607
- Campana S. *et al.* 2001, *ApJ*, 561, 924
- Campana S. *et al.* 2006, *Nature* 442, 1008
- Campana S. *et al.* 2010, *MNRAS*, 410, 1611
- Cannizzo J. K. *et al.* 2010, *GNCR* 10288
- Cardone V. F. *et al.* 2010, *MNRAS*, 408, 1181
- Chaisson E. & McMillan S., 1993, *Astronomy Today*, 418
- Chevalier R., A., 2005, *ApJ*, 619, 839
- Chincarini G. *et al.* 2007, *ApJ*, 671, 1903
- Chincarini G. *et al.* 2010, *MNRAS*, 406, 2113
- Christensen L. *et al.* 2004, *AA*, 425, 913
- Colgate S. A. 1968, *Canadian J. Phys.*, 46, 476
- Colgate S. A. 1973, *ApJ*, 181, L53
- Costa E. & Frontera F. 1997, *Nature*, 387, 878
- Cowsik R. *et al.* 2001, *BASI*, 29, 157
- Cummings, J., R. *et al.* 2005, *GCN* 339
- Cummings, J., R. *et al.* 2007, *GCN* 6007
- Curran *et al.* 2008, *A & A*, 487, 533
- Dado S. & Dar A., 2010, *ApJ*, 712, 1172
- Dai, Z., G. & Lu, T. 1998, *A & A*, 333, L87
- Daigne F. & Mochkovitch 2002, *MNRAS*, 336, 1271
- Dainotti M. G. *et al.* 2008, *MNRAS*, 391L, 79

- Dainotti M. G. *et al.* 2010, ApJ, 722, L215
- Dall’Aglia A. *et al.* 2008, A & A, 480, 359
- Dall’Osso S. *et al.* 2010, MNRAS, 408, 1387
- Dermer C., D., 2004, ApJ, 628, 21
- Dermer C. D. 2007, ApJL, 661, L394
- Drago A. & Pagliara G. 2007, ApJ, 665, 1227
- Duncan R., C., 1998, ApJ, 498, L45
- Duncan R. C., & Thompson C. 1992, ApJ, 392, L9
- Eichler D. *et al.* 1989, Nature, 340, 126
- Eichler D. & Levinson A., 1999, ApJ, 521, L117
- Eichler D. & Granot J., 2006, ApJ, 641, L5
- Evans P. A. *et al.* 2007, A & A, 469, 379
- Evans P. A. *et al.* 2009, MNRAS, 397, 1177
- Evans P.A *et al.* 2010, MNRAS, 397, 1177
- Falcone A. D. *et al.* 2006, ApJ, 641, 1010
- Fan Y. Z. 2010, MNRAS, 403, 483
- Fan Y. Z. & Wei D. M. 2005, MNRAS, 364, L42
- Fan Y. Z. & Wei D. M. 2005, MNRAS, 369, 197
- Fenimore, Epstein & Ho 1993 AA Suppl., 97 59
- Fenimore E. E. *et al.* 1996, ApJ, 473, 998
- Fenimore E. *et al.* 2006, GCN 5831
- Firmani C. *et al.* 2006, MNRAS, 370, 185
- Fishman G. J. 1998 A & A, 188, 159
- Fox D. *et al.* 2005, Nature, 437, 845
- Frail D. A., *et al.* 2000, ApJ, 537, 191

- Frail, D. A. *et al.* 2001, ApJ, 562, 55
- Fryer C. L., 1999, ApJ, 522, 413
- Gal-Yam A. *et al.* 2006, Nature, 444, 1053
- Galama T. J. *et al.* 1998, Nature, 395, 670
- Gehrels N. *et al.* 2004, ApJ, 611, 1005
- Gehrels N. *et al.* 2006, Nature, 444, 1044
- Genet F. & Granot J., 2009, MNRAS, 399, 1328
- Ghirlanda G. *et al.* 2004, ApJ, 616, 331
- Ghisellini G. *et al.* 2006, MNRAS, 372, 1699
- Goad M. R. *et al.* 2006, A & A, 449, 89
- Goodman J., 1986 ApJ, 308, L47
- Granot J. *et al.* 2002, ApJ, 570, L61
- Granot J. & Kumar P. 2006, MNRAS, 366, L13
- Granot J. 2007, RMxAC, 27, 140
- Guetta D. *et al.* 2004, ApJ, 615L, 73
- Hjorth J. *et al.* 2003 Nature, 423, 6942
- Hflich P. *et al.* 1998, ApJ, 492, 228
- Howell E. *et al.* 2010, MNRAS, 410, 2123
- Hullinger D. *et al.* 2006, GCN 4635
- Hurkett C. P. 2008a, ApJ, 679, 587
- Hurkett C. P. 2008b, PhD Thesis, Gamma-Ray Bursts: Selected results from the *Swift* Mission, University of Leicester
- Jin Z. P. *et al.* 2010, ApJ, 724, 861
- Kaspi V., M., 2004, IAUS, 218, 231
- Katz, J. I. 1994, ApJ, 422, 248

- Katz J. I. & Piran T. 1997, ApJ, 490, 772
- King A. *et al.* 2005, ApJ, 630, L113
- Klebesadel R. W., Strong I. B. & Olson R. A. 1973, BAAS, 5, 322
- Kobayashi S. *et al.* 1997, ApJ, 490, 92
- Koshut T. M. *et al.* 1995, AAS, 186, 530
- Kouveliotou C. *et al.* 1993, ApJL, 413, L101
- Kouveliotou C. *et al.* 1995, AAS, 186, 530
- Kouveliotou C., Duncan R. & Thompson C. 2003, SC AM, 200302, 35-41
- Krimm H. *et al.* 2007, GCN 6058
- Krimm H. A. *et al.* 2009, GCN 9241
- Kumar P. & Panaitescu A., 2000, ApJ, 541, L51
- Kumar, P., *et al.* 2008a, A & A, 388, 1729
- Kumar, P., *et al.* 2008b, Science, 321, 376
- Lamb & Reichart 2000, ApJ, 536, 1
- Lamb D. Q. 2007, Phil. Trans. R Soc A. 365, 1363
- Lattimer, J., M. & Prakash, M. 2004, Sci, 304, 536
- Lazzati D., Rossi E., Covino G., *et al.* 2002, 330, 583
- Lazzati D., & Begelman M. C., 2005, ApJ, 629, L903
- Lazzati D., & Begelman M. C., 2006, 641, 972
- Lazzati & Perna 2006, MNRAS, 375, L46
- Lee T. & Dermer C. D. 2007, ApJ, 661, 394
- Li L.-X., 2007, MNRAS, 380, L621
- Liang E. *et al.* 2006, ApJ, 646, L351
- Liang, E., E., *et al.* 2007, ApJ, 670, 565
- Liang E. W. *et al.* 2009, ApJ 707, 328

- Liang E. W. *et al.* 2010, ApJ 725, 2209
- Lil-X. 2007, MNRAS, 380, 621
- Lipunova G., V. *et al.* 2009, MNRAS, 397, 1695
- Littlejohns O. *et al.* 2012, MNRAS, 412, 2692
- Livio M. & Waxman E., 2000, ApJ, 538, 187
- Lloyd N. M. & Petrosian V. 2000, ApJ, 543, 722
- Lyons N. *et al.* 2010, 402, 705
- Lyubarsky Y. E. 2003, MNRAS, 345, L153
- Lyubarsky Y. E. 2005, MNRAS, 358, L113
- Lyutikov M. & Blandford R. D. 2003, MNRAS, 346, 540
- MacFadyen A. I. *et al.* 2001, ApJ, 550, 410
- Malesani D. *et al.* 2004, ApJL, 609, L5
- Manganol V. *et al.* 2007, A & A, 470, 105
- Margutti R. *et al.* 2010, MNRAS, 406, 2149
- Markwardt C. *et al.* 2006, GCN 5174
- Markwardt C. *et al.* 2006, GCN 6596
- Markwardt C. *et al.* 2007, GCN 6591
- Matzner C. D. & McKee C. F., 1999, ApJ, 510, 379
- McLaughlin M. A., Stairs I. H. & Kaspi V. M., 2003, ApJ, 591, 135
- Mészáros, P., 2006, RPPh, 69, 2259
- Mészáros, P. & Rees, M. J. 1997, ApJ, 476, 232
- Mészáros, P. & Rees, M. J. 2000, ApJ, 530, 292
- Metzger *et al.* 1997, Nature, 387, 878
- Metzger M. R. *et al.* 2000, ApJ, 534, 248
- Metzger B. D. *et al.* 2011, MNRAS, 413, 2031

- Monchmeyer R. 1991 in Woosley S. E. ed., *Supernovae*, 358
- Murakami T. *et al.* 1991, *Nature*, 350, 592
- Nakamura T. 1998, *Prog. Theor. Phys.*, 100, 921
- Nakar E. *et al.* 2005, *ApJ*, 635, 516
- Nakar E. 2010, *Italian Physical Society Conference Proceedings*, 102, 403
- Norris J. P. *et al.* 2005, *ApJ*, 627, 324
- Nousek, J., A. *et al.* 2006, *ApJ*, 642, 389
- O'Brien, P.T. *et al.* 2006, *ApJ*, 647, 1213
- O'Brien, P.T. *et al.* 2006, *NJP*, 7, 121
- Oates S. *et al.* 2009, *MNRAS*, 395, 490
- Paczynski B. 1986, *ApJ*, 308, L43
- Paczynski B. 2000, *ApJ*, 363, 218
- Page K. L. *et al.* 2006, *GCNR*, 15, 2
- Page K. L. *et al.* 2007, 663, 1125
- Page K. L. *et al.* 2009, *MNRAS*, 400, 134
- Palmer D. *et al.* 2007, *GCN* 6643
- Panaitescu A. *et al.* 2006, *MNRAS*, 369, 2059
- Panaitescu A. 2008, *MNRAS*, 383, 1143
- Panaitescu A. *et al.* 2008, *MNRAS*, 369, 2059
- Pe'er A. *et al.* 2006, *ApJ*, 652, 482
- Petrosian V. *et al.* 2009, arXiv0909.5051
- Pian *et al.* 2000, *ApJ*, 536, 778
- Piro L. *et al.* 2005, *ApJ*, 623, 314
- Podsiadlowski P. *et al.* 1995, *MNRAS*, 273, 755
- Pols O. 1997, in *ASP Conf. Ser.* 130, *The Third Pacific Rim Conference on Re-*

- cent Development in Binary Star Research, 153
- Prochaska J. *et al.* 2006, ApJ, 168, 231
- Qin Y. -P. *et al.* 2004, ApJ, 617, 439
- Qin Y. -P. 2006, Phys. Rev. D 74, 063005
- Racusin J. L. *et al.* 2008, Nature, 455, 183
- Racusin J. L. *et al.* 2009, ApJ, 698, 43
- Ramirez-Ruiz E. *et al.* 2001, MNRAS, 327, 829
- Ramirez-Ruiz E. *et al.* 2002, MNRAS, 331, 197
- Ramirez-Ruiz E., Celotti A. & Rees M. J., 2002, MNRAS, 337, 1349
- Rees M. J., & Mészáros, P. 1994, ApJ, 430, L93
- Rees M. J., Mészáros P. & Begelman M. C., 1994, AIPC, 307, 606
- Reichart D. E. *et al.* 2001, ApJ, 552, 57
- Romano P. *et al.* 2006, NCimB, 121, 1067
- Roming *et al.* 2005, SSRv, 120, 95
- Rosswog S. & Ramirez-Ruiz E., 2003, AIPC, 727, 361
- Rosswog S. *et al.* 2003, MNRAS, 345, 1077
- Rowlinson A. *et al.* 2010, MNRAS, 409, 531
- Ruffini R. *et al.* 2001, ApJ, 555, L113
- Ryde F. & Svensson R. 1999, ApJL, 636, L73
- Sahu K. C. *et al.* 1997, ApJ, 489L, 127
- Sakamoto T. *et al.* 2004, ApJ, 602, 875
- Sakamoto T. *et al.* 2005, GCN 3938
- Sakamoto T. *et al.* 2008, ApJ Suppl, 175, 179
- Salvaterra R. *et al.* 2008, MNRAS, 385, 189
- Salvaterra *et al.* 2009, MNRAS, 396, 299

- Sari, R., & Piran, T. 1997, ApJ, 485, 270
- Sari, R., & Piran, T. 1999, ApJ, 520, 641
- Sari, R., Piran, T., Narayan, R. 1998, ApJ, 497, L17
- Sato G. & Barthelmy S. 2007, GCN 6551
- Sato G. *et al.* 2006, ApJ, 657, 359
- Sato G. *et al.* 2007, ApJ, 657, 359
- Schmidt 2001, ApJ, 559L, 79
- Shao L. *et al.* 2010, ApJ, 719, 172
- Shemi A. & Piran T. 1990, ApJ, 365, L55
- Sollerman J. *et al.* 2005, New A, 11, 103
- Stairs, I., H., 2004, Science, 304, 547
- Stanek *et al.* 2003, ApJ, 591, 17
- Starling R., L., C. *et al.* 2008, MNRAS, 384, 504
- Stella L. *et al.* 2005, ApJ, 634, 165
- Svensson K. M. *et al.* 2010, MNRAS.405, 57
- Tanvir N. R. *et al.* 2009, Nature, 461, 1254
- Thompson, C. & Duncan, R., C. 1993, ApJ, 408, 194
- Thompson, C. 1994, MNRAS, 270, 480
- Thompson C. *et al.* 2002, 574, 332
- Thompson C. 2006, ApJ, 651, 333
- Thompson T. A., 2005, Il Nuovo Cimento C, 28, 583
- Thompson, T., A. 2007, Revista Mexicana de Astronomia y Astrofisica Conference Series, 27, 80
- Toma K., Sakamoto T. & Mészáros P., 2011, ApJ, 731, 127
- Troja, E. *et al.* 2007, ApJ, 665, 599

- Tueller J. et al. 2006, GCN 5242
- Tueller J. et al. 2008, GCN 7402
- Usov, V., V. 1992, Nature, 357, 472
- Valageas P. & Silk J., 1999, A & A, 347, 1
- Vanderspek R. *et al.* 2004, ApJ, 617, 1251
- Vlahakis N., Peng F. & Konigl A., 2003, ApJ, 594, L23
- Wang X., -Y. & Mészáros, P., 2007, 670, 1247
- Waxman E. & Mészáros, P. 2003, ApJ, 584, 390
- Waxman E. 2004, ApJ, 602, 886
- Wheeler J. C. *et al.* 2000, ApJ, 537, 810
- Willingale R. *et al.* , 2007, ApJ, 662, 1093
- Willingale R. *et al.* 2009, MNRAS, 403, 1296
- Willingale R. *et al.* 2010, MNRAS, 403, 1296
- Woods P. M. & Thompson C. 2006, 547
- Woosley S. E. & Heger A. 2005, ASPC, 332, 395
- Woosely S. E. 1993, ApJ, 405, 273
- Woosley S. E., & Weaver T. A., 1986, ARA&A, 24, 205
- Woosely S. E. *et al.* 1999, ApJ, 516, 788
- Xiao L. & Schaefer B. E., 2009, 707, 387
- Yamada S. & Sato K. 1994, ApJ, 434, 268
- Yamazaki R. *et al.* 2003, ApJ, 594, L79
- Yoon, S.-C. & Langer, N., 2005, A & A, 443, 643
- Zeh A. *et al.* 2006, ApJ, 637, 889
- Zhang B. & Mészáros P., 2001, ApJ, 552, L35
- Zhang B. *et al.* 2006, ApJ, 642, 354

Zhang B. *et al.* 2007, ChJAA, 7, 1

Zhang B. *et al.* 2009, ApJ, 703, 1696

Zhang B. & Yan H. 2011, ApJ, 726, 89

Zou Y. C. & Piran T. 2010, MNRAS, 402, 1854